A LOW-COST DEPTH IMAGING MOBILE PLATFORM FOR CANOLA PHENOTYPING

A Thesis Submitted

to the College of Graduate and Postdoctoral Studies

in Partial Fulfillment of the Requirements

for the Degree of Master of Science

in the Department of Electrical and Computer Engineering

University of Saskatchewan

Saskatoon, Saskatchewan, Canada

By

HONG THANG CAO

Permission to Use

In presenting this thesis in partial fulfillment of the requirements for a Postgraduate degree from the University of Saskatchewan, I agree that the Libraries of this University may make it freely available for inspection. I further agree that permission for copying of this thesis in any manner, in whole or in part, for scholarly purposes may be granted by the professor or professors who supervised my thesis work or, in their absence, by the Head of the Department of Electrical and Computer Engineering or the Dean of the College Graduate and Postdoctoral Studies at the University of Saskatchewan in which my thesis work was done. It is understood that any copying or publication or use of this thesis or parts thereof for financial gain shall not be allowed without my written permission. It is also understood that due recognition shall be given to me and to the University of Saskatchewan in any scholarly use which may be made of any material in my thesis.

Disclaimer

Reference in this thesis to any specific commercial products, process, or service by trade name, trademark, manufacturer, or otherwise, does not constitute or imply its endorsement, recommendation, or favoring by the University of Saskatchewan. The views and opinions of the author expressed herein do not state or reflect those of the University of Saskatchewan, and shall not be used for advertising or product endorsement purposes.

Requests for permission to copy or to make other uses of materials in this thesis in whole or part should be addressed to:

Head of the Department of Electrical and Computer Engineering
57 Campus Drive
University of Saskatchewan
Saskatoon, Saskatchewan S7N 5A9
Canada

OR

Dean
College of Graduate and Postdoctoral Studies
University of Saskatchewan
116 Thorvaldson Building, 110 Science Place
Saskatoon, Saskatchewan S7N 5C9
Canada

Abstract

To meet the high demand for supporting and accelerating progress in the breeding of novel traits, plant scientists and breeders have to measure a large number of plants and their characteristics accurately. A variety of imaging methodologies are being deployed to acquire data for quantitative studies of complex traits. When applied to a large number of plants such as canola plants, however, a complete three-dimensional (3D) model is time-consuming and expensive for high-throughput phenotyping with an enormous amount of data. In some contexts, a full rebuild of entire plants may not be necessary. In recent years, many 3D plan phenotyping techniques with high cost and large-scale facilities have been introduced to extract plant phenotypic traits, but these applications may be affected by limited research budgets and cross environments. This thesis proposed a low-cost depth and high-throughput phenotyping mobile platform to measure canola plant traits in cross environments. Methods included detecting and counting canola branches and seedpods, monitoring canola growth stages, and fusing color images to improve images resolution and achieve higher accuracy. Canola plant traits were examined in both controlled environment and field scenarios. These methodologies were enhanced by different imaging techniques. Results revealed that this phenotyping mobile platform can be used to investigate canola plant traits in cross environments with high accuracy. The results also show that algorithms for counting canola branches and seedpods enable crop researchers to analyze the relationship between canola genotypes and phenotypes and estimate crop yields. In addition to counting algorithms, fusing techniques can be helpful for plant breeders with more comfortable access plant characteristics by improving the definition and resolution of color images. These findings add value to the automation, low-cost depth and high-throughput phenotyping for canola plants. These findings also contribute a novel multi-focus image fusion that exhibits a competitive performance with outperforms some other state-of-the-art methods based on the visual saliency maps and gradient domain fast guided filter. This proposed platform and counting algorithms can be applied to not only canola plants but also other closely related species. The proposed fusing technique can be extended to other fields, such as remote sensing and medical image fusion.

Acknowledgments

I would like to express my sincere appreciation to my parents and family for supporting and encouraging me during my time here. I want to special express my thanks to Trang Nguyen for her love, promote, and advice.

First, I sincerely gratitude my supervisor, Prof. Anh Dinh, who gives me not only financial and moral support but also expert advice. I acknowledge the support from the Global Institute for Food Security, Canada, and Agriculture Development Fund, Saskatchewan, Canada. My appreciation also goes to Prof. Khan Wahid, Prof. Scott Noble, Prof. Reza Fotouhi, and their colleagues for assisting me with some experiments in the fields.

I would also like to thank Dr. Bett Kirstin, Dr. Sally Vail, Dr. Pankaj Bhowmik, and Mr. Dan Vessey for supporting me with canola samples and other equipment that I used to perform some experiments in the lab.

Lastly, I convey my gratitude to my friends and colleagues who offered their advice to answer my questions on various parts of this thesis: Tung Nguyen, Nhat Pham, Long Le, Loc Luu, Quang Duong, and Karim Panjvani.

Dedication

Dedicated to my amazing parents for their love, support, and encouragement.

Table of Contents

page

List of Tables

List of Figures

List of Abbreviations

2D	Two-dimensional
3D	Three-dimensional
ARW	Sony alpha raw
CCD	Charge-coupled device
CPU	Central Processing Unit
DC	Direct current
DNA	Deoxyribonucleic acid
FGF	Fast guided filter
Fps	Frame per second
GDGIF	Gradient domain guided filter
GPIO	General-purpose input/output
HTTPs	High-throughput phenotyping platforms
IPC	Inter-process communication
IQA	Image quality assessment
IR	Infrared
LED	Light-emitting diode
LiDAR	Light Detection and Ranging
MFM	Multi-stencils Fast Marching
NIFA	National Institute of Food and Agriculture
NIR	Near infrared region
OS	Operating system
PSII	Photosystem II (or water-plastoquinone oxidoreductase)
RGB	Red, Green, and Blue

RGB-D	A combination of an RGB image and its corresponding depth image
ROI	Area of interest
SWIR	Short wavelength infrared region
ToF	Time-of-Flight
UAP	Unmanned aerial platform
UAVs	Unmanned aerial vehicles
USDA	United States Department of Agriculture
UV	Ultraviolet
VIS	Visible region
VS	Visual saliency

CHAPTER 1 - INTRODUCTION

1.1 A Statement of Objectives

The sharp increase demand for global food raises the awareness of the public, especially, agricultural scientists to the global food security. According to the recent assessment report of the future of food and agriculture [1], the world would reach its population of 9.73 billion by 2050 and 11.2 billion by 2100. To meet the high demand for food in 2050, agriculture will need to produce almost 50 percent more food than was produced in 2012 [1]. In Canada, plant scientists are working to improve yield of the major crops, including wheat, barley, lentils, and canola. Canola is an outstanding agricultural product for Canada. Canola refers to a particular group of rapeseed varieties, a species of the much larger mustard family, including mustard, turnips, cauliflower, cabbage, and broccoli [2]. Three members of the Brassicaceae family, such as Brassica napus, Brassica rapa, and Brassica oleracea (wild mustard), are referred as canola. Canola or rapeseed (Brassica napus) was first grown in Canada during the Second World War but almost disappeared by 1950 when steam power invented. Due to the demand of oilseeds depending on the imported markets, canola was developed by plant breeders in Saskatchewan and Manitoba from the 1960s to 1970s [2]. The crop area planted to rapeseed, and a decade later canola has sharply expanded, from 143,000 hectares in 1956 to 5 million hectares in 2006. Recently, there are more than 20 million acres of canola planted, as reported in 2016 [3], with yields of 42.3 bushels (0.959 tonnes) per acre [4]. The new target of the Canadian canola industry was set to 26 million tonnes of seeds and 52 bushels per acre by 2025 [3]. To response this target, canola productivity must be improved.

There are many ways of improving yields for canola and other crops. These solutions, such as enhancing investment in primary agriculture and promoting technology change, are suggested [1]. One of these solutions to meet the high demands for food is to increase breeding efficiency. In the past decade, advances in genetic technologies, such as next-generation DNA sequencing, have provided new methods to improve plant-breeding techniques. Using these novel technologies, plant breeders can increase the rate of genetic improvement through molecular breeding [5]. However, the lack of knowledge of phenotyping capabilities limits the ability to analyze the genetics of quantitative traits related to plant growth, crop yield, and adaptation to stress [6]. Phenotyping creates opportunities not only for functional research on genes, but also for the development of new crops with beneficial features. To fulfill these opportunities, integrated approaches are needed that bring together genotypes and phenotypes of all scales to develop sustainable plant production with higher yield crops and better use of limited resources of land, water, and nutrients.

Image-based phenotyping methods are those integrated approaches that enable the potential to greatly enhance plant researchers' ability to characterize many different traits of plants. As non-invasive techniques, these methods can capture plant traits with a precision that crop researchers cannot achieve. In addition, traditional evaluations of plant traits are time-consuming, labor intensive, commonly require expertise, and prone to human error. Also, these image-based methods can acquire many different traits of plants faster than human beings do. These image-based techniques can be classified into two categories such as two-dimensional (2D) and three-dimensional (3D) image-based approaches. 2D image-based approaches are commonly applied and provide many benefits in plant phenotyping; however, there are some limitations when investigating 3D plant structures. For example, the curved leaf area or plant volume can be estimated by 2D image-based techniques, but results are prone to error. 3D image-based techniques can overcome the limitations of 2D image-based techniques. These 3D image-based approaches are well suited to capture 3D structure of plants. 3D image-based information provides good indicators of plant responses to environmental conditions. For example, stresses such as drought and extreme temperatures can change the shape, structure, color, and pattern of individual plants. Thus, image-based approaches with the potential for high accurate, high throughput and non-invasive techniques are required for accurate plant phenotyping.

Recently, there has been increased interest in high-throughput phenotyping approaches in controlled environments. There are many image-based techniques used in high-throughput phenotyping approaches [6,7], such as visible imaging, spectroscopy imaging, thermal imaging, fluorescence imaging, LiDAR, laser, and Time-of-Flight, which can provide quantitative morphological measurements of plants. Many studies [8,9,10] have deployed laser systems (LemnaTec Scanalyzer) in small-scale research centers, be able to scan both 2D and 3D images of the plant surfaces for extracting particular phenotypic traits. Some larger-scale facilities, such as the Australian Plant Phenomics Facility, the European Plant Phenotyping Network, and the USDA-NIFA, have also adopted robotics, precise environmental controls, and remote sensing techniques to assess plant characteristics in both growth chambers and greenhouses. Similarly, authors in [11] adopted a high-resolution 3D laser scanner (PlantEye, Phenospex) to monitor plant growth with high precision in challenging environments. In another study, Light Detection and Ranging sensor (LiDAR) is the most widely used for 3D canopy reconstruction of plants due to its greater robustness, accuracy, and resolution [12]. LiDAR creates accurate and detailed 3D models by using a pulsed laser to measure variable distances between the sensor and the object. However, these systems are expensive and time-consuming and may not be suitable for field environments as they are mainly built for controlled environments.

In the fields, many phenotyping platforms have been developed, ranging from ground-based to aerial systems. Most plant phenotyping systems have focused on automated and high-throughput solutions for data acquisition. A tractor-based high-throughput phenotyping system [13] has been developed to determine rice genetic variation of important underlying traits. Many research centers, such as the University of Arizona Maricopa Agricultural Center, USDA Arid Land Research Station in Maricopa, Arizona, and the Rothamsted Research Centre in the St Albans city in the county of Hertfordshire, have implemented phenotyping field scanner systems (Lemnatec FIXED GANTRY) to monitor plant traits. These scanner systems are fully automated gantry systems designed to capture depth data from crops and other plants growing in field environments. In general, these field-based phenotyping platforms perform well in field environments, but are still expensive and designed for field purposes only. Ideally, to fulfill the requirements of crop research institutions with limited budgets, a 3D mobile phenotyping system with low-cost and high-throughput should be developed for use across environments in both controlled and field settings.

Beside many advanced image-based phenotyping techniques, image fusion techniques also offer great potential for plant researchers to analyze complex traits by enhancing image resolution. In plant science, image fusion techniques aim at combining the data acquired from either many different sensors or the same sensor with a different focus length for improving image resolution, image segmentation, feature extraction, modeling, and classification. Many studies have deployed fusion techniques to detect plant diseases [14], identify the plant location, segment its leaves, and measure leaf topology and area [15], and identify and localize plant [16]. These findings imply that fusion techniques can offer many benefits for further image processing.

There are many scholars have investigated canola plant traits and their responses to the environmental conditions. Authors in [17] have measured nitrogen status and biomass of oilseed rape by using laser-induced chlorophyll fluorescence. Few years later, authors in [11] have investigated the rapeseed growth parameters, such as plant height, leaf area, number of leaves, and biomass, by using 3D laser triangulation system, but total leaf area was underestimated. In the interesting analysis of quantifying oilseed rape leaf traits described in [18], leaf area and plant height with high accuracy have been extracted by using a high-throughput stereo-imaging system. Besides the investigation of plant traits, many studies have been conducted to analyze the plant responses to the surroundings. The reaction of oilseed rape (Brassica napus) to fungal species have been examined by using hyperspectral and thermal imaging [19]. Similarly, authors in [20] have reviewed machine-learning tools using color images for high-throughput stress phenotyping in various plants, including oilseed rape. Recently, similar experiments have been performed to monitor oilseed rape growth-related traits and plant responses to water stress [21]. These findings suggest that there are many high-throughput plant phenotyping techniques to monitor and analyze plant traits; however, there are few studies have conducted to count canola branches and seedpods.

The main objective of this thesis is to propose a low-cost depth high-throughput phenotyping mobile platform for cross environments. The second objective is to detect and count the number of canola branches and seedpods. The third objective is to monitor canola growth stages, such as measuring canola plant height. The fourth objective is to fuse color images to enhance image quality and resolution. Some experiments are necessary to meet these goals. The first experiment examines the detecting and counting canola branches. The second experiment examines the detecting and counting canola seedpods. The third experiment investigates the height of individual canola plants. The fourth experiment surveys some image fusion techniques.

1.2 Contributions

This study makes five contributions to the canola phenotyping and image processing areas: developing a low-cost depth high-throughput phenotyping mobile platform; proposing methods for detecting and counting canola seedpods and branches; setting forth a platform for monitoring canola growth stages; and developing fusing techniques to improve images resolution from low cost cameras.

1.2.1 A Low-Cost Depth High-Throughput Phenotyping Mobile Platform

A low-cost depth high-throughput phenotyping mobile platform in cross environments is proposed. This platform consists of a Raspberry Pi3, an Argos3D P100 camera and a Pi camera. The Raspberry Pi3 is used as a mini computer to control the depth (Argos3D P100) and Pi cameras. First, this platform is built from a low-cost depth camera with outperform, the Argos3D P100 camera, for a US $1,200 budget. By providing 3D and grayscale information, the depth camera offers excellent potential for 3D modeling and other analyzing plant traits. Multiple 3D images from various views are captured to generate point cloud data used to reconstruct the 3D plant models. The depth camera also provides grayscale information which is used to monitor canola growth stages and to count canola branches and seedpods.

Besides the low-cost depth advantage, high-throughput phenotyping mobile platform in cross environments is also another advantage. This proposed system shows the capability of an automated and high-throughput phenotyping system via our experiments. The very high-performance depth sensor is able to capture a resolution of 160 x 120 pixels and up to 160 frames per second (fps). This 3D sensor simultaneously delivers either 3D data and amplitude (intensity level) information or depth and amplitude data for each of the 160 x 120 pixels, adding up to 19,200 independent measuring points for each measurement (https://www.bluetechnix.com). Also, this system can be applied in both environments, such as a controlled environment and field scenario. In the field, a tractor arm and a sprayer boom are used to mount the system, enabling movement anywhere around plant plots. In the laboratory, the system is fixed on a camera tripod or a frame, and the plant is turned on a turntable device. The system can also be moved around the canola plant to capture data. Moreover, this system can achieve data either manually via remote control and the internet or automatically by pre-configured settings.

1.2.2 Methods for Detecting and Counting Canola Branches and Seedpods

Although many studies have investigated plant structure and health status structure, few studies have detected branch points and counted seedpods. Many studies [22,23,24] have focused on leaves, canopy health status and shoots of crop plants (e.g., soybeans, wheat, triticale, maize, pepper, sorghum, rice, and barley). Other studies have highlighted findings in detecting flowers and counting soybean seedpods [25], as well as detecting branch points to locate the cutting point of the rose stem for robotic rose harvesting [26]. To date, however, few studies have detected and counted canola branches and seedpods. Canola plants have unique characteristics, such as many thin and small seedpods in each plant, making counting seedpods time-consuming. In addition, the more branches of a canola plant, the higher the crop yield. Therefore, a non-invasive automated process to count canola branches and seedpods is required for crop researchers and breeders. The number of canola branches and seedpods is an essential factor in analyzing the relationship between genotypes and phenotypes, estimating the crop yield, and for other purposes. In this thesis, some techniques for detecting and counting canola branches and seedpods have been developed by applying algorithms, such as the fast-marching-method and the Frangi-vesselness filter. In the future, these approaches can be deployed to other members of rapeseed family and other crop plants.

1.2.3 Methods for Monitoring Canola Growth Stages

With the advantages of the proposed platform, the 3D information (point cloud images), grayscale data (distance and amplitude images), and color images of canola plants are retrieved from multiple views during growth stages. These data are used to monitor canola growth stages, such as the height of individual canola plants, the height of canola plots, number of leaves, and leaf area.

To estimate the height of individual canola plants or canola plots, an algorithm using grayscale images has been developed. To verify the algorithm, manual measurements of the plant height of these individual canola plants are implemented.

1.2.4 Methods for Fusing Images

Fusion of multi-color images acquired from any digital camera or low-resolution Pi camera can offer many improved results to color-image accuracy. This study focuses on how to fuse multi-focus color images to enhance resolution and quality of the fused image. The proposed image fusion was developed and compared with other state-of-the-art image fusion methods.

1.3 Description of the Remaining Chapters

The remain of this thesis is organized as follows. Chapter 2 reviews the background of recent different techniques used for plant phenotyping. In this chapter, the literature review focuses on the basics of plant phenotyping, the role of imaging techniques in plant phenotyping, image acquisition systems, and some high-throughput phenotyping platforms.

Chapter 3 describes the requirements and specifications of the proposed methodology, proposed approaches for detecting and counting canola branches and seedpods, monitoring canola growth stages, and fusing color images. This chapter also introduces algorithms for removing the background and noise, extracting the skeleton of the plant, extracting the area of interest; and detecting and counting canola branches and seedpods. Additionally, this chapter introduces plant height measurement and multi-focus image fusion algorithm.

Chapter 4 shows an image acquisition system deployed for canola plant phenotyping. A mobile system was built that can be applied in the greenhouse or field. This system includes a depth camera and color camera run on a Raspberry Pi3. The advantage of this platform is that it enables data to be captured remotely via a remote control key, automatically obtaining data based on a pre-set time or remote access via the Internet.

Chapter 5 illustrates the results of counting canola branches and seedpods, estimating plant height, and fusing multi-focus color images experiments. The results show that the proposed methods of counting canola branches and seedpods as well as estimating canola plant height are state-of-the-art methods of high accuracy, stability, and reliability. On the other hand, the proposed multi-focus image fusion reveals competitive performance, which outperforms some state-of-the-art methods based on the visual saliency metrics and gradient domain fast guided filter. This fusion method can be used to improve the results of counting canola seedpods from images captured by low-cost cameras or for further study.

Chapter 6 summarizes the whole study and highlights some future research directions.

CHAPTER 2 - LITERATURE REVIEW

This section covers the related technologies and methods implemented in automated high-throughput plant phenotyping. Section 2.1 discusses the basics of plant phenotyping and its role in developing high yield crops. Section 2.2 describes the role of imaging techniques for plant phenotyping. Section 2.3 introduces various image acquisition systems for plant phenotyping. Section 2.4 investigates some high-throughput phenotyping platforms. Finally, Section 2.5 illustrates current image fusion techniques.

2.1 Plant Phenotyping

To understand the relationship between plant phenotypes, plant genotypes, and environmental scenarios, for decades, crop researchers have studied plant phenotyping. A plant phenotype is formed during plant growth from the complex interaction between the genotype and the surrounding environment. Plant phenotyping is the process of quantitatively measuring a set of observable characteristics of plants such as plant height, stem diameter, leaf area, number of seedpods, and canopy. Measuring observed characteristics is vital for plant breeders to understand the plant growth underlying genetic factors and to improve plant-breeding techniques. Accurate plant phenotyping plays a crucial role in analyzing different plant traits in different environmental scenarios. By accurately measuring phenotypic characteristics during a plant’s growth stages, crop breeders can produce crops with higher yields, higher tolerance to drought and stress, and stronger disease resistance.

For many years, traditional plant assessments were labor intensive, prone to errors, and had low-throughput. These assessments were performed from a small sample of plants in selected crop fields. The low-throughput traditional phenotyping is known as a phenotyping bottleneck in plant breeding [8]. The term bottleneck is used because this type of phenotyping both restricts plant researchers’ capacity to understand the correlation between phenotypes with underlying genotypes and environmental conditions and decreases the progress in vital breeding issues such as drought resistance [27]. Due to strong demand from plant breeders for phenotypic information, plant phenotyping has become an emerging field of research in plant breeding. In recent years, plant phenotyping has progressed from manual to automatic measurement, from destructive to non-destructive collection, and from low-throughput to high-throughput platforms. High-throughput phenotyping platforms (HTPPs) are automated, non-invasive, and high-volume systems for plant phenotyping. Many HTPPs have been recently implemented at all scales in growth chambers, in greenhouses and fields [13,23,28,29,30]. Some of these platforms [23,28,29] have applied climate-controlled growth houses to a conveyor belt system for moving plants to and from fluorescent, color, and near-infrared imaging systems to capture and access plant growth. Other platforms [13,28,29,30] have deployed unmanned aerial vehicles (UAVs), ground vehicles (tractors or robots), and automated gantry systems to monitor plants in fields during growth stages. Together, these studies have shown that plant phenotyping plays a crucial role in plant breeding, in which HTPPs improve the plant phenotyping process at all scales and across environments.

2.2 Imaging Techniques in Plant Phenotyping

Imaging techniques are used in plant phenotyping to measure phenotypic characteristics of plants through automated processes non-invasively. With light sources from visible to near-infrared spectroscopy to computed tomography, imaging and image processing techniques offer non-destructive measurements of complex traits. Modern advanced imaging techniques provide high-resolution images and enable visualization of multi-dimensional data. These methods allow plant breeders and researchers to obtain exact data, speed-up image analysis, bring high-throughput and high-dimensional phenotype data for modeling, and estimate plant growth and structural development during the plant life cycle. The application of advanced imaging technologies in plant phenotyping [11,13,16,25] have led to increase in performance such as high-throughput and offer new prospects to improve breeding efficiency, sustain, and enhance crop yields.

With the rapid development of imaging technologies, a number of imaging methodologies have been adapting to capture plants for quantitative research of plant growth during their life cycle. These techniques are well known, such as visible light imaging, infrared imaging, fluorescence imaging, imaging spectroscopy [6]. While 2D imaging techniques, such as visible imaging, infrared imaging, fluorescence imaging, have been successful in plant science for extracting morphological phenotype data and physiological information [6,26,31], they remain some inherent limitations. For instance, it is difficult to measure the area of a curved leaf from its 2D images. Another primary source of uncertainty is that 2D approach causes some error-prone when computes the volume of the plant.

Since 2D imaging techniques have their limitations, 3D based approaches take a chance and overcome these bias for plant phenotyping. 3D imaging techniques offer great potential to plant scientists to comprehend phenotype. The benefit of these approaches is that, for example, the 3D area of the curved leaf is more accurately calculated than 2D based approaches. Due to these significant advantages of 3D techniques, many high throughput phenotyping platforms have been developed. Most of the high-throughput platforms are fully automated, high-speed in greenhouses, growth chambers, or fields. For large-scale, high-throughput phenotyping platforms are offered for the greenhouses and fields by companies, such as LemnaTec, PhenoSpex, Phenokey, Photon System Instruments, and Wiwam. The image-based high-throughput automated system is a perfect tool for plant phenotyping due to the capacity to measure complex traits of the plant, such as the height of the plant, size of the leaf, and canopy of the plant. Moreover, as a consequence of imaging techniques, a set of physical and biochemical traits - provide crop researchers a new approach to understand the relationship between phenotypes underlying genotypes and environmental conditions of living plants via multiple sensors.

2.3 Image Acquisition Systems

This section reviews some techniques for plant phenotyping of aboveground plant organs. These techniques, such as visible light imaging, infrared imaging, fluorescence imaging, spectroscopy imaging, and other 3D imaging, will be explained in the following section.

2.3.1 Visible Light Imaging

The visible light is detectable by human eyes, the wavelengh is ranging from 400 to 700 nm. This region is located in between ultraviolet (UV) and infrared (IR) regions [32]. Visible light imaging is also named RGB (red, green, and blue) color. Using silicon sensors (CCD or CMOS arrays), a visible light camera produces two-dimensional (2D) images that become cutting edge of the simplest plant phenotyping technique.

Due to its low cost, simplicity, and low maintenance cost, visible light imaging is predominantly used in the agricultural area for analyzing the complex traits with all scales. In chambers or greenhouses, authors in [6] have investigated that visible light imaging techniques were used to analyze many plant traits, such as leaf morphology, seedling vigor, shoot biomass, yield traits, panicle traits, germination rates, and root architecture. In control environments, the authors found that visible images of the plant growth stages were used to monitor drought stress response and tolerance of plants. According to the authors [6], canopy cover, leaf area index, and light interception information in the fields were extracted from visible images of canopy cover and canopy color. In a related research [26], a method was developed that can locate the proper location of the cutting point of the rose stem for robotic rose harvesting. Their algorithm for branch detection performed quite well to detect and located the position of the point when there occurs no overlapping. Recently, a hybrid machine learning approach [25] was presented that enabled automatic monitoring to acquire images of soybean flowers and seedpods in the fields. To detect flowers and seedpods in a crowd of soybean plants under outdoor environments, some image processing and machine learning techniques were deployed. Nevertheless, there are some limitations, such as stems and leaves were sometimes wrongly detected as seedpods and seedpods were miss-detected in some cases. Even though this approach is popularly used in plant phenotyping, the limitations are that visible imaging techniques only offer physiological information and cause challenging to extract phenotypic information, such as biomass and leaf area by the overlapping of adjacent leaves and soil background in image segmentation [6,7,31]. These findings implies that visible imaging approaches enable their potential in plant phenotyping.

2.3.2 Infrared Imaging

Infrared imaging is a technology used to measure the temperature and radiation energy of an object. Instead of the wavelength ranges from 400 to 700 nm of the visible light camera, the range of thermal cameras (IR based) is 3–14 µm. The most commonly used wavelengths for thermal imaging are two ranges of 3–5 µm and 7–14 µm because infrared radiation atmospheric transmission is close to its maximum value [6].

Infrared thermal imaging technology uses infrared detectors to convert invisible infrared radiation into a visible image. In plant science, thermal imaging is a very suitable technology for plant phenotyping to assess plant health status response to different stress conditions [33,34]. In a similar research, authors in [35] highlighted the potential applications of IR sensing for analyzing plant responses to water stress. In a study conducted in 2016, the authors showed the ability of their sensing system to observe soybean responses to drought stresses [36]. Some other studies also used thermal imaging techniques to study plant stress responses in field conditions [37,38].

There are many benefits from applying infrared imaging techniques in plant phenotyping. These benefits are that they offer high-throughput phenotyping, spatial resolution, and more precise measurement under changing environmental conditions [6]. They also enable fast collection of data on a single leaf or canopy area. However, a drawback of thermal imaging technology in the field is that it may be affected by soil background, wind, and effects of transient cloudiness [6,8,35,39]. Overall, these studies highlight the need and advantages of infrared imaging techniques in plant phenotyping as well as negative effects of surroundings.

2.3.3 Fluorescence Imaging

Fluorescence imaging is a non-destructive technique that uses to detect plant stresses and responses from the laboratory to the field. Using this technology, the information about the metabolic status of the plant can be obtained [6]. By using charge-coupled device (CCD) cameras, fluorescence imaging is sensitive to fluorescence signals that occur by illuminating samples with visible or ultraviolet (UV) light. With long-wavelength UV radiation (ranging from 320 to 400 nm), the excitation of leaves generates four spectral bands such as blue (440nm), green (520 nm), red (690 nm), and far-red (740 nm).

There have been varieties applications of fluorescence imaging technique to detect and measure photosynthetic responses, pathogen infections, stress responses, etc. One study examined that it is effective to detect stress tolerance in Arabidopsis thaliana and other rosette plants in various conditions such as drought stress, chilling stress, heat, and ultraviolet light [40]. This technique also successfully examine the impact of fungal pathogens on the photosynthetic metabolism of host plants [41]. Numerous studies have attempted to explain that fluorescence imaging was deployed for early detection of stress responses to biotic (e.g., insect attack, fungal infection, and bacterial infection) and abiotic (e.g., water stress, sun exposure, and chilling) factors before a decline in growth [10,39]. As a result, the fluorescence imaging technique becomes a powerful diagnostic tool to monitor plant stresses and responses induced by abiotic or biotic factors, in which some cases allow to detect of disease before visible symptoms appearing. However, the drawback of this technique, such as dark-adaptation for F_v/F_m (maximum quantum efficiency of PSII) measurements, makes it difficult to apply in the field [42]. It also may be limited to field phenotyping applications because of its power requirements by using short wave laser stimulation. Overall, there seems to be some evidence to indicate that fluorescence imaging techniques are powerful approaches to monitor diseases, stresses, and responses of plants. Beside their benefits, it is needed to consider restrictions on the power supply or high illumination.

2.3.4 Imaging Spectroscopy

Imaging spectroscopy (also known as hyperspectral or spectral imaging) is a promising phenotyping tool for accessing plant stresses, biochemical, and structural properties. This technique measures the interaction of solar radiation with plants [6]. In the hyperspectral imaging, the spectral reflectance of each pixel is obtained for a range of wavelengths that includes the visible and infrared regions of the electromagnetic spectra [43]. Depending on the measured wavelengths of the reflected signal, various detectors are used, usually visible region (VIS; 300-750nm), near infrared region (NIR; 750-1400 nm), and short wavelength infrared region (SWIR; 1400-3000 nm). The absorption of light by leaf pigments is used for calculations of many vegetation indices. These indices reflect the composition and function of a plant. These indices are related to different plant properties, such as the plant biomass, photosynthetic size, photosynthetic radiation use efficiency, and physiological status. Spectral measurement can be achieved by multispectral or hyperspectral cameras. Since obtained data in the VIS-NIR spectral region is used for evaluation of several indices (e.g., chlorophyll content, photochemical reflectance, and photosynthetic efficiency), the SWIR spectral region is primarily adapted for the investigation water content of plants [44]. From these vegetation indices, plant researchers can predict the green biomass, leaf area, chlorophyll content, and crop yield of the plant under field conditions [45].

Many studies found that imaging spectroscopy techniques are powerful phenotyping tools in plant science. First, these techniques have been successfully implemented for predicting biophysical and structural features. Surveys such as that conducted by [46] have shown that NIR imaging technique to evaluate the tomato water content under drought conditions. In similar research [47], both berry yield and quality attributes in rain-fed vineyards were well predicted by using hyperspectral reflectance indices related to plant biophysical properties. According to [48], imaging spectroscopy enables modeling and predicting plant functional types at the vegetation community scale with high accuracy and greater consistency than plant growth forms. In all the studies reviewed here, spectroscopy techniques are recognized as highly favorable tools for analyzing biochemical and structural traits of plants and plant stresses in controlled environments and field scenarios. However, the main challenges are the cost and complexity of the spectral devices and their related infrastructures.

2.3.5 3D Imaging

3D imaging techniques pass over 2D-based approaches and become essential methodologies in plant phenotyping. Although 2D imaging techniques are broadly used in plant phenotyping as mentioned above, they still have some drawbacks. First, the imaging process can be easily interfered by changing of environmental light and caused image degradation. Also, 2D image is hard to fully characterize the plant spatial distributions by losing the depth information about the scene. By possessing 3D geometry information, 3D imaging techniques deal with these issues and become innovative solutions in plant science. There are many ways to construct plant traits in 3D, in which plant researchers can gather plant architecture that is fundamental for high yield breeding. One of these methodologies is that 3D plant phenotypic traits can be efficiently reconstructed by using 2D images. Many authors have developed multi-perspective 2D images based approaches to constructing a 3D model of plants [49,50]. In some situations, the size and shape of the plant can be reliably measured in 2D. Nevertheless, 3D information is required, for example, when the biomass, canopy diameter, or volume of the plant is needed to estimate. In these cases, a variety of 3D technologies (such as laser techniques, time-of-flight (ToF) sensors) are used, in which, 3D plant traits of interest can be directly derived. These techniques offer great potential for automated and high-throughput 3D plant phenotyping.

There are many 3D imaging techniques are available. Currently, 3D imaging techniques such as laser sensor, stereo vision, time-of-flight (ToF) cameras, and Microsoft Kinect sensors are popularly used in plant phenotyping. Laser sensor techniques provide precise measurement of 3D plant structures. There are some kinds of laser sensors used in plant science, such as light detection and ranging (LiDAR), terrestrial laser, and triangulation laser. LiDAR (also named as a laser scanner) and laser triangulation are active sensors, in which a light beam (laser line or dot) is projected onto plants. The energy scattered from the plant is used for the computation of depth maps and 3D point clouds [11]. LiDAR offers measurement and details of 3D distribution of plant canopies accurately. Many studies found that 3D data acquired from LiDAR can provide high-resolution topographic maps and highly accurate estimates of the plant height, cover, and canopy structures [51,52,53].

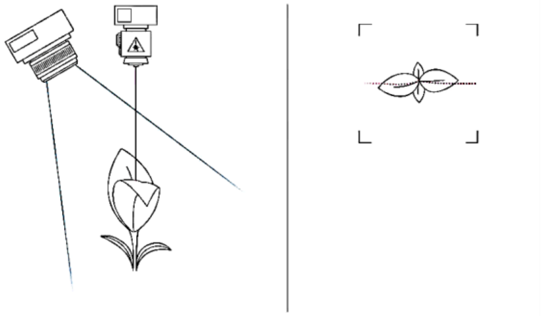

Figure 2-1. LiDAR (https://phenospex.com)

In addition, detecting and tracking organs in plants (e.g., leaf, stems, flowers, and fruits) have been attracting many plant scientists. Automated and high-throughput phenotyping for monitoring barley organs was proposed by [51]. Their results showed that this method is capable of the detection of water stress in barley. Data from several related studies suggest that LiDAR also is a useful tool for the correctly estimating leaf area index [54] and aboveground biomass [55]. Together, these studies indicate that, although LiDAR brings many benefits to handle the challenges currently in plant phenotyping, it still has some shortcomings of throughput, cost, and complex.

Many studies have also implemented terrestrial laser sensors for 3D biochemical and structural features. A terrestrial 3D laser scanner [57] was adopted to measure the aboveground biomass and growth stages of some juvenile trees over time in the indoor environment. By using a Perceptron V5 laser scanner, authors in [51] illustrated a method of automatically monitoring barley plant's structure of leaves and stems. Their approach also enables applicability for detecting and monitoring of drought effects on the 3D structure of plants. Recently, terrestrial laser scanner based approaches [53] were presented to measure canopy height growth and architecture of different crops (such as maize, soybean, and wheat) under field conditions with a high temporal resolution. Moreover, their method can compute and analyze some other plant parameters, such as canopy volume, leaf angle distribution, and height positions of leaves and ears. Beside LiDAR and terrestrial laser sensors, 3D triangulation laser scanner is also used to measure 3D distributions of plants. One study by [58] examined the interactive effects of 3D triangulation laser scanner settings (exposure time) and leaf properties. They found that laser triangulation sensors offer the highest accuracy and the highest resolution of all currently available 3D imaging techniques for plant phenotyping, but their cost is still relatively high and their accuracy can be reduced by nonbiological surfaces on the plant. On the other study, 3D triangulation laser scanner [11] was used to examine daily changes in plant growth of rapeseed plants with high precision in challenging environments. Their results have revealed that this technique is appropriate for high-precision phenotyping in plant breeding. Considering all of this evidence, it seems that laser sensor techniques are well 3D phenotyping tools with high precision, resolution, and throughput.

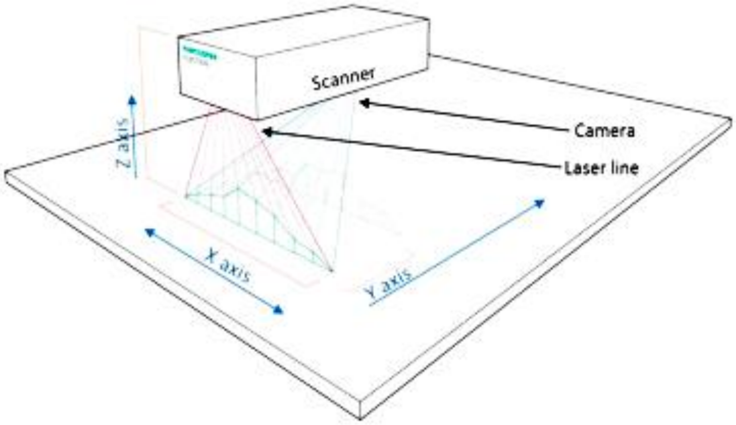

Figure 2-2. A draw of the 3D scanner

Besides the laser sensors, stereo vision techniques also popular deployed in phenotyping for measuring 3D geometry information. Stereo vision has two types, passive and active. Passive stereo vision offers the depth information by searching the correspondence between the images taken by the cameras and then doing triangulation. In contrast to the passive stereo, an active stereo vision emits structured light onto the object and then captures the reflected pattern to compute the 3D geometry of the object surface [6]. Many studies found that stereo vision successfully used to reconstruct 3D models of plants in indoor and outdoor environments. A multi-view stereo vision system was well deployed to extract 3D features, such as plant height and total leaf area of whole plants [49]. This system also offered the capacity to produce high-resolution 3D models to allow highly accurate feature extraction of whole plants in indoor and outdoor scenarios. A recent study described in [55] involved a low-cost and portable stereo vision system in generating dense and accurate 3D imaging of plants in three different environments, including an indoor lab, open field with grass, and a multi-span glass greenhouse.

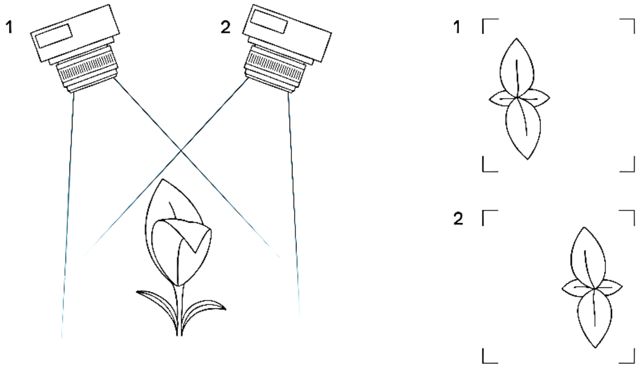

Figure 2-3. A stereo camera

At larger scales in the field phenotyping, a multiple-camera system was successfully deployed for 3D plant phenotyping to produce 3D plant models of sunflowers with plant height, plant volume, leaf count, leaf size, and internode distance [58]. In field operations, stereo vision performance is not only directly affected by the ambient lighting conditions (such as high sunlight, overcast sky, or partial clouds), but also limited by the stereo matching process which is not robust to all sorts of surfaces and objects expected in the field. This stereo vision reduces its potential and limits either the scope or the scale of the application [6]. To deal with these limitations, a shade or polarized filter was used. The advantages of the stereo vision are high-resolution color images and relatively small and low priced. However, the precision and maximum depths are limited by the baseline between the cameras and the distance between the camera and the plant [16]. Collectively, these studies outline a critical role for stereo vision techniques in 3D plant modeling with high resolution, small size, and low cost, but some limitations of illumination conditions and matching process are needed to concern.

Similar to laser sensor and stereo vision, Time-of-Flight (ToF) technology is also adapted to measure 3D plant traits from controlled environments to fields with all scales. A ToF camera is a range imaging system that calculates the distance based on the known speed of light, measuring the time of the light that travels between the sensor and the targeted object. These ToF cameras use near-infrared emitters and mostly offer low-resolution depth images. They can offer a high frame rate (up to 160 fps) (e.g., Argos3D-Pxx, https://bluetechnix.com) and are highly suitable for real-time applications. However, some of them are not suitable to use under intense sunlight.

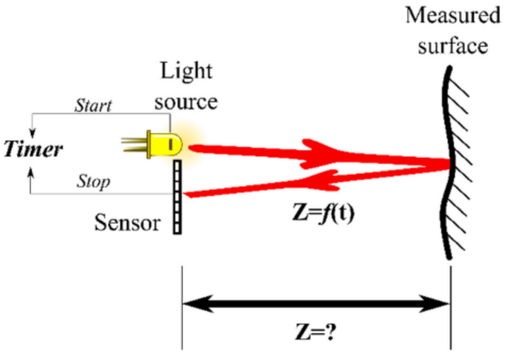

Figure 2-4. The fundamental principle of time-of-flight camera

In plant science, ToF cameras are used to measure 3D traits of plants. Authors in [60] used ToF cameras for automated phenotyping of maize plants under outdoor conditions. Their results showed that their approach enables to detect and distinguish different leaves and leaf size. In a similar study, authors in [61] investigated a method for monitoring and modeling plant leaves using both ToF and color cameras. Their results showed that this approach provides a useful enough 3D approximation for automated plant measuring at the high throughput. The study of an inter-plant spacing by using a TOF camera was carried out in [62]. They demonstrated that the use of 3D vision system could accurately measure the spacing between the corn plants in early growth stages, however low resolution and sensitivity to strong sunlight become main obstacles for depth camera applications. In another related experiment conducted by [63], a multisensory system, including a ToF camera that offered fast acquisition of depth maps, was developed to detect and locate fruits from different kinds of crops in natural scenarios. The studies presented thus far provide evidence that ToF technique is a powerful tool for 3D plant traits measurements with high frame rate and high throughput, but low resolution and high sensitivity of illumination.

Finally, low-cost depth cameras Microsoft Kinect also were applied for 3D phenotyping in controlled environments and field conditions. Many studies have been investigated to assess different applications of Kinect sensors in plant science. Authors in [64] used a Kinect V1 to capture 3D shapes of sugar beet taproots, sugar beet leaves, and wheatears. The volumetric shape of sugar beet taproots and their leaves were reconstructed to compare with the other cameras. They suggested that the low-cost depth sensor could replace some alternative high-cost sensors in some scenarios. In another study, a Kinect V2 sensor is used for robotic weeding in [13]. This system allows the weeding robot to detect ground and single plants in crop rows. In the indoor environment, a Kinect sensor was applied for automatically detecting and segmenting stems of tomato plants [65]. In a practical approach, a Kinect-based method was developed for 3D measurement of strawberries and investigated the measurement accuracies of plant height, width, and the area of leaves using a potted strawberry plant [66]. These studies provide valuable insights into the use of Microsoft Kinect cameras for 3D phenotyping, these low-cost depth cameras offer some benefits in plant phenotyping, but they still have some limitations such as low resolution and highly sensitive to outdoor lighting conditions.

2.4 Some High Throughput Phenotyping Platforms

Most of the high throughput phenotyping platforms (HTPPs) around the world have been popularly implemented in controlled environments and fields with all scales for measuring overall growth and development of different plants. In growth chambers or greenhouses, HTPPs are fully automated and high-speed platforms that supported by robotics, precise environmental control, remote sensing systems, and high-performance computing systems to monitor and analyze plant traits. Although these platforms are definitely deployed for research and large-scale phenotyping purposes, they are only used for a limited range of species, including small plants. For example, these small plants are Arabidopsis thaliana [67,68] and primary cereal crops such as barley [69]. There is a consensus among crop scientists that controlled environments are far from the real situation where plants will experience in the field, thus they cannot extrapolate to the field situations [70,71,72]. These limitations of environmental factors are known, such as soil volume, sunlight, wind speed, CO_2 level, air humidity, temperature, and evaporation rate. These obstacles lead to unreliable results of accessing plant responses, for example, effects of stresses during plant growth stages, especially in reproductive growth. On the other hand, these HTPPs are relatively expensive.

By combining advanced in imaging techniques, aerial to ground-based devices, and high-performance computing facilities, field-based HTPPs are recognized as reliable approaches to measure a large number of plants and describe relevant phenotypic traits in natural scenarios. There are varieties of vehicle-based HTPPs used for plant phenotyping in the fields, such as ground-based phenomobiles, stationery phenotowers, and unmanned aerial vehicles. These platforms have been recently deployed by plant research institutes or big seed companies, such as:

- The Australian Plant Phenomics Facility (http://www.plantphenomics.org.au),
- The International Plant Phenomics Network (https://www.plantphenomics.com),

- The USDA (https://nifa.usda.gov, https://www.ars.usda.gov),
- The European Plant Phenotyping Network (http://www.plant-phenotyping-network.eu/eppn/structure),
- The German Plant Phenotyping Network (http://www.dppn.de),
- The LemnaTec (http://www.lemnatec.com),
- PHENOPSIS (http://bioweb.supagro.inra.fr/phenopsis/InfoBDD.php),
- PhenoFab (http://www.keygene.com).

A number different ground-based platforms, named as phenomobiles, include farming vehicles (e.g., tractors, sprayers, robots) equipped with multiple sensors and a global positioning system (GPS), are developed to measure plant architecture, canopy height, reflectance, and temperature [13,70,72,73]. Some others focused on phenotyping for tall dense canopy crops such as sorghum [74]. The other types of ground-based platforms are known as fixed gantry systems [75,76,77]. The fixed gantry systems carrying multiple sensors are used for tall crops that move along the designated area in the research field. Although ground-based platforms offer great potential to revolutionize the field of plant phenotyping, they still meet several significant obstacles such as high cost of construction and operation and are limited in the size of the breeding plots.

As ground-based platforms are impossible to simultaneous measurements of all plots within a trial, aerial-based platforms equipped with different sensors are emerging as an alternative option. These platforms include small airplanes or helicopters, blimps, and unmanned aerial platforms (UAPs). They enable a fast and non-destructive high throughput phenotyping approach with high spatial resolution, flexible, and convenient in operation. These systems also provide the ability to rapidly phenotype a large number of plots and field traits in relatively short periods of time. A number of published studies shown that these platforms have been widely deployed in the field for measuring canopy height [78], crop yield forecasting [79], disease and pets detection [79], etc. The current aerial-based platforms are flexible to use for specific phenotyping purposes depending on their payload, initial costs, maintenance costs, and control. Aerial platforms increasingly become the most popular method of field phenotyping because they are easy to deploy and can collect data over a long distance within a short time span. However, they are faced with size, weight, power, and sensor resolution. These studies suggest that HTPPs are power tools for automatic and high throughput 3D phenotyping covering all environments and all scales. Each of them can be fit for one or several environments and depends on the budget.

2.5 Image Fusion Techniques

Image fusion is a technique that combines many different images to generate a fused image with highly informative and reliable information. There are several image fusion types, such as multi-modal, multi-sensor, and multi-focus image fusion. In multi-modal image fusion, two different kinds of images are fused, for example, combining a high-resolution image with a high color image. In multi-sensor image fusion, images from different types of sensors are combined, for example, combining an image from a depth sensor with an image from a digital sensor. In multi-focus image fusion, two or more images captured by the same sensor from the same visual angle but with a different focus are combined to obtain a more informative image. For example, a fused image with clearer canola seedpods can be produced by fusing many different images of a canola plant acquired by the same Pi camera at the same angle with many different focus lengths.

Image fusion methods can be grouped into several levels depending on the image-fusion processing methods. These image fusion methods can be divided into three levels, such as the pixel level, feature level, and decision level. Image fusion at the pixel level refers to an imaging process that occurs in the pixel-by-pixel manner in which each new pixel of the fused image obtains a new value. At a higher level than the pixel level, feature-level image fusion first extracts the relevant key features from each of the source images and then combines them for image-classification purposes such as edge detection. Decision-level image fusion (also named as interpretation-level or symbol-level image fusion) is the highest level of image fusion. Decision-level image fusion refers to a type of fusion in which the decision is made based on the information separately extracted from several source images.

Over two decades, image fusion techniques have been widely applied in many areas, such as medicine, mathematics, engineering, and physics. In plant science, many image fusion techniques are used to improve the classification accuracy for determining plant features, detecting plant diseases, and measuring crop diversification. Authors in [80] well implemented a Kalman filtering fusion to improve the accuracy of the prediction on the citrus maturity. In related research, a feature-level fusion technique [81] successfully developed to detect some types of leaf disease with excellent results. In other similar research, apple fruit diseases were detected by using feature-level fusion in which two or more color and feature textures were combined [82]. Besides these feature-level fusion techniques, decision-level fusion techniques combined with other techniques have been used for early detection and characterization of agricultural food crop contamination and infestation in the field. The decision-level fusion technique has resulted in high detection rates. While decision-level fusion techniques have been deployed to detect crop contamination and plague [83], authors in [84] have also implemented the Ehler’s fusion algorithm (decision level) to measure the diversification of the three critical crop systems with the highest classification accuracy. These findings suggest that image-fusion techniques at many levels are broadly applied in the plant science sector because they offer the highest classification accuracy.

CHAPTER 3 - METHODOLOGY

This section describes the related techniques and methodologies deployed in designing a low-cost depth mobile platform for canola phenotyping, counting canola branches and seedpods, and fusing color images for the thesis as follows: the requirements and specifications of the proposed approach (Section 3.1); the proposed approaches for counting canola branches and seedpods, estimating canola plant height, and fusing multi-focus color images (Section 3.2); image-processing algorithms for counting canola branches and seedpods, estimating canola plant height, and fusing multi-focus color images (Section 3.3).

3.1 Requirements and Specifications

3.1.1 Project Requirements

To meet the goal of the project “Field-Based High-Throughput Phenotyping Mobile Systems for Crop Monitoring” of the University of Saskatchewan being to develop a high-throughput mobile platform for the rapid assessment of plant traits, requirements of a mobile system were proposed. This system must be a non-invasive plant phenotyping system, which can be mounted on mobile vehicles, such as swathers, sprayers, and tractors. In both controlled and field environments, the system must operate continuously for at least two hours in the ambient temperatures from 5 °C to 45 °C and moving speeds in the range from 1 to 1.5m/s.

3.1.2 Materials Used

In this study, a mobile platform, including an Argos3D-P100 camera, a Pi camera, a Raspberry Pi3, a remote-control system, and a 12V battery, was developed. In addition, a Kinect V2 and a Sony A58 camera were also used in our experiments. For our experiments, the subjects of the study are canola plants growing in the controlled environments and in the fields.

3.1.3 System Requirements

The proposed mobile platform was designed as shown in Figure 3-1. This system can be fixed on a bracket that mounted on the boom of the swather or sprayer.

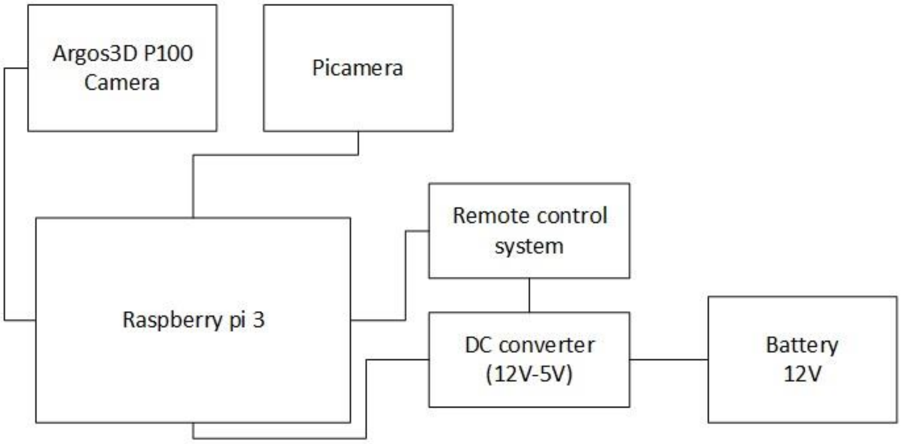

Figure 3-1. A concept design of the proposed phenotyping mobile system

3.1.4 Energy Requirements

The system must be operated for at least two hours per day without recharging the battery. The currents of the proposed system when starting and capturing images are 0.61 A and 0.95 A, respectively. Due to the power requirements of the whole system, at least 2h*12 V*0.95 A = 22.8 Ah was needed.

3.1.5 Storage Requirements

The storage space is required to be large enough for the operating system and data acquired from both cameras. The operating system is required to be at least 2 GB. The streams and videos acquired from Argos3D P100 and Pi cameras at 10 frames per second are about 1.468MB/s and 0.92MB/s (with a resolution of 1640 x 1232 pixels). For two hours, a minimum storage space of 17.2 GB is needed. As the result, at least 19.2 GB of total storage space is required.

3.2 The Proposed Approaches

3.2.1 Detection and Counting Canola Branches

The proposed approach has several advantages: a low-cost depth camera system, a high-throughput 3D phenotyping system, and multi-platform capability. The low-cost depth camera (Argos3D-P100) is used as an imaging acquisition system. Comparing with other advanced depth cameras, such as a laser camera, this ToF camera is suitable for our platform due to its cost, size, and ability to capture both 3D and 2D images for counting canola branches. With this ToF technology camera, phenotypic traits (e.g., canola plant height and number of branches) can be directly extracted and measured. In addition, the ToF Argos3D-P100 camera can capture depth map and 160x120 pixels data with up to 160 fps to deliver depth information and grayscale data for each pixel simultaneously. The data received from the depth camera is small enough to improve phenotyping process as well as increase the storage capacity. Also, the proposed system can be deployed on two different imaging platforms: controlled environments (chambers or greenhouses) and field scenarios. With the controlled platforms, the proposed system can be fixed, and the plant is turned around the camera system, or the proposed system is moved around a stationary plant. In the field, the proposed system can be mounted on a vehicle (e.g., swather, sprayer, or tractor) that moving over the field plots.

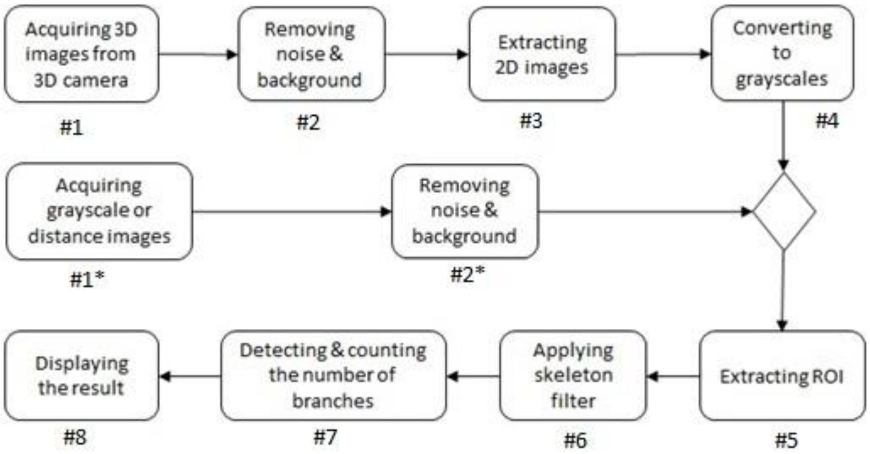

Figure 3-2. The workflow of the proposed approach for counting canola branches

The process of detecting and counting canola branches includes eight steps as described by the workflow shown in Figure 3-2. There are two ways to count the canola branches, using 3D point cloud data or using grayscale data acquired from the Argos3D P100 camera. The method of counting the canola branches by using 3D point cloud data is described as follows. First, the canola depth and grayscale information are acquired by a 3D camera (Argos3D-P100 or Kinect V2) that mounted on the tripod while the plant is turned around on the turntable device. In the next step, a 3D size filter is applied to remove the noise and background. From the filtered 3D images, 2D images are extracted in the third step. Before extracting the area of interest (ROI), containing stems and branches, the images are converted to grayscale images in step 4 or the distance and grayscale information acquired from depth camera can be directly used in step 5. After that, a fast-marching method in step 6 is deployed to obtain the skeleton of the plant before detecting and counting canola branches in step 7. Finally, the results of counting number of canola branches are displayed in step 8.

On the other hand, another method of counting the canola branches by using grayscale data is simpler than the first one. Instead of implementing first four steps as mentioned above, only two steps are implemented, including acquiring grayscale images and removing the noise and background steps. These next steps are implemented as similar as the first one did. The diamond block indicates the options that each of methods can be done.

3D point cloud, distance, and grayscale images are taken by using the Argos3D P100 and Kinect V2 cameras in an indoor environment. The resolution of images adopted by the Argos 3D P100 and Kinect V2 is 160x120 pixels and 512x424 pixels, respectively. These depth images are captured under different views with a distance of 50 cm from the plant. Matlab R2016b, Argos3D-P100 SDK, and Kinect V2 SDK are used to connect the depth cameras with a PC, support to the acquiring data process, process the data, and display the results.

3.2.2 Detection and Counting Canola Seedpods

To detect and count canola seedpods from single canola plants, a 2D image-based approach is to be developed to extract seedpod features from the color side view of the images in the laboratory as illustrated by the workflow in Figure 3-3. In this approach, a digital camera is employed to capture color side view images of the canola plants. Then, these color images are converted to grayscale images. Next, a Frangi 2D vesselness filter algorithm [85] is applied to detect tube-like structures of stems and branches from these grayscale images. Although the Frangi vesselness filter produces an excellent result, the remaining noise is required to be removed before obtaining the skeleton of the canola plant. Following the previous step, a skeleton algorithm – multi-stencils fast marching method [100] is adopted to retrieve the skeleton of the plant. After that, an algorithm for detecting endpoints of the given skeleton is deployed to find locations of the endpoints of the skeleton. Finally, from these end-point locations, canola seedpods can be detected, and the number of canola seedpods can be estimated and displayed as well.

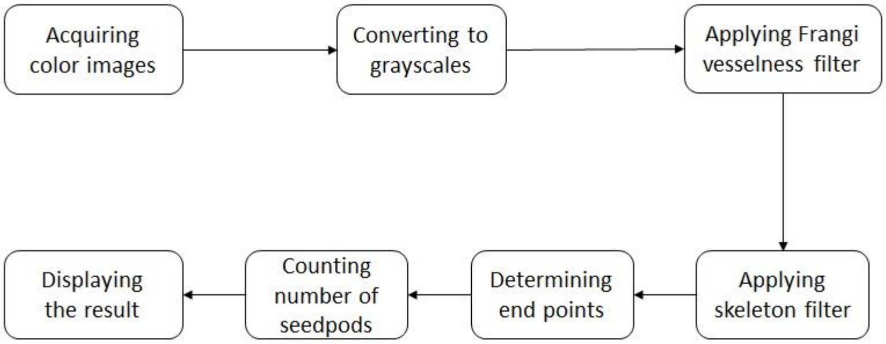

Figure 3-3. The workflow of the proposed approach for counting canola seedpods

Color images are taken by the Pi and Sony A58 cameras in the indoor environment. The resolution of images acquired by the Pi camera and Sony camera are 1640 x 1232 pixels and 3872 x 2576 pixels, respectively. These color images are obtained under different side views at a distance of 50cm for the Pi camera and 180 cm for the Sony camera. Matlab R2016b is used for software development.

3.2.3 Monitoring Canola Growth Stages

A hybrid of depth and color cameras system is implemented to monitor individual canola plants in early growth stages. The depth, grayscale information, and color images of the canola plants grown in the greenhouse are derived from two leaves to green pod stages. From these images, estimating the height of individual canola plants or canola plots can be implemented. Regularly and accurately monitoring canola plant-growth stages offers a good indication of canola plants for crop researchers and breeders to diagnose problems early.

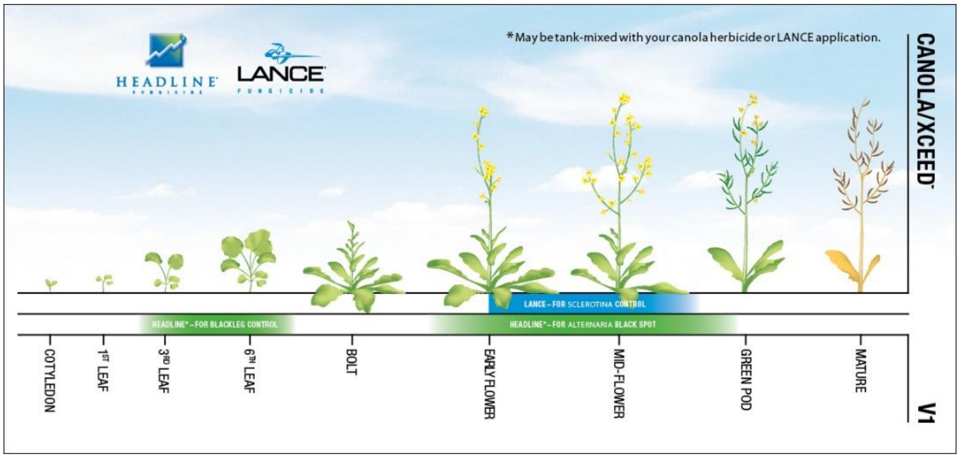

Figure 3-4. Canola growth stages (Taken from www.agsolutions.ca)

To measure plant height of individual canola plants, grayscales or depth images are extracted. Each canola plant is placed underneath the depth camera with a distance between 30mm and 1500mm. Each measurement is executed from 10 to 30 seconds at a frame rate of 10fps in the laboratory. The measurement unit of the depth camera is set to millimeter (mm). To estimate plant height of individual canola plants, depth and amplitudes data of each canola plant are first extracted from the Argos3D's stream, then only depth data are used for plant height measurement. Next, the background and noise of these depth data is removed before extracting the area of interest (where the canola plant is located). Finally, from the depth image, both the distance between the depth camera and the ground truth and the distance between the depth camera and the highest point of the plant are retrieved to calculate the canola plant height.

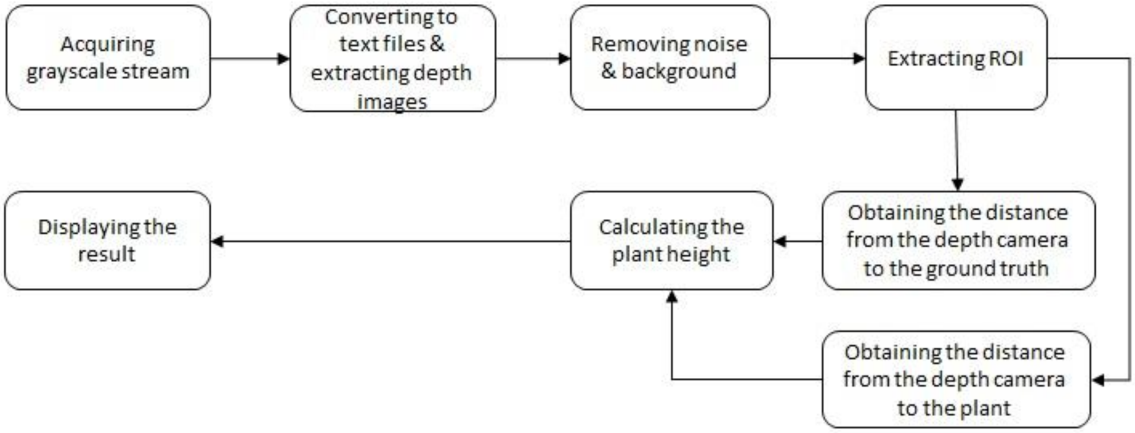

Figure 3-5. The workflow of the proposed approach for plant height measurement

3.2.4 Multi-focus Image Fusion

Because the Pi camera is limited by its low-resolution, this thesis aims to fuse different color images to improve color-image resolution for further plant traits analysis. The Pi camera enabled two types of images, focus-based and exposure-based images. Focus-based images are images acquired with different focuses, in which some part of the image is well focused, while other ones are blurred. Similarly, exposure-based images were those obtained with different exposures, in which some portion of the image was properly exposed, whereas other portions were under- or over-exposed. Due to time constraints, only multi-focus fusion techniques are inspired in this thesis.

Multi-focus image fusion is a type of adaptive image processing technique, in which multiple images with varied focuses are combined to enhance the perception of the scene. The objectives of the multi-focus image fusion are to increase the depth-of-field by extracting partially focused regions from multiple source images and combining them together to produce a single image in which all regions are well focused. Many studies investigated multi-focus image fusion techniques in spatial and frequency domains to improve the outcomes. Authors in [86] proposed a method based on the robust principal component analysis in the spatial domain. They developed this method to form a robust fusion technique to distinguish focused and defocused areas. The method outperforms wavelet-based fusion methods and provides better visual perception, however it has a high computation cost. In the similar spatial domain, a multi-focus image fusion method based on region [87] was developed, in which, their algorithm offers smaller distortion and better reflection the edge information and importance of the source image. Similarly, authors in [88] investigated a fusion technique based on dense scale invariant feature transform (SIFT) in the spatial domain. The method performs better than other techniques in terms of visual perception and performance evaluation but it requires high amount of memory. In the frequency domain, authors in [89] conducted a method based on Discrete Cosine Transform. They computed and obtained the highest variance of the 8x8 DCT coefficients to reconstruct the fused image. In a recently study, the authors in [90] examined a method based on focuses regions detection. Their approach provides great quality in respect of visual and objective evaluation.

To deal with these obstacles, a novel multi-focus image fusion based on the image quality assessment metrics is proposed in this thesis. The proposed approach is illustrated in Figure 3-6. The proposed method of fusion is developed based on crucial image quality assessment (IQA) metrics and a gradient domain fast guided image filter (GDFGIF). This approach is motivated by the fact that visual saliency maps, including visual saliency, gradient similarity, and chrominance similarity maps, outperform most of the state-of-the-art image quality assessment (IQA) metrics in term of the prediction accuracy [91]. Authors in [91] stated that their IQA metrics have the best performance and stable. In addition, gradient domain guided filter (GDGIF) [92] and fast guided filter (FGF) [93] are adopted in this thesis due to the combination of GDGIF and FGF can offer better fused results, especially near the edges, where halo artifacts appear in the original guided image filter. The proposed method first measures visual saliency, gradient similarity, and chrominance similarity and then calculates weight maps from these metrics. Next, these weight maps are refined by a gradient domain fast guided image filter. Then, the source images are decomposed into base and detail layers. The base and detail layers contain the large-scale variations in intensity and the small-scale variations in intensity, respectively. Finally, the fused image is directly obtained from the refined weight maps and two-layer-decomposed images. The workflow of the proposed approach was described in Figure 3-6. The details of the proposed algorithm will be introduced in the next section.

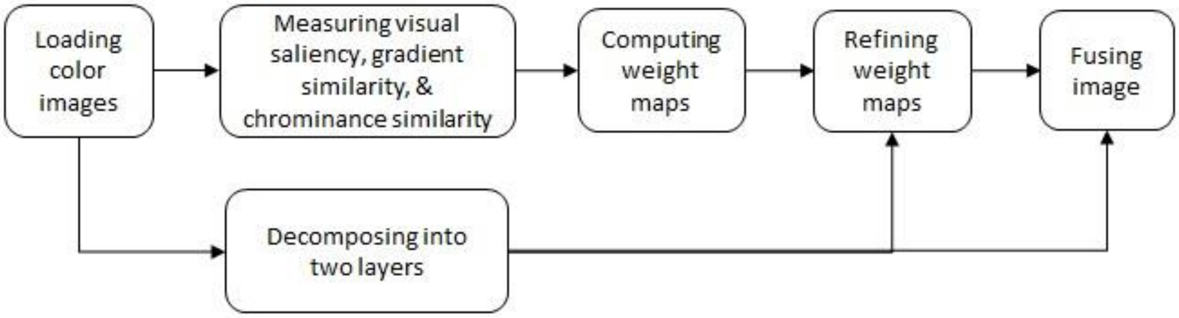

Figure 3-6. The proposed approach for multi-focus image fusion

3.3 Image Processing Algorithms

3.3.1 Frangi Vesselness Filter

Canola seedpods are required to be detected and counted from the acquired color images. The color of the canola seedpods, stems, and branches may range from green to brown. They appear as significant vessel structures in the acquired images. Property of vesselness is better than the property of color for identifying canola seedpods in the color images. Authors in [85] developed a method for vessel enhancement filtering based on Hessian matrix eigenvalues to identify tube-like objects. Their method has been applied and is popular in medical areas to identify such anatomical features as blood vessels, vascular trees, pulmonary vessels, and retinal vascular networks from medical images. In plant science, the Frangi filter was applied for automatically detecting and counting Hibiscus branches from color images [94], automatically measuring internode length of cotton plants [95] and estimating stem width of sorghum plants [96].

Due to these advantages of the Frangi vesselness filter mentioned above, the vesselness measurement technique is adopted in this study to detect and count the number of canola seedpods. From the Frangi's method, Hessian-based multiscale filtering is adopted for enhancing vascular structures in the medical image. This filter is based on eigenvalue analysis of the scale space of the Hessian matrix. The eigenvalues and eigenvectors of Hessian matrix are closely related to tube-like intensity and direction. For 2D images, the Hessian matrix is a 2x2 matrix, including second order partial derivatives of the input image, described as below

$$H(x,y) = \begin{bmatrix} \frac{\partial^2 I}{\partial x^2} & \frac{\partial^2 I}{\partial x \partial y} \\ \frac{\partial^2 I}{\partial y \partial x} & \frac{\partial^2 I}{\partial y^2} \end{bmatrix} \quad (3.1)$$

where $I(x,y) = \frac{\partial^2 I}{\partial x \partial y}$ is the intensity value of a pixel (x, y) in the image *I*. To obtain the Hessian matrix elements - the second order partial derivatives of the image, *I(x, y), I(y, x),* and *I(y, y)* need to be computed. The second partial derivatives of an input image *I* at the pixel (x, y) can be calculated by the convolution with derivatives of the Gaussian filter at a standard deviation (σ), as defined as

$$I(x, y, \sigma) = G(x, y, \sigma) * I(x, y) \quad (3.2)$$

$$G_{(x,y,\sigma)} = \frac{1}{2\pi\sigma^2} e^{-\frac{x^2+y^2}{2\sigma^2}} \quad (3.3)$$

where *G(x, y, σ)* is a Gaussian convolution kernel at scale σ, as mentioned in Equation (3.3). When the standard deviation is changed, vessel structures with different widths can be obtained. When increasing the value of sigma (σ), the wider lines of the vessel can be identified.

Let the eigenvalues of Hessian matrix be λ_1, λ_2 and $|\lambda_1| \leq |\lambda_2|$, and their corresponding eigenvectors are e_1 and e_2, respectively. The relationships between λ_1, λ_2, and orientation of different structures in the images are described in Table 3-1.

Table 3-1. Eigenvalues and orientation patterns

Eigenvalues		**Orientation pattern**
λ_1	λ_2	
L	H-	Tubular structure (bright)
L	H+	Tubular structure (dark)
H-	H-	Blob-like structure (bright)
H+	H+	Blob-like structure (dark)

L = Low, H = High, and +/- indicate the sign of eigenvalues. The eigenvalues are ordered by $|\lambda_1| \leq |\lambda_2|$.

Eigenvalues of the Hessian matrix (H) are calculated to extract about contrast and principal direction information from the image. They can be used to detect the vessel region [85]. The eigenvalues decide which pixel belongs to a ‘tubular structure’ or a ‘blob-like structure’ of the vessel. Since λ_1 is the eigenvalue of smallest magnitude, pointing in the direction of smallest curvature and λ_2 is the eigenvalue of largest magnitude, pointing in the direction of the largest curvature. For example, a combination of a small value of λ_1 and a large value of λ_2 indicates that this pixel belongs to a tubular structure. However, if λ_1 changes to a large value, that pixel will belong to a blob-like structure. Eigenvalues have two signs (+) and (-) that they indicate the darkness and brightness of the tube structure, respectively.

The vesselness is a measurement of the probability of the pixel belonging to the stem, branches, and seedpods of the plant, which similar to the blood vessel as described in [85]. The vesselness measure includes two factors, blobness measure - R_β and the second order structureness - S. Based on the eigenvalues λ_1 and λ_2, R_β and S are calculated as follows

$$R_\beta = \frac{\lambda_1}{\lambda_2} \tag{3.4}$$

$$S = \sqrt{{\lambda_1}^2 + {\lambda_2}^2} \tag{3.5}$$

where R_β is the blobness measurement in 2D images and accounts for the eccentricity of the second order ellipse. It has low value for tubular structures than blob-like structures. S is the second order structureness. S is defined by a Frobenius norm of the Hessian matrix to reduce the response of the background [85]. The second order structureness will be low in the background where no structure is present, and the eigenvalues are small for the lack of contrast. In regions with high contrast compared to the background, the norm will become larger since at least one of the eigenvalues will be large [85]. The vesselness measure can be calculated from blobness measure and the second order structureness as given by

$$v_0 = \begin{cases} 0, & if \;\; \lambda_2 > 0, \\ \exp\left(-\frac{{R_\beta}^2}{2\beta^2}\right)\left(1 - \exp\left(-\frac{S^2}{c^2}\right)\right), & otherwise, \end{cases} \tag{3.6}$$

where β and c are weight factors, which control the sensitivity of the filter to the measures R_β and S. Authors in [85] integrated the vesselness measure provided by the filter response at different scales to obtain a final estimate of vesselness. According to authors in [85], the idea behind this expression is to map the features in Equations (3.4) and (3.5) into probability-like estimates of vesselness according to different criteria. They combined the different criteria using their product to ensure that the response of the filter is maximal only if all three criteria are fulfilled. In their experiments, β was fixed to 0.5. The value of the threshold c depends on the grey-scale range of the image and half the value of the maximum Hessian norm has proven to work in most cases [85]. As a result, the maximum response is accepted to be a final measurement of vesselness, is defined by

$$v_0(\Upsilon) = \max_{\sigma_{min} \le \sigma \le \sigma_{max}} \{v_0(\sigma, \Upsilon)\} \tag{3.7}$$

where $\sigma_{\min}$ and $\sigma_{\max}$ are the minimum and maximum scales at which relevant structures are expected to be found. They can be chosen that they will cover the range of vessel widths. This filter can be used at different scales that are able to offer a result in a larger range of line sizes. However, its performance depends on the scales ($\sigma_{\min}$ and $\sigma_{\max}$) to be chosen.

3.3.2 Multi-stencils Fast Marching Method

Because the branches and seedpods of the canola plants are too small and thin, detecting and counting canola branches and seedpods bring many obstacles for crop researchers. From their characteristics, an idea to deal with this is to find the skeleton of the canola plant, then apply other detecting and counting algorithms. The skeleton describes simple and compact shapes of a plant with all features of the original plant. An example of the skeleton of a plant is shown in Figure 3-7.

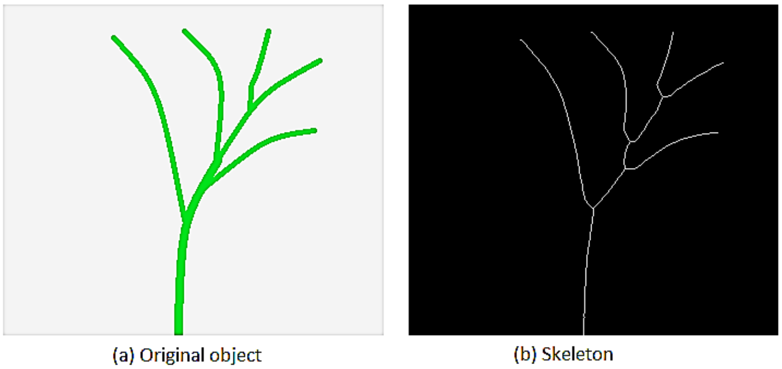
(a) Original object

(b) Skeleton

Figure 3-7. General concept of skeleton

Skeletonization algorithms can be classified into four main categories, morphological thinning algorithms, Voronoi diagram based algorithms, distance transform based algorithms, and mathematical morphology based on algorithms [98]. These morphological thinning methods iteratively remove the boundary layer by layer and can preserve the object topology. However, they are sensitive to the boundary noise and do not generate a true skeleton. Geometric approaches calculate the Voronoi diagram of a discrete polyline like a sampling of the boundary. These methods result in an accurately connected skeleton by increasing the sampling rate, but relatively complicated to implement as well as computationally expensive. Authors in [99] reviewed some algorithms used mathematical morphology for skeleton calculation, such as using influence zones and setting operations to transform a discrete binary image using parts of its skeleton containing complete information about its shape and size. The limitations of such methods are that their outcomes depend on structure elements used for mathematical morphology operations. Also, the resulting skeletons may not preserve connectedness. The distance transform methods calculate the shortest distance from a given point to the object boundary. Approaches based on distance transform are expected to show a better performance under rotation and at sharp corners due to the robust underlying strategy of using the distance transform or depth measure, in defining the peel sequence [99]. Therefore, distance transform-based approaches have been studied, especially; a high accuracy fast marching method was used.

Fast marching methods are techniques designed to solve the Eikonal equation ($T_i^2 + T_j^2 = 1/F_{\{i,j)}^2$, where T is travel time, ij represent Cartesian coordinates) for detecting the evolution of a monotonically advancing front. These approaches produce consistent, accurate, and highly efficient algorithms due to entropy-satisfying upwind schemes and fast sorting techniques. There are several improved fast marching methods, such as the Higher Accuracy Fast Marching, Untidy Fast Marching, Shifted Grid Fast Marching, and Multi-stencils Fast Marching (MFM) methods. These methods have been introduced to enhance the accuracy of predictions. Most of all algorithms, except the MFM algorithm, ignore information of nodes in the diagonal direction while considering only the 4-connected neighboring nodes in the 2D plane; therefore, they cause significant numerical errors along the diagonal directions. By utilizing information from all neighboring nodes (8-connected neighbors), the MFM algorithm solves this obstacle. The algorithm proposed by [100] is applied in this study because this technique improves version of the MFM that is highly accurate. This method computes the solution at each grid point by solving the Eikonal equation along several stencils that cover the entire nearest neighbors of the point and then picks the solution that satisfies the upwind condition. In addition, the accuracy of the MFM approach is further improved by using second-order finite difference schemes from the Eikonal equation.

In the MFM algorithm, the computation of the arrival time $T_{i,j}$ includes two different equations; the nearest neighbor points are covered by S_1, whereas the diagonal neighbor ones are covered by S_2.

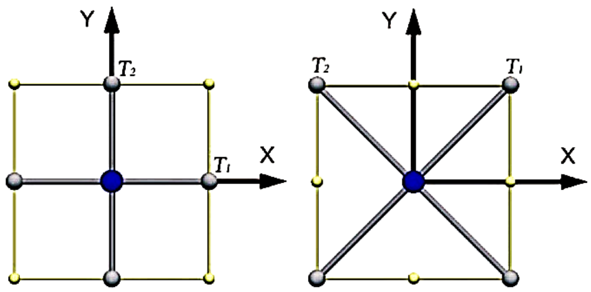

(a) (b)

Figure 3-8. The stencils for the 2D Cartesian domain. (a) S_1 stencil and (b) S_2 stencil

- *S_1 stencil computation:* Assuming we have a regular grid, the first-order equation of this stencil aligned with the natural coordinate system is solved by the following equation:

$$\sum_{v=1}^{2}\max\left(\frac{T_{i,j}-T_v}{h},0\right)^2 = 1/F_{i,j}^2, \tag{3.8}$$

where $\Delta i = \Delta j = h$ is the distance between nodes and

$$T_1 = \min\left(T_{i-1,j}, T_{i+1,j}\right), \tag{3.9}$$

$$T_2 = \min(T_{i,j-1}, T_{i,j+1}). \tag{3.10}$$

On the other hand, for a second-order approximation of the directional derivative, this equation must be solved:

$$\sum_{v=1}^{2}\max\left(\frac{3}{2h}\left[\frac{T_{i,j}-T_v}{h}\right],0\right)^2 = 1/F_{i,j}^2 \tag{3.11}$$

where

$$T_1 = \min\left(\frac{T_{i-1,j}-T_{i-2,j}}{3}, \frac{T_{i+1,j}-T_{i+2,j}}{3}\right) \tag{3.12}$$

$$T_2 = \min\left(\frac{T_{i,j-1}-T_{i,j-2}}{3}, \frac{T_{i,j+1}-T_{i,j+2}}{3}\right) \tag{3.13}$$

- *S_2 stencil computation*: Similar to the previous case, for a first-order approximation of the diagonal equations, the following equation is solved:

$$\sum_{v=1}^{2}\max\left(\frac{T_{i,j}-T_v}{\sqrt{2}h},0\right)^2 = 1/F_{i,j}^2, \tag{3.14}$$

where

$$T_1 = \min\left(T_{i-1,j-1}, T_{i+1,j+1}\right), \tag{3.15}$$

$$T_2 = \min(T_{i+1,j-1}, T_{i-1,j+1}). \tag{3.16}$$

and the second order equation is given by:

$$\sum_{v=1}^{2} \max\left(\frac{3}{2\sqrt{2}h}[T_{i,j} - T_v], 0\right)^2 = 1/F_{i,j}^2 \tag{3.17}$$

where

$$T_1 = \min\left(\frac{T_{i-1,j-1} - T_{i-2,j-2}}{3}, \frac{T_{i+1,j+1} - T_{i+2,j+2}}{3}\right) \tag{3.18}$$

$$T_2 = \min\left(\frac{T_{i+1,j-1} - T_{i+2,j-2}}{3}, \frac{T_{i-1,j+1} - T_{i-2,j+2}}{3}\right) \tag{3.19}$$

For both stencils S_1 and S_2, if

$$T_{i,j} > \max(T_1, T_2) \tag{3.20}$$

then (3.8), (3.11), (3.14), and (3.17) can be simplified to

$$g(h) \sum_{v=1}^{2} a_v (T_{i,j})^2 + b_v T_{i,j} + c_v = \frac{1}{F_{i,j}^2} \tag{3.21}$$

where

$$[a_v \quad b_v \quad c_v] = [1 \quad -2T_v \quad T_v^2] \tag{3.22}$$

The value of *g(h)* for the first and second-order numerical schemes, as well as the stencil orientation, is given in Table 3-2.

Table 3-2. Values of first and second-order schemes

Stencil	First order scheme	Second order scheme
S_1	$g(h) = 1/h^2$	$g(h) = 9/4h^2$
S_2	$g(h) = 1/2h^2$	$g(h) = 9/8h^2$

- *Upwind condition:* As a result, the upwind condition is given by the following equation:

$$|T_1 - T_2| < \frac{f(\Delta i, \Delta j) \sin \emptyset}{F_{i,j}} \tag{3.23}$$

The value of $f(\Delta i, \Delta j)$, for the first and second-order numerical schemes, as well as the stencil orientation, is given in Table 3-3.

Table 3-3. Coefficients of the upwind condition for both S_1 and S_2

Stencil	**First order scheme**	**Second order scheme**
S_1	$f = \min(\Delta i, \Delta j)$	$f = 2\min(\Delta i, \Delta j)$
S_2	$f = \sqrt{\Delta^2 i + \Delta^2 j}$	$f = 2\sqrt{\Delta^2 i + \Delta^2 j}$

3.3.3 Size Filter

Even though the Frangi vesselness filter offers excellent results for detecting vessel in images, it still leaves unwanted small objects in the outputs. To remove these unwanted small objects, a morphological size filter is applied.

3.3.4 Finding the Area of Interest (ROI)

Before finding the skeleton of stems and branches of the canola plant, the other parts of the plant are not necessary to keep, and then they must be removed. Simply, a bottom-most pixel will be found, and then a region of interest polygon will be converted to a region mask. From that region mark, regions of stems and branches are selected.

3.3.5 Detecting and Counting Number of Branches

Detecting and counting number of branches are based on the skeleton of the given ROI of the plant that obtained by using a multi-stencils fast marching method. This fast marching algorithm is used to find the skeleton of the ROI, including stems and branches and to mark them by different colors. From these findings, the number of canola branches is estimated. This algorithm is illustrated, as shown in Figure 3-9.

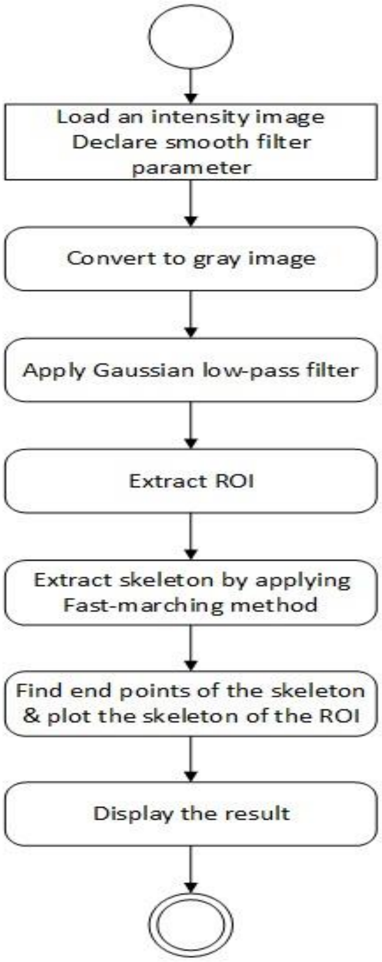

Figure 3-9. The proposed algorithm for detecting and counting canola branches

3.3.6 Detecting and Counting Number of Seedpods

To detect and count the number of canola seedpods, the color images of the canola plant are acquired by different views. Then, the Frangi-vesselness and size filters to remove the background and noise are applied to these color images. Next, by applying the multi-stencils fast marching method, a skeleton of the canola plant is obtained. From this skeleton, an algorithm is developed to find the end-points of the skeleton, in which the number of seedpods can be estimated. The algorithm for determining end-points of the skeleton finds the locations of endpoints in the given skeleton, in which, all coordinates are extracted. All of the coordinates are tested to determine which one is an island that had only one neighbor pixel. Finally, these island pixels are collected that all of them are seedpods and spikes. To obtain more accurate results of the counting canola seedpods, the number of canola spikes should be estimated. Motivated from this point of view, another technique is applied to eliminate these spikes. The idea to calculate the number of canola spikes is to count the number of canola spikes by manual. From these manual counting number of canola spikes, an average percentage of spikes is calculated. Since the results of automatic counting canola seedpods including spikes, the estimated spikes are identified, and the number of seedpods can be calculated. This algorithm is described in Figure 3-10.

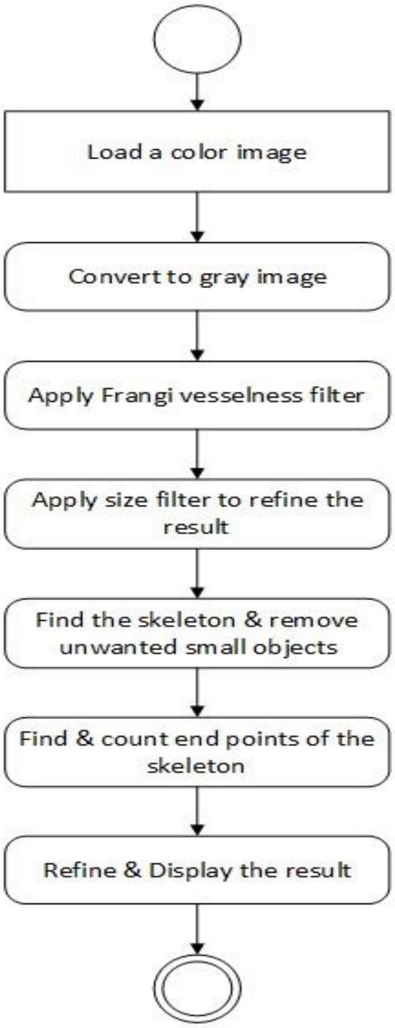

Figure 3-10. The proposed algorithm for detecting and counting canola seedpods

3.3.7 Measuring Plant Height

To measure the height of individual canola plants, each canola plant is placed underneath the proposed camera system in the laboratory, then depth images of the canola are captured and processed. The workflow of the plant-height measurement process, including two different parts, acquiring data and processing image is described in Figure 3-11.

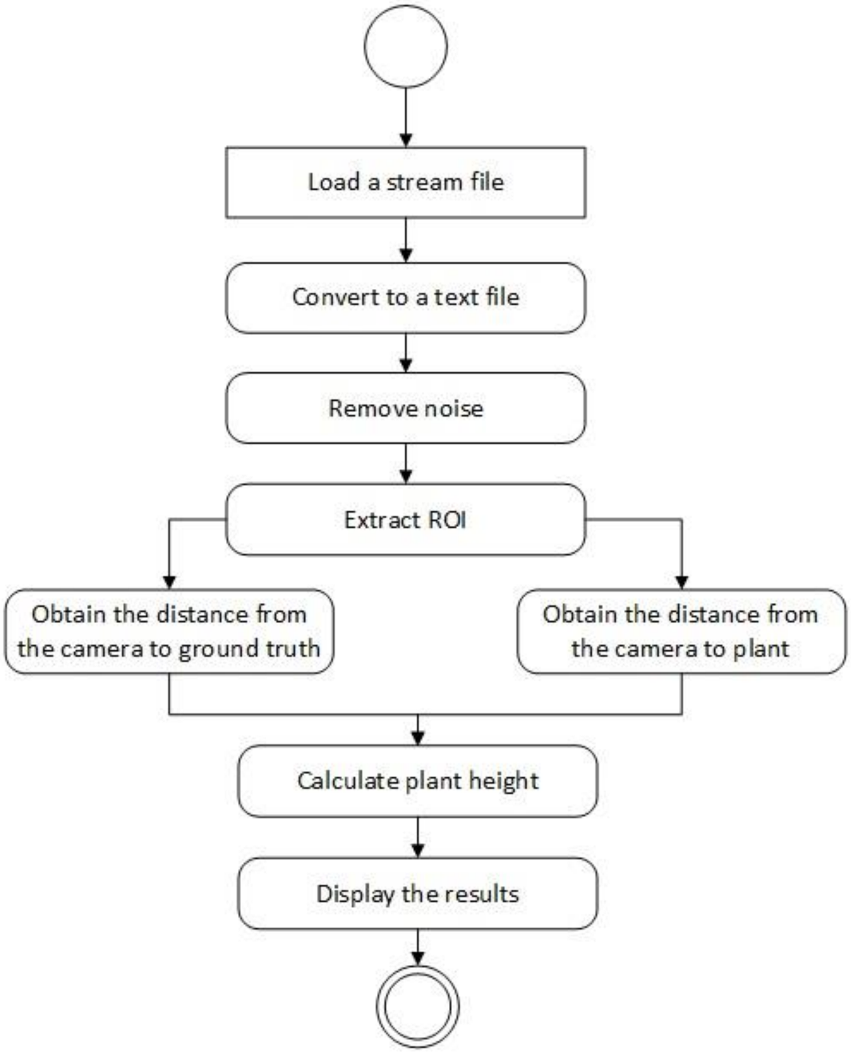

Figure 3-11. The proposed algorithm for plant height measurement

In the acquiring data process, the depth data are captured in term of stream data, then converted to a text file in the Raspberry Pi3. In the imaging process, the text file from the previous process is extracted from multiple MAT files, then extracted the area of interest (ROI) contained the plant. From ROI, the ground point and maximum point values are obtained, and the plant height is directly calculated as

$$plant\ height\ (mm) = ground_{point}(mm) - maximum_{point}(mm) \qquad (3.24)$$

where $ground_{point}$ is the distance from the depth camera to the ground and $maximum_{point}$ is the distance from the depth camera to the highest point of the plant. These distance values are extracted directly from the depth images. The color image, depth image and depth image histogram of the canola plant are depicted in Figure 3-12.

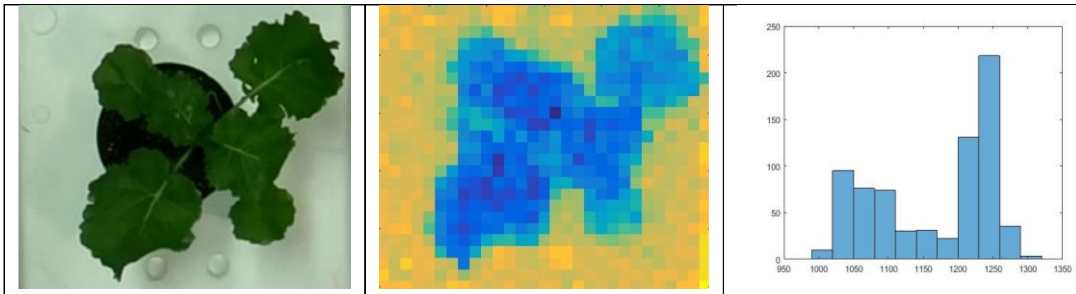

(a) Color image

(b) Depth image

(c) the histogram of the depth image

Figure 3-12. An example of the canola plant-height measurement.

3.3.8 Multi-focus Image Fusion

In the proposed fusion approach, three IQA metrics: visual saliency similarity, gradient similarity, and chrominance similarity (or color distortion) are measured to obtain their weight maps. Then these weight maps are refined by a gradient domain fast guided filter in which, a gradient domain guided filter proposed by [92] and fast guided filter proposed by [93] are combined. The workflow of the proposed multi-focus image fusion algorithm is illustrated in Figure 3-13. The detail of the proposed algorithm is described as follow.

First, each input image is decomposed into a base and detail components, which contain the large-scale variations in intensity and the small-scale variations in intensity, respectively. A Gaussian filtered is used for each source image to obtain its base component, and the detail component can be easily obtained by subtracting the base component from the input image, as given by:

$$B_n = I_n * G_{r,\sigma} \tag{3-25}$$

$$D_n = I_n - B_n \tag{3-26}$$

where B_n and $D_n$are the base and detail components of the n^{th} input image, respectively. $*$ denotes a convolution operator, and $G_{r,\sigma}$ is a 2-D Gaussian smoothing filter.

Then, several measures are used to obtain weight maps for image fusing. According to [91], visual saliency similarity, gradient similarity, and chrominance maps are vital metrics in accounting for the visual quality of image fusion techniques. In most cases, changes of visual saliency (VS) map can be a good indicator of distortion degrees and thus, VS map is used as a local weight map. However, VS map does not work quite well for the distortion type of contrast change. Fortunately, the image gradient can be used as an additional feature to compensate for the lack of contrast sensitivity of the VS map. In addition, VS map does not work quite well for the distortion type change of color saturation. This color distortion cannot be well represented by gradient either since usually gradient is computed from the luminance channel of images. To deal with this color distortion, two chrominance channels are used as features to represent the quality degradation caused by color distortion. Motivated from these metrics, an image fusion method is designed based on the measurement of three key visual features of input images: visual saliency similarity, gradient similarity, and chrominance similarity.

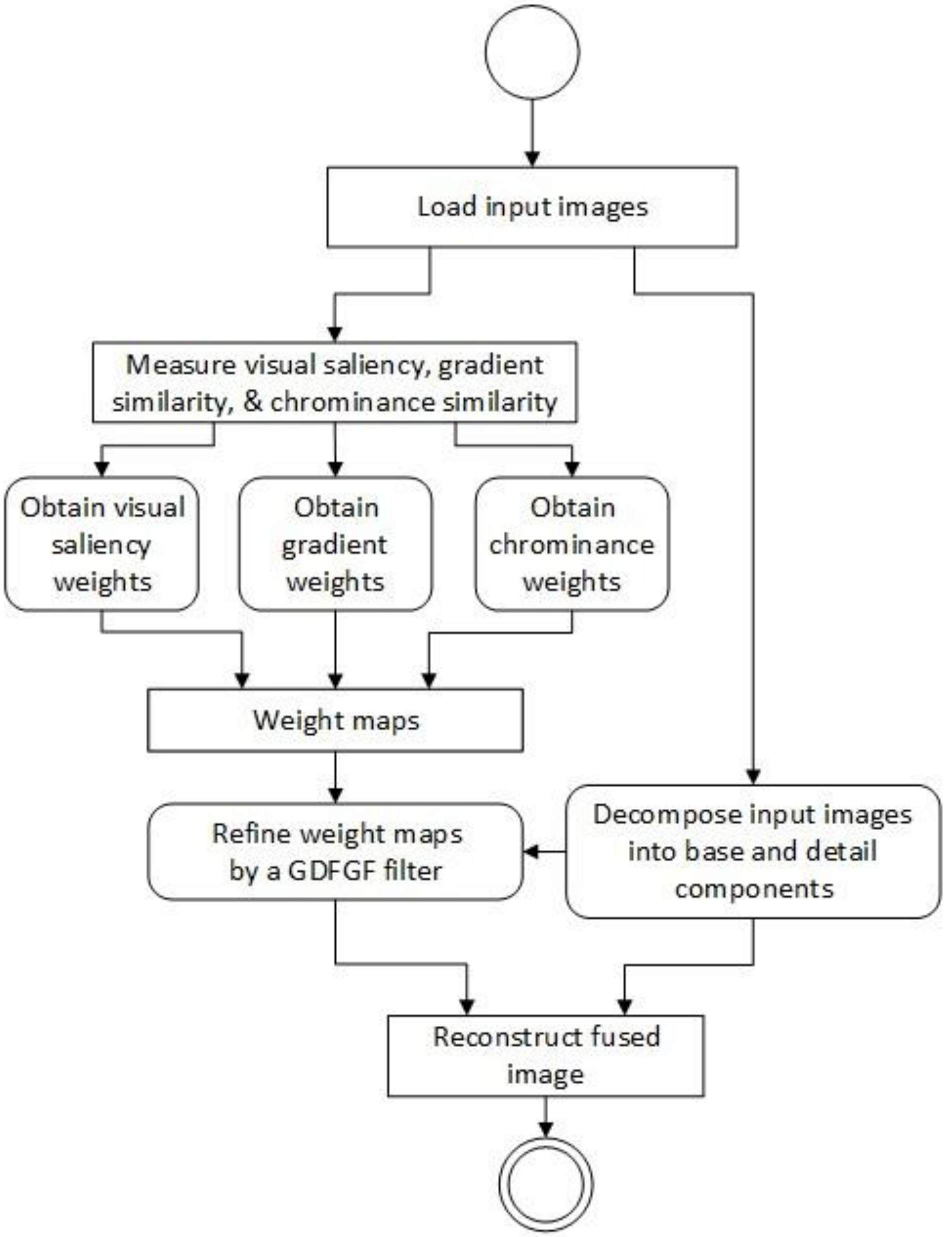

Figure 3-13. The workflow of the proposed algorithm for multi-focus image fusion

a. Visual Saliency Similarity Maps

A saliency similarity detection algorithm proposed by [101] is adopted to calculate visual saliency similarity in this thesis due to its higher accuracy and low computational complexity comparing with other current algorithms. This algorithm is constructed by combining three simple priors: frequency, color, and location. The visual saliency similarity maps are calculated as

$$VS_n^k = SF_n^k . SC_n^k . SD_n^k \tag{3-27}$$

where SF_n^k, SC_n^k, SD_n^k are the saliency at pixel k under frequency, color and location priors. SF_n^k is calculated by

$$SF_n^k = (IL_n^k * g)^2 + (Ia_n^k * g)^2 + (Ib_n^k * g)^2)^{1/2} \tag{3-28}$$

where IL_n^k, Ia_n^k, Ib_n^k are three resulting channels transformed from the given RGB input image, I_n to CIE L*a*b* space. CIE L*a*b* (CIELAB) is a color space specified by the Commission internationale de l'éclairage (CIE). This color space describes all the colors visible to the human eye and is an opponent color system that L* channel indicates lightness, a* channel represents green-red information while b* channel represents blue-yellow information. If a pixel has a smaller (greater) a* value, it would seem greenish (reddish). If a pixel has a smaller (greater) b* value, it would seem blueish (yellowish). Then, if a pixel has a higher a* or b* value, it would seem warmer; otherwise, colder. The color saliency SC_n at pixel k is calculated using

$$SC_n^k = 1 - \exp(-\frac{(Ia_n^k)^2 + (Ib_n^k)^2}{\sigma_C^2}) \tag{3-29}$$

where σ_C is a parameter. $(Ia_n^k) = \frac{Ia_n^k \ -\mathrm{mina}}{maxa-mina}$, $(Ib_n^k = \frac{(Ib_n^k - \mathrm{minb}}{maxb-minb}$, $mina(maxa)$ is the minimum (maximum) value of the Ia and minb (maxb) is the minimum (maximum) value of the Ib.

Many studies found that regions near the image center are more attractive to human visual perception [101]. It can thus be suggested that regions near the center of the image will be more likely to be "salient" than the ones far away from the center. The location saliency at pixel k under the location prior can be formulated by

$$SD_n^k = \exp(-\frac{\|k-c\|^2}{\sigma_D^2}) \tag{3-30}$$

where σ_D is a parameter. c is the center of the input image I_n. Then, the visual saliency was used to construct the visual saliency (VS) maps, given by

$$VSm = VS * G_{r,\sigma} \tag{3-31}$$

where $G_{r,\sigma}$ is a Gaussian filter.

b. *Gradient Magnitude Similarity*

The gradient is usually computed by convolving an image with a linear filter. The gradient magnitude similarity algorithm proposed by [102] is adopted. This algorithm used Scharr gradient operator, which has been proved very powerful in their previous study. With the Scharr gradient operator, the partial derivatives GMx_n^k and GMy_n^k of an input image I_n are calculated as:

$$GMx_n^k = \frac{1}{16}\begin{bmatrix} 3 & 0 & -3 \\ 10 & 0 & -10 \\ 3 & 0 & -3 \end{bmatrix} * I_n^k$$

$$GMy_n^k = \frac{1}{16}\begin{bmatrix} 3 & 0 & -3 \\ 10 & 0 & -10 \\ 3 & 0 & -3 \end{bmatrix} * I_n^k \tag{3-32}$$

The gradient of the image I_n is calculated by

$$GM_n = \sqrt{GMx^2 + GMy^2} \tag{3-33}$$

The gradient is computed from the luminance channel of input images that will be introduced in the next section. Similar to the visual saliency maps, the gradient magnitude (GM) maps is constructed as

$$GMm = GM * G_{r,\sigma} \tag{3-34}$$

c. *Chrominance Similarity*

The RGB input images are transformed into an opponent color space [102], given by

$$\begin{bmatrix} L \\ M \\ N \end{bmatrix} = \begin{bmatrix} 0.06 & 0.63 & 0.27 \\ 0.30 & 0.04 & -0.35 \\ 0.34 & -0.6 & 0.17 \end{bmatrix} \begin{bmatrix} R \\ G \\ B \end{bmatrix} \tag{3-35}$$

The L channel is used to compute the gradients introduced in the previous section. The M and N (chrominance) channels are used to calculate the color distortion saliency, given by

$$M_n = 0.30 * R + 0.04 * G - 0.35 * B \tag{3-36}$$

$$N_n = 0.34 * R - 0.6 * G + 0.17 * B \tag{3-37}$$

$$C_n = M_n . N_n \tag{3-38}$$

Finally, the chrominance similarity or color distortion saliency (CD) maps is calculated by

$$CDm = C * G_{r,\sigma} \tag{3-39}$$

d. *Weight Maps*

Using three measured metrics above, the weight maps are computed as given by

$$W_n = (VSm)^{\alpha}.(GMm)^{\beta}.(CDm)^{ɤ} \tag{3-40}$$

where α, β, and ɤ are parameters used to control the relative importance of visual saliency (VS), gradient saliency (GM), and color distortion saliency (CD). From these weight maps, W at each location k, the overall weight maps of each input image can be obtained.

$$W_n^k = \begin{cases} 1, if \;\; W_n^k = \max(W_1^k, W_2^k, \dots, W_N^k), \\ 0, \qquad\qquad\qquad\qquad otherwise, \end{cases} \tag{3-41}$$

where *N* is number of input images, W_n^k is the weight value of the pixel k in the n^{th} image. Then proposed weight maps are determined by normalizing the saliency maps as follows:

$$W_n^k = \frac{W_n^k}{\sum_{n=1}^{N} W_n^k}, \qquad \forall n = 1, 2, \dots, N \tag{3-42}$$

These weight maps then are refined by a gradient domain guided filter that introduced in the next section.

e. Gradient Domain Fast Guided Filter

The gradient domain guided filter that proposed by [92] is adopted to optimize the initial weight maps. By using this filter, the halo artifacts can be more effectively suppressed the other traditional or guided filter algorithms. It also less sensitive to its parameters while has the same complexity as the guided filter. The gradient domain guided filter has good edge-preserving smoothing properties like the bilateral filter, but it does not suffer from the gradient reversal artifacts. The filtering output is a local linear model of the guidance image [92]. According to the authors, the gradient domain guided filter performs very well in many applications, including image smoothing or enhancement. It is one of the fastest edge-preserving filters. Therefore, the gradient domain guided filter can apply in image smoothing to avoid ringing artifacts. The gradient domain guided filter can be summarized as bellow.

It is assumed that the filtering output Q is a linear transform of the guidance image G in a local window w_k centered at the pixel k.

$$Q_i = a_k G_i + b_k, \forall i \in w_k \tag{3-43}$$

where (a_k, b_k) are some linear coefficients assumed to be constant in the local window $w_k$with the size of (2 ζ1+1)×(2 ζ1+1). The linear coefficients (a_k, b_k) can be estimated by minimizing the cost function in the window w_k between the output image Q and the input image P

$$E_{(a_k,b_k)} = \sum_{i \in w_k} [(Q_i - P_i)^2 + \frac{\lambda}{\hat{\Gamma}_{G(k)}} (a_k - \gamma_k)^2] \tag{3-44}$$

where γ_k is defined as

$$\gamma_k = 1 - \frac{1}{1+e^{\eta(\chi(k)) - \mu_{\chi,\infty}}} \tag{3-45}$$

$\mu_{\chi,\infty}$ is the mean value of all $\chi(k)$. η is calculated as $4/(\mu_{\chi,\infty} - \min(\chi(k)))$. $\hat{\Gamma}_G(k)$ is a new edge-aware weighting used to measure the importance of pixel k with respect to the whole guidance image. It is defined by using local variance of 3x3 windows and $(2\zeta 1 + 1)\ x\ (2\zeta 1 + 1)$ windows of all pixels by

$$\hat{\Gamma}_G(k) = \frac{1}{N}\sum_{i=1}^{N} \frac{\chi(k)+\varepsilon}{\chi(i)+\varepsilon} \tag{3-46}$$

where $\chi(k) = \sigma_{G,1}(k)\sigma_{G,\zeta 1}(k)$. ζ_1 is the window size of the filter.

The optimal values of a_k and b_k are computed by

$$a_k = \frac{\mu_{G\odot X,\zeta 1}(k) - \mu_{G,\zeta 1}(k)\mu_{X,\zeta 1}(k) + \frac{\lambda}{\hat{\Gamma}_G(k)}\gamma_k}{\sigma^2_{G,\zeta 1}(k) + \frac{\lambda}{\hat{\Gamma}_G(k)}} \tag{3-47}$$

$$b_k = \mu_{X,\zeta 1}(k) - a_k\ \mu_{G,\zeta 1}(k) \tag{3-48}$$

The final value of $\widehat{Q_\iota}$ is calculated by

$$\widehat{Q_\iota} = \bar{a}_k G_i + \bar{b}_k \tag{3-49}$$

where $\bar{a}_k$ and $\bar{b}_k$ are the mean values of $a_k$and b_k in the window, respectively. $\bar{a}_k$ and $\bar{b}_k$ are computed by

$$\bar{a}_k = \frac{1}{|w_{\zeta 1}(k)|}\sum_{i\in w_{\zeta 1}(k)} a_k \tag{3-50}$$

$$\bar{b}_k = \frac{1}{|w_{\zeta 1}(k)|}\sum_{i\in w_{\zeta 1}(k)} b_k \tag{3-51}$$

where $|w_{\zeta 1}(k)|$ is the cardinality of $w_{\zeta 1}(k)$.

f. Refining weight maps by the gradient domain guided filter

Due to these weight maps are noisy and not aligned with object boundaries. The proposed approach deploys a gradient domain guided filter to refine the weight maps. The gradient domain guided filter is used at each weight map W_n with the corresponding input image I_n. However, the weigh map W_D_n used W_B_n as the guidance image to improve the W_D_n, is calculated by

$$W\_B_n = G_{r1,\mathcal{E}1}(W_n, I_n) \tag{3-52}$$

$$W\_D_n = G_{r2,\mathcal{E}2}(W\_B_n, I_n) \tag{3-53}$$

where $r1,\ \mathcal{E}1\ and\ r2,\ \mathcal{E}2$ are the parameters of the guided filter. W_B_n and W_D_n are the refined weight maps of the base and detail layers, respectively. Both weight maps W_B_n and W_D_n are deployed mathematical morphology techniques to remove small holes and unwanted regions in the focus and defocus regions. The morphology techniques are described as bellow,

$$\begin{aligned} mask \ &= W_n < threshold \\ temp1 &= imfill(mask,' holes') \\ temp2 &= 1 - temp1 \\ temp3 &= imfill(temp2,' holes') \\ W_n(refined) \ &= bwareaopen(temp3, threshold) \end{aligned} \tag{3-54}$$

Then, the values of the N refined weight maps are normalized such that they sum to one at each pixel k. Finally, the fused base and detail layer images are calculated and blended to fuse the input images, as given by

$$\bar{B}_n = W\_B_n * \ B_n \tag{3-55}$$

$$\overline{D}_n = W\_D_n * \ D_n \tag{3-56}$$

$$Fused_n = \bar{B}_n + \overline{D}_n \tag{3-57}$$

The fast guided filter is improved of the guided filter proposed by [93]. This algorithm is adopted for reducing the processing of gradient domain guided filter time complexity. According to [93], before processing gradient domain guided filter, the rough transmission map and the guidance image employ nearest neighbor interpolation down-sampling. After gradient domain guided filter processing, the gradient domain guided filter output image uses bilinear interpolation for up-sampling and obtains the refining transmission map. Using this fast guided filter, the gradient domain guided filter performs better than the original one. Therefore, the proposed filter was named as the gradient domain fast guided filter.

CHAPTER 4 - A LOW-COST DEPTH MOBILE PLATFORM

This section describes the proposed platform and its components for the thesis as follows: the proposed system design (Section 4.1); an Argos3D P100 camera and its specifications (Section 4.2); A Kinect V2 and its specifications (Section 4.3); a digital camera and its specifications (Section 4.4); a Pi camera and its specifications (Section 4.5); a Raspberry Pi3 and its specifications (Section 4.6); a wireless remote control system and its specifications (Section 4.7); DC to DC converters and their specifications (Section 4.8); a power supply and its specifications (Section 4.9); a set of tools used for developing software of the proposed platform (Section 4.10); developed software of the proposed platform (Section 4.11).

4.1 Phenotyping Mobile Platform

From the concept design mentioned in the previous section, a low-cost high throughput phenotyping mobile system has been developed as illustrated in Figure 4-1. This system includes an Argos3D-P100 camera, a Pi camera, a Raspberry Pi3, two DC converters (one for Raspberry Pi3 and other for the Argos3D P100), a 12V battery, and a remote control. Canola plants were used in our experiments. In addition, a Kinect V2 camera and a Sony A58 camera were also used to compare the performance of detection and counting branches and seedpods with this system (see Figure 4-2).

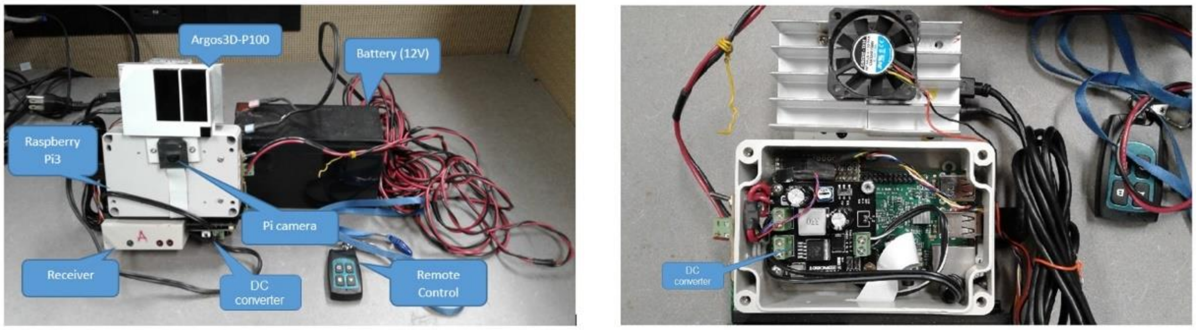

a) Front side

b) Back side

Figure 4-1. The proposed low-cost depth mobile phenotyping system


Kinect V2
Sony A58

Figure 4-2. Kinect V2 and Sony A58 cameras

4.2 Argos3D-P100

The Argos3D - P100 is a depth sensor, operating on the Time-of-Flight (ToF) principle, developed by Bluetechnix (Wien, Austria; www.bluetechnix.at). By equipping a PMD PhotonICs® 19k-S3 Time-of-Flight 3D chip, this sensor is able to capture a resolution of 160 x 120 pixels and up to 160 fps. This smart sensor simultaneously delivers depth information and intensity level for each pixel. This sensor adds up to 19,200 independent measuring points of each measuring cycle. Therefore, it is possible to analyze scenes based on only 3D data or in combination with grayscale information.

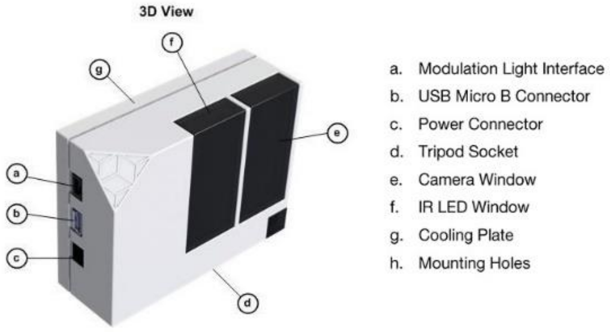

Figure 4-3. An Argos3D – P100

The Argos3D – P100 includes four main components: depth sensor, lens, active infrared light (IR) illumination and a Central Processing Unit (CPU) as illustrated in Figure 4-4. The active illumination module determines modulated IR in the near-infrared. The object is projected via the lens onto the depth sensor. Taking the angular phase shift into consideration, the distance data between the depth sensor and the object of each pixel will be individually calculated. As a result, a 3D point cloud and intensity data per pixel or depth and intensity level are produced at the same time.

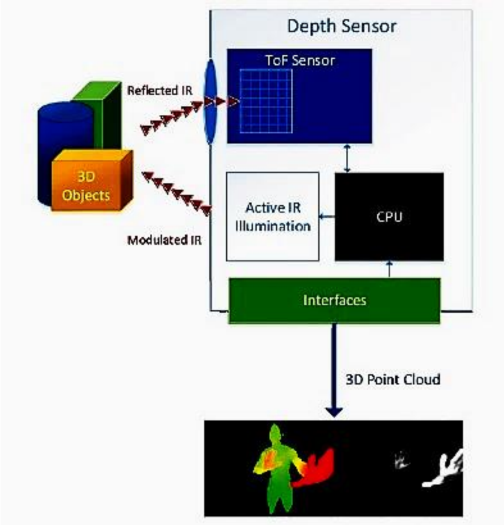

Figure 4-4. Structure of the Argos3D P100 sensor (www.bluetechnix.at)

With a power supply of 5V@2.6A, an operation range of 3m, a field of view of 90 x 67.5 degrees, supported Windows and Linux OS, and a size of 75 x 57 x 26 mm, this depth camera can be suitable for a mobile phenotyping system as listed in Table 4-1.

Table 4-1. Argos3D –P100 specifications (Taken from www.bluetechnix.at)

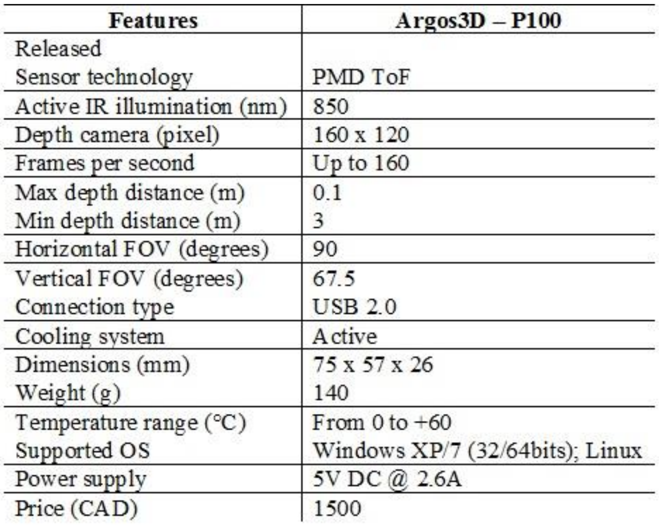

Features	Argos3D – P100
Released	
Sensor technology	PMD ToF
Active IR illumination (nm)	850
Depth camera (pixel)	160 x 120
Frames per second	Up to 160
Max depth distance (m)	0.1
Min depth distance (m)	3
Horizontal FOV (degrees)	90
Vertical FOV (degrees)	67.5
Connection type	USB 2.0
Cooling system	Active
Dimensions (mm)	75 x 57 x 26
Weight (g)	140
Temperature range (°C)	From 0 to +60
Supported OS	Windows XP/7 (32/64bits); Linux
Power supply	5V DC @ 2.6A
Price (CAD)	1500

Examples of a 3D image (point cloud) and grayscale information (Distance and Amplitude information) captured by the Argos3D P100 during in experiments are shown in Figure 4-5.

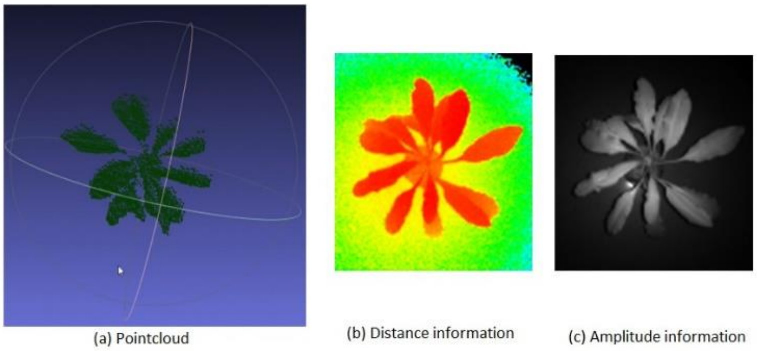
(a) Pointcloud (b) Distance information (c) Amplitude information

Figure 4-5. An example of 3D and 2D images

4.3 Kinect V2

Kinect v2 is an RGB-D acquisition device designed by Microsoft as a contact-free controller for Xbox One. The Kinect sensor consists of an infrared projector, an infrared camera, and an RGB camera (see Figure 4-6). The RGB and IR cameras are equipped with a 400-800nm bandpass filter and 850–1100nm bandpass filter, respectively.

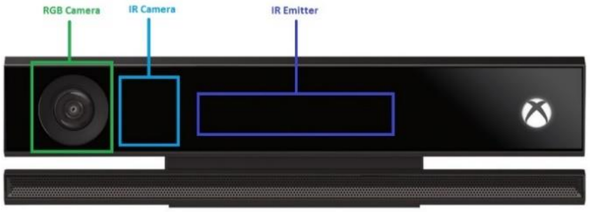

Figure 4-6. Kinect V2 Sensor

The Kinect sensor simultaneously acquires depth and color information at a frame rate of up to 30 fps. The integration of depth and color data results in a colored point cloud that contains about 300,000 points in every frame. It captures a depth image with 512 x 424 pixels at a measurement rate of 30 fps. Since an infrared laser beam is divided into multiple beams onto the scene, the infrared camera records this pattern. The measurable distance range from 500 mm to maximum 4500 mm. Figure 4-7 displays some 3D image and 2D images captured from the Kinect V2 sensor.

Table 4-2. Kinect V2 specifications

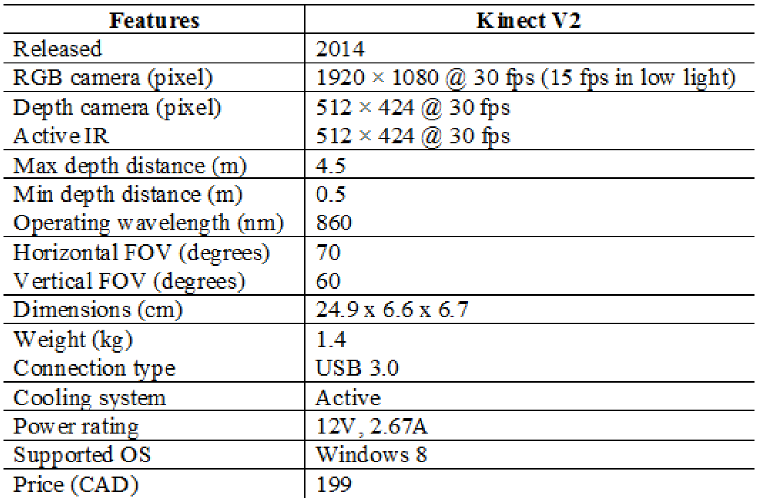

Features	Kinect V2
Released	2014
RGB camera (pixel)	1920 × 1080 @ 30 fps (15 fps in low light)
Depth camera (pixel)	512 × 424 @ 30 fps
Active IR	512 × 424 @ 30 fps
Max depth distance (m)	4.5
Min depth distance (m)	0.5
Operating wavelength (nm)	860
Horizontal FOV (degrees)	70
Vertical FOV (degrees)	60
Dimensions (cm)	24.9 x 6.6 x 6.7
Weight (kg)	1.4
Connection type	USB 3.0
Cooling system	Active
Power rating	12V, 2.67A
Supported OS	Windows 8
Price (CAD)	199

a) RGB image b) 3D image c) Depth image d) Infrared image

Figure 4-7. Examples of 3D image and 2D images taken by the Kinect V2 sensor

4.4 Digital Camera

Sony A58 camera is selected due to its low price and high-quality image. The basic price is about CAD $500. This camera offers a high resolution of 20.1 effective megapixels. It is equipped with a redesigned DT 18-55mm F3.5-5.6 SAM II kit lens that offers quieter autofocus. It also provides remote control function that very useful for capturing without any direct touch to the camera.

Figure 4-8. Sony A58

Table 4-3. Sony A58 key specifications

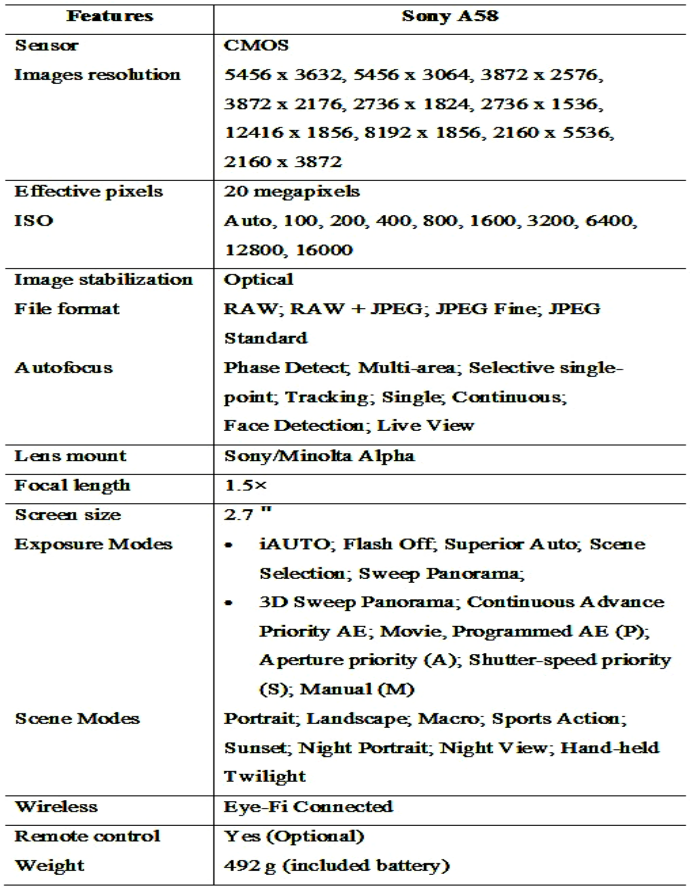

Features	Sony A58
Sensor	CMOS
Images resolution	5456 x 3632, 5456 x 3064, 3872 x 2576, 3872 x 2176, 2736 x 1824, 2736 x 1536, 12416 x 1856, 8192 x 1856, 2160 x 5536, 2160 x 3872
Effective pixels	20 megapixels
ISO	Auto, 100, 200, 400, 800, 1600, 3200, 6400, 12800, 16000
Image stabilization	Optical
File format	RAW; RAW + JPEG; JPEG Fine; JPEG Standard
Autofocus	Phase Detect; Multi-area; Selective single-point; Tracking; Single; Continuous; Face Detection; Live View
Lens mount	Sony/Minolta Alpha
Focal length	1.5×
Screen size	2.7 "
Exposure Modes	• iAUTO; Flash Off; Superior Auto; Scene Selection; Sweep Panorama; • 3D Sweep Panorama; Continuous Advance Priority AE; Movie, Programmed AE (P); Aperture priority (A); Shutter-speed priority (S); Manual (M)
Scene Modes	Portrait; Landscape; Macro; Sports Action; Sunset; Night Portrait; Night View; Hand-held Twilight
Wireless	Eye-Fi Connected
Remote control	Yes (Optional)
Weight	492 g (included battery)

4.5 Pi Camera

The Pi camera module with adjustable-focus shown in Figure 4-9 was used. The board of Pi camera is tiny, at around 25mm x 23mm x 9mm and it weighs just over 18g (including LED lights). It connects to Raspberry Pi by using the dedicated CSi interface. The Pi camera, equips with the 5 megapixels OV5647 sensor. It is able to capture 2592 x 1944 pixel static images, and also supports to capture video of 1080 p at 30 fps, 720 p at 60 fps and 640 x 480 p at 60/90 formats.

Figure 4-9. A Pi camera module with adjustable focus

Table 4-4. Kuman Pi camera module specifications (Taken from https://www.amazon.ca)

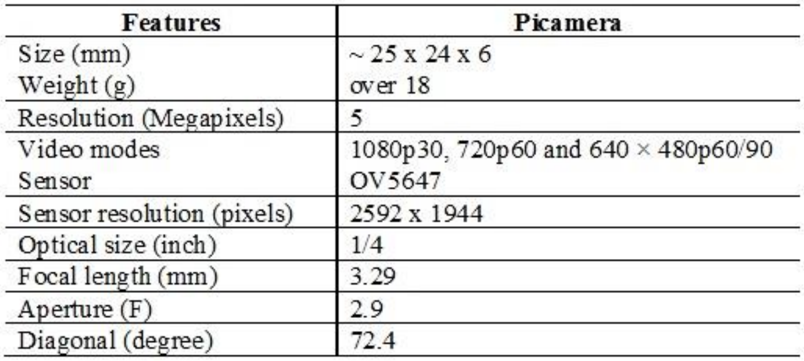

Features	Picamera
Size (mm)	~ 25 x 24 x 6
Weight (g)	over 18
Resolution (Megapixels)	5
Video modes	1080p30, 720p60 and 640 × 480p60/90
Sensor	OV5647
Sensor resolution (pixels)	2592 x 1944
Optical size (inch)	1/4
Focal length (mm)	3.29
Aperture (F)	2.9
Diagonal (degree)	72.4

4.6 Raspberry Pi 3

From the beginning, a series of small single-board computers - Raspberry Pi- was developed by the Raspberry Pi Foundation for educational purposes. The main advantages of Raspberry Pi computers are small and low cost. There are several generations of Raspberry Pi, such as Raspberry Pi 1 with some models (such as B, A, A+, and B+), Pi Zero (smaller size and reduced input/output (I/O), and general-purpose input/output (GPIO) capabilities), that have been released from 2012 to 2015. From 2017, newest models (such as Pi 3 Module B and Pi Zero W) have been equipped Wi-Fi and Bluetooth functionality. In our study, a Raspberry Pi 3 Module B was adopted. The Raspberry Pi 3- Model B equips a quad-core 64-bit ARM Cortex A53 clocked at 1.2 GHz (see Figure 4-10). This makes the Pi 3 roughly 50% faster than the Pi 2. The Pi 3 still uses 1GB of LPDDR2-900 SDRAM and Broadcom VideoCore IV for graphics capabilities, but it includes onboard 802.11n Wi-Fi and Bluetooth 4.0. (https://www.raspberrypi.org).

Figure 4-10. Raspberry Pi 3 - Module B

Table 4-5. Raspberry Pi 3 Module B specifications (Taken from https://www.raspberrypi.org)

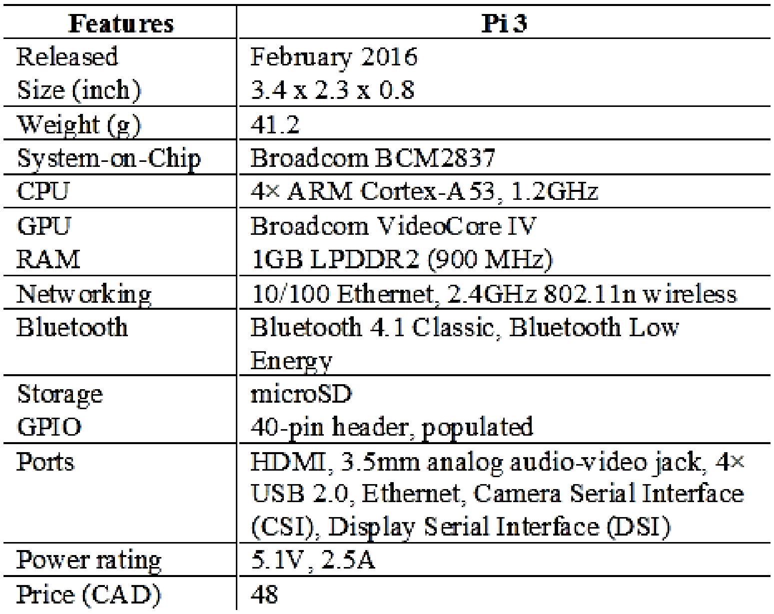

Features	Pi 3
Released	February 2016
Size (inch)	3.4 x 2.3 x 0.8
Weight (g)	41.2
System-on-Chip	Broadcom BCM2837
CPU	4× ARM Cortex-A53, 1.2GHz
GPU	Broadcom VideoCore IV
RAM	1GB LPDDR2 (900 MHz)
Networking	10/100 Ethernet, 2.4GHz 802.11n wireless
Bluetooth	Bluetooth 4.1 Classic, Bluetooth Low Energy
Storage	microSD
GPIO	40-pin header, populated
Ports	HDMI, 3.5mm analog audio-video jack, 4× USB 2.0, Ethernet, Camera Serial Interface (CSI), Display Serial Interface (DSI)
Power rating	5.1V, 2.5A
Price (CAD)	48

4.7 Wireless Remote Control

A wireless remote-control system, as shown in Figure 4-11, INSMA DC 12V 4 channels, 433 MHz with 2 transmitter switch, is used to start and stop capturing images from the Argos3D and Pi cameras. This system can be purchased from the Amazon, about CAD$ 55/piece.

Figure 4-11. A wireless remote control system

The receiver and transmitter have key features as follow: a) Receiver: Operating supply DC 7mA@12V, frequency: 433Mhz, quiescent condition: 6mA, receiver sensitivity: more than -105dBm, output voltage: AC and DC is optional, output current: 3A, size: 72mm (L) x 52mm (W) x 26mm (H). b) Remote control transmitter: Remote distance: 200m, operating voltage: DC 12V, operating current: 13mA, frequency: 433Mhz, code type: Fixed code / Learning code, size: 55mm (L) x 30mm (W) x 10mm (H). The receiver was configured to operate in Self–lock mode, which uses one channel switch and one remote button control. In the Self-lock mode, pressing one button for one time is ON; pressing the same button again is OFF.

4.8 DC to DC Converters

Two small size step-down converters (5A, 350 KHz, 25V, DC to DC) were used for Raspberry Pi3 and Argos3D P100 camera to convert 12V to 5V/5A (see Figure 4-12). These modules were bought from the Robotshop.ca, about CAD $11/piece. These converters have the following features: input voltage range: 3.6V to 25V, output adjustable range: 3.3V to 25V, constant output current: 5A@5V, max output power: 25W, switching frequency: 350KHz, three different output interfaces, size: 46x50x20mm.

Figure 4-12. A DC-DC Step Down Converter

4.9 Power Supply

A 12V, 7.2Ah sealed lead acid rechargeable battery (UPS TLV1272 model) was equipped to supply power for the proposed phenotyping mobile system. This battery is a small size sealed battery with free maintenance, long service life, wide operating temperature range, and high discharge rate. By setting the Argos3D's frame rate to 10 fps, the power consumption has lowered. Because the power of this battery can offer up to 12V*7.2A = 86.4 VAh, it is able to supply the proposed mobile system for at least 86.4 VAh/12V*0.95A = 7.5hr continuous working.

4.10 Tools

4.10.1 Argos3D P100 APIs

To create a common interface for their products, Bluetechnix developed the interfaces between a ToF device and applications as shown in Figure 4-13. The heart of this interface is the BltTofApi, which is written in C for platform independence. The BltTofSuite, including the

BltTofApi interface, is compatible with any device with existing lib implementing the BltTofApi (https://support.bluetechnix.at).

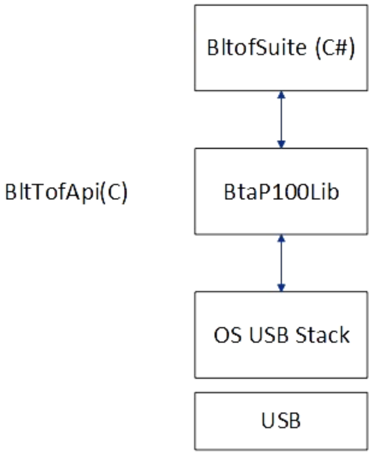

Figure 4-13. Argos3D P100's interfacing concept

The main interfaces of the BltTofApi are listed as in Table 4-6. In this thesis work, a package of BtaP100Lib was used as an interface between the USB camera and a Python-based application running on Raspbian OS to capture depth and intensity data.

Table 4-6. Argos3D P100 BltTofApi interfaces (Taken from www.bluetechnix.com)

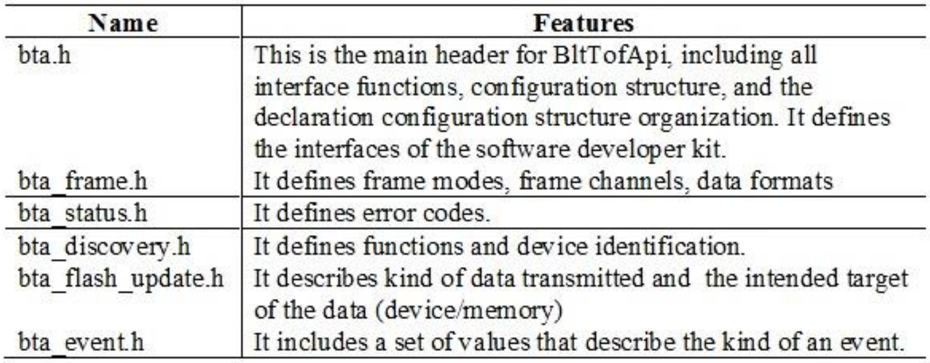

Name	Features
bta.h	This is the main header for BltTofApi, including all interface functions, configuration structure, and the declaration configuration structure organization. It defines the interfaces of the software developer kit.
bta_frame.h	It defines frame modes, frame channels, data formats
bta_status.h	It defines error codes.
bta_discovery.h	It defines functions and device identification.
bta_flash_update.h	It describes kind of data transmitted and the intended target of the data (device/memory)
bta_event.h	It includes a set of values that describe the kind of an event.

4.10.2 Raspbian Operating System

The Raspberry Pi operating system used in this study is the Raspbian Jessie 4.1. It is the Raspberry Pi Foundation's official supported operating system available for free to download and use. Based on the Debian computer operating system, Raspbian is highly optimized to work efficiently with Raspberry Pi computers. Raspbian has plenty of pre-installed software for education, programming, and general purposes. While Debian is very lightweight and makes a great choice for the Pi computers, Raspbian consists of tools for browsing, python programming, and a GUI desktop.

4.10.3 Python

Python is a powerful high-level and object-oriented programming language created by Guido van Rossum, released in 1991. Due to its easy-to-use syntax, Python allows programmers to read and write concepts much easier than other languages such as C++, Java, and C#. Python can run on almost all platforms including Windows, Mac OS X, and Linux. It also can easily combine with other languages (C/C++ or other languages). When compiling Python code, it automatically converts the code to the machine language that it does not need to concern about memory management. Furthermore, Python is equipped a number of standard libraries that make programmers much more comfortable since they do not have to write all the code (https://www.python.org). In this study, through Integrated Development Environment or Integrated Development and Learning Environment (IDLE) – an integrated development environment for Python - from the Desktop of the Raspbian operating system, Python 3 was used to code applications of connecting Arogos3D P100 and Pi camera to Raspberry Pi 3, image acquisition, and remote control of start and stop capturing images.

4.10.4 Matlab 2016b

Matlab 2016b was used to develop applications for extracting Argos3D-P100's streams and Pi's videos, detection and counting number of canola branches and seedpods, measuring the height of canola plots, and estimating canola density.

4.10.5 C++ Language

IPC socket server and acquiring streams from the Argos3D camera in term of 3D point cloud and intensity level or depth and intensity level were developed in C++ to use BltTofApi library for the Argso3D camera. In addition, extracting encoded stream files into text files was written in C++.

4.11 Developed Software

A client-server model was developed to concurrent capture images from depth and Pi cameras via remote control. In this model, Inter-Process Communication (IPC) socket client and server were developed to connect between independent processes running on the Raspberry Pi 3. Due to this IPC sockets, start or stop capturing data from both a Pi camera and an Argos3D camera is initiated via a remote control. A general concept view of the data acquisition process is given as in Figure 4-14.

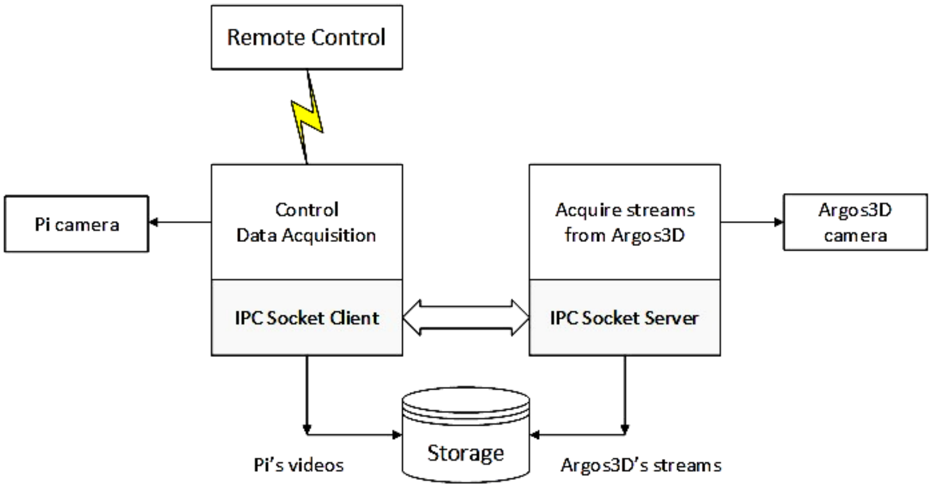

Figure 4-14. Data acquisition process

4.11.1 Control Data Acquisition

Control Data Acquisition manages two processes of capturing images from the Pi camera and the Argos3D camera via a remote control. This module consists of some functions, such as controlling image acquisition from the Pi camera and Argos3D camera, remote control, and inter-process communication between the module of Control Data Acquisition and the module of acquire streams from the Argos3D camera. In this module, Pi camera, GPIO pins for remote control status, and IPC socket client and server were declared and configured.

When the button on the remote control is pressed (flashing red LED for each camera), a “START” command is sent to the Control Data Acquisition module via a wireless protocol, in which, the Argos3D and Pi cameras simultaneously start to record stream and video. When pressing the second time (turn off red LEDs), a “STOP” command is sent to the Control Data Acquisition module, all stream and video are stopped and then stored into the SD card. The stream (e.g., 3D point cloud and intensity level or depth and intensity level) acquired from the Argos3D – P100 is stored into the bltstream format encoded by Bluetechnix. The video obtained from the Pi camera is stored in the h.264 format. The delay time for starting or stopping record stream cycle is about one second because of the integration time of the Argos3D camera. This module can be set up the timeout to automatically shut down the system for a long time unused.

4.11.2 IPC Socket Client and Server

IPC socket Client and Server provide point-to-point, two-way communication between two processes. In this study, IPC socket Client and Server are used to communicate between two modules, Control Data Acquisition and Acquire Streams from the Argos3D, which are written in different languages. While IPC socket client integrated into the Control Data Acquisition module and written in Python, IPC socket server is combined into the module of Acquire streams from the Argos3D using C++ based BltTofApi library.

In operating, the Client and Server processes are started when turning on the Raspberry Pi 3. Then, the Client process is automatically connected to the Server process. On the Server side, the Server process goes to sleep waiting for a request from the Client process. When the Client process sends a request (i.e., start or stop command) across the network to the Server, the Server process receives a message and executes some actions (start or stop capturing data). After finishing its service, the Server goes back to sleep, waiting for the next request from the Client. The diagram of IPC socket Client and Server interaction is shown in Figure 4-15.

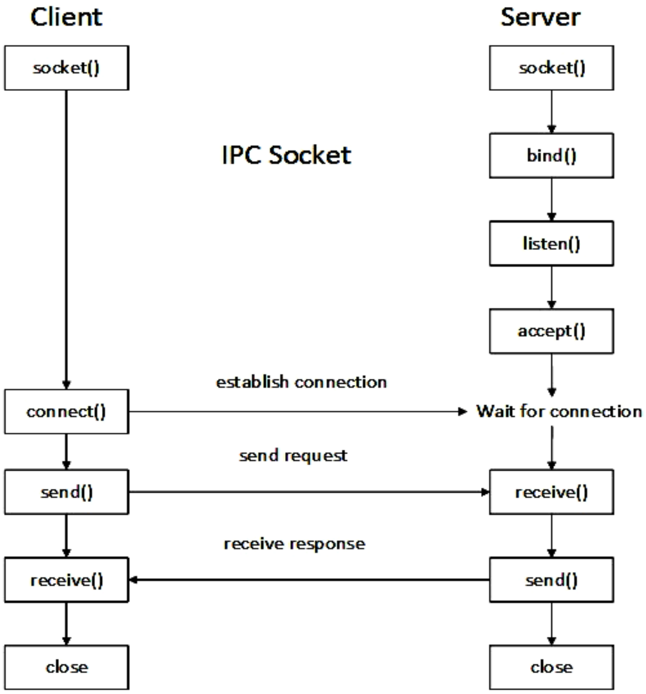

Figure 4-15. The complete IPC socket Client and Server interaction

4.11.3 Acquiring Streams from the Argos3D Camera

The module of Acquiring Streams from the Argos3D was deployed to manage image acquisition from the Argos3D camera as well as communicate with the module of Control Data Acquisition. This hybrid module is written in C++, in which IPC socket Server and Acquiring streams from the Argos3D modules are combined. When the Control Data Acquisition receives a message from the remote control, it concurrently allows the Pi and Argos3D cameras execute an action (start or stop capturing data). In this case, the module of Control Data Acquisition works as an IPC socket Client, while the module Acquiring Streams from the Argos3D works as an IPC socket Server. Therefore, a command (START or STOP) from the remote control is transferred to the Argos3D camera via IPC sockets to start or stop acquiring images. This process can be repeated forever with the minimum interval time between the start and stop signals about 2 seconds. The workflow of acquiring streams from the Argos3D is given in Figure 4-16.

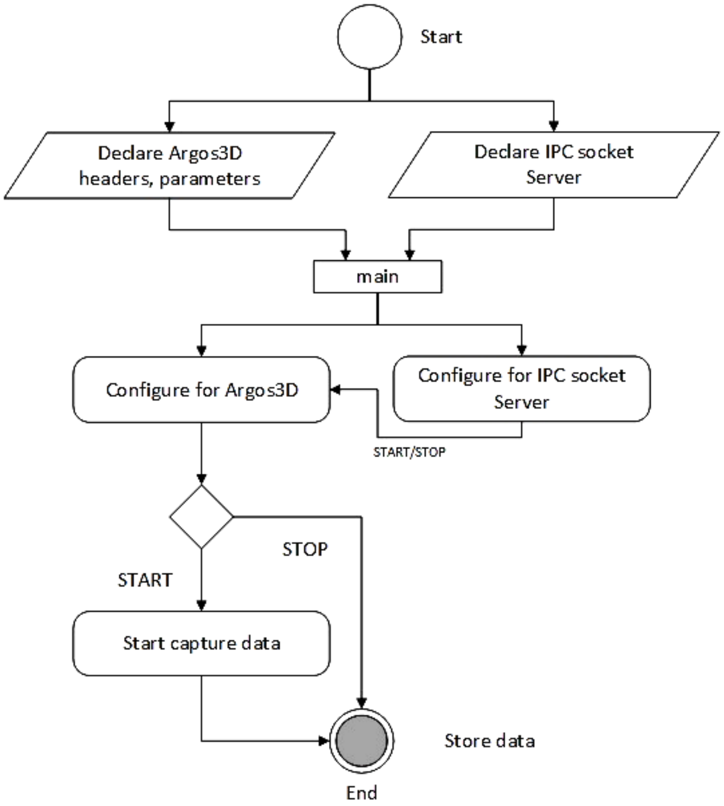

Figure 4-16. The workflow of acquiring streams from the Argos3D

In operation, this module works as an IPC socket Server, waiting for a request from the Client, then executes that request, after that goes to sleep waiting for next request. When the Server process receives a message from the Client process, the Server process will transfer that message to the module of Acquiring streams. Based on the received message, the module of Acquiring streams will start or stop capturing data from the Argos3D camera. For example, when the Server process obtains a message of "START," that message will be sent to the module of Acquiring streams, in which the depth camera already initiated and immediately starts capturing data. If the Client process send a message of "STOP," the capturing stream process will be stopped instantly, and the data will be stored in a bltstream-based file. The bltstream file is only one of two kinds of data, 3D point cloud and intensity level or depth information and intensity level. This kind of data format is able to declare in the configuration of the Argos3D camera.

4.11.4 Acquiring Video from Pi Camera

The function acquiring video from Pi camera was embedded into to module of Control Data Acquisition and written in Python. By using pure Python library existing in the Raspbian OS, acquiring video from Pi camera is very simple. For example, to start or stop recording a video, calls a function start_recording() or stop_recording(), respectively. In the module of Control Data Acquisition, GPIO pins are declared and set to the Broadcom SOC channel (BCM) mode, in which, remote input and Pi camera's LED are set to pin number 17 and 27, respectively. The frame rate of Pi camera is set to 10 fps, the resolution is set to 1640 x 1232 pixels, and the video format is set to h.264 to minimize the video size.

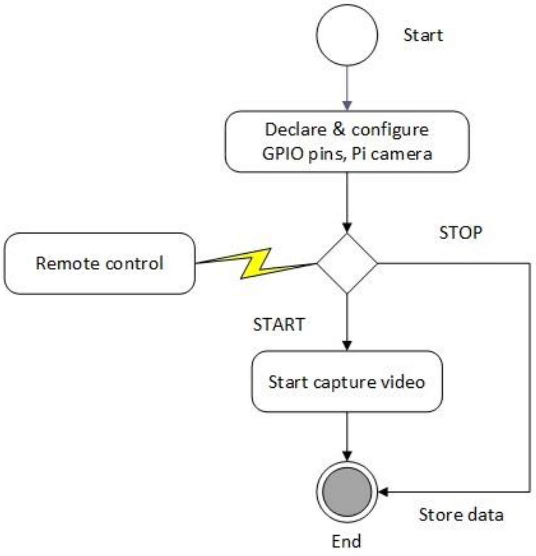

Figure 4-17. The workflow of acquiring videos from the Pi camera

When this module receives a message from the Remote Control, for example, “START” message, the Pi camera immediately starts recording video. It will stop recording and store video when receives “STOP” message. The workflow of the Pi camera’s acquiring videos is demonstrated in Figure 4-17.

4.11.5 Extracting Argos3D’s Stream Files

The module of extracting the Argos3D stream was developed to convert stream files based on bltstream format encoded by Bluetechnix to text-based files. This module is written in C++ due to extracting process depends on BltTofApi library and live Argos3D camera.

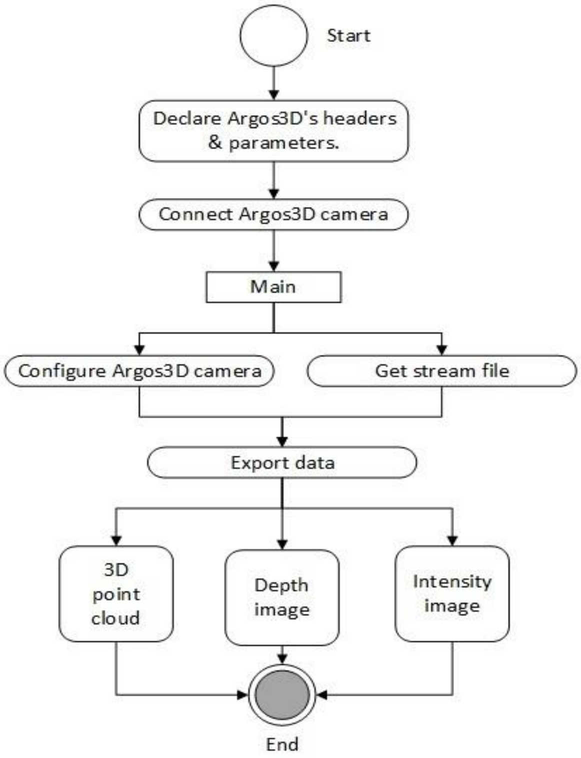

Figure 4-18. The workflow of extracting the Argos3D stream into text files

The process of extracting data from the bltstream files is implemented as a reverting of the capturing data process from Argos3D camera. First, the Argos3D camera’s headers and parameters are declared, and the depth camera is connected. Then, the depth camera is configured, and a target stream file is pulled out. By using functions of BTAgetXYZcoordinates and BTAgetAmplitudes or BTAgetDistances and BTAgetAmplitudes linking to the BltTofApi library, the outputs of the 3D point cloud and intensity level or depth information and intensity level are obtained after that.

Finally, these data mentioned above are written into text-based files, in which each text file is a frame of the original data. The following workflow of extracting data from a stream file to multi text-based files is outlined in Figure 4-18.

4.11.6 Convert Text Files into MAT Files

After the data extracted from the Argos3D stream files, the text-based data are then converted to MAT files to be used in later imaging processes. The outputs of this converting process are multiple MAT files. These MAT files are used instead of image files because they are convenient for analyzing images in the later steps. This converting process is implemented in Matlab 2016 environment.

4.11.7 Extracting Pi Camera’s Videos

The module of extracting Pi’s video is implemented to extract all frames from a video file. A simple way is that to use FFMPEG to extract all frames from a video file to image files. In the experiments, a FFMPEG software is deployed in Ubuntu. After installing FFMPEG package, all frames are extracted by using a command of `ffmpeg –i inputvideo.h264 –vf fps=10 $outputfilename%03d.jpg`.

CHAPTER 5 - EXPERIMENTAL RESULTS AND DISCUSSION

This section describes and discusses experiment results for the thesis as follows: the settings of the proposed platform for measuring canola plants in both field and laboratory environments (Section 5.1); the counting of canola branches (Section 5.2); the counting of canola seedpods (Section 5.3); the estimation of canola plant height (Section 5.4); the experiment results for fusing multi-focus images (Section 5.5).

5.1 Testing in Cross Environments

In this study, the Argos3D-P100, Kinect V2, Sony A58, and Pi cameras were used in the laboratory-based environment. First, a combination of the Argos3D-P100 and Sony A58 was used to compare with the other combination of the Kinect V2 and Sony A58. Then, a proposed mobile platform, in which the Argos3D P100 and Pi cameras combined, was deployed in both controlled environment and field scenarios. After applying these methodologies, the best approach would be proposed. The experimental results are shown below.

5.1.1 Field Tests

The measurements in the field were conducted at dusk (8.30 – 9.30PM). This time period was chosen because this low level of brightness has the least effect on the Argos3D P100 camera, making the measurements of canola growth most reliable at this time. In the canola field of the University of Saskatchewan (Figure 5-1), canola plant images were captured from the top view and side view by using a portable low-cost depth plant phenotyping system mounted on the boom of a swather or a sprayer as shown in Figure 5-2.

Figure 5-1. Canola field (August 2017)

Figure 5-2. The designed system mounted on a swather (left) and a sprayer (right)

The proposed system allows the capture of plant images in video stream format by using a remote control. The raw data were stored on the 32GB SD card in the Raspberry Pi3, then transferred to the PC for further imaging processes.

5.1.2 Laboratory Tests

To capture images of canola plants for detecting and counting the seedpods, a digital camera (Sony A58) was used. Five side views 3872 x 2576 resolution RGB images were taken of every plant in the lab. The raw images were stored in ARW format. A total of thirty (30) canola plants were used for this study to develop the model and ensure sufficient variation. The plants were randomly selected in the canola field of the University of Saskatchewan. The experiments were conducted in the summers of 2016 and 2017.

To count the number of canola branches and seedpods and to compare the results with other methodologies (for example using a Kinect V2 instead of using an Argos3D P100), a proposed mobile phenotyping platform was used. The laboratory test set-up is illustrated in Figure 5-3. The methods described in this study were tested on canola datasets. Most of the canola plants were grown in the field, while some were grown in the greenhouse.

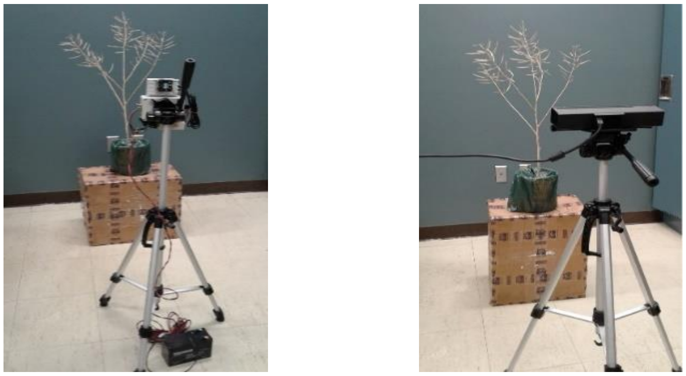

(a) (b)

Figure 5-3. A setting of the proposed mobile platform (a) and Kinect V2 (b)

5.2 Detection and Counting Canola Branches

Two approaches were used to detect and count canola branches in indoor by using the Argos3D camera and Kinect V2 camera. A comparison of each camera performance is shown in the next section.

5.2.1 Using an Argos3D Camera

To detect and count the number of canola branches, two approaches using 3D point cloud and grayscale information acquired from the Argos3D camera were used. Each approach had advantages and disadvantages. Although using 3D point cloud results in some advantages for extracting the targeted object or removing the background by using size filters, the quality image of the targeted object was too low. The grayscale information offers a higher quality image than 3D point cloud, but it is more difficult to remove the background. A 3D point cloud-based approach to detect and count canola branches was used through several steps. First, a 3D point cloud of the canola plant was extracted from the Argos3D-P100 by using APIs mentioned in the MatlabSDK_BtaP100 package. Then, the noise and background of this depth image was removed by applying a size filter as illustrated in Figure 5-4.

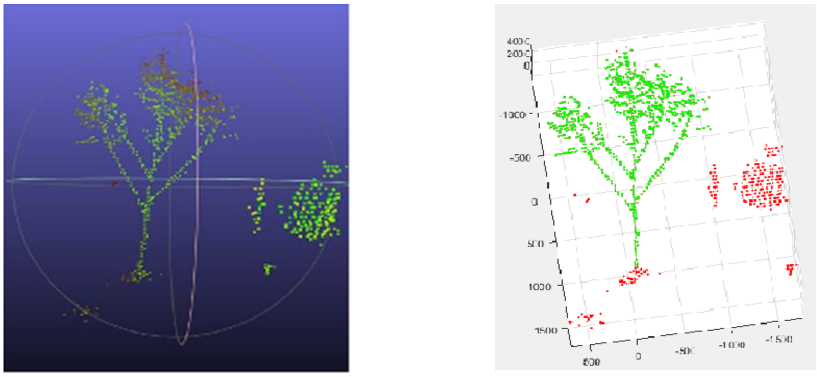

a) b)

Figure 5-4. The original 3D point cloud (a) and its filtered point cloud (green color) (b)

From the 3D cleaned point cloud above, a 2D image was extracted and then converted to grayscale, as illustrated in Figure 5-5.

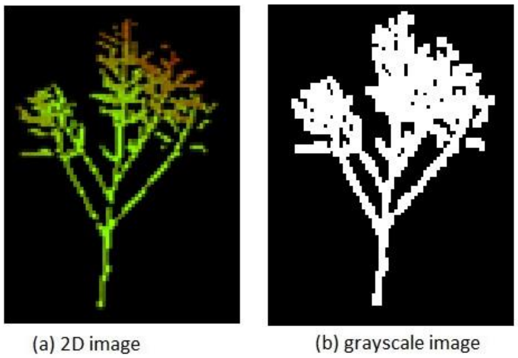
(a) 2D image (b) grayscale image

Figure 5-5. 2D image and its grayscale image

Based on the grayscale image, a skeleton of the canola plant was obtained, which was then applied to a tubeness filter to make the skeleton smoother before investigating the area of interest (ROI). The ROI, containing stem and branches, was examined to remove unwanted parts of the canola plant. Therefore, the remaining parts consisted of a stem and branches, as illustrated in Figure 5-6. Finally, based on the ROI information, an algorithm for counting the number of branches was deployed, the results of which are illustrated in Figure 5-6(c). This approach met some obstacles, for example, less number of points for each canola branch leading to the difficulty to obtain plant' 3D skeleton or 2D skeleton. This is the reason why the 3D skeleton algorithm was not investigated in this research.

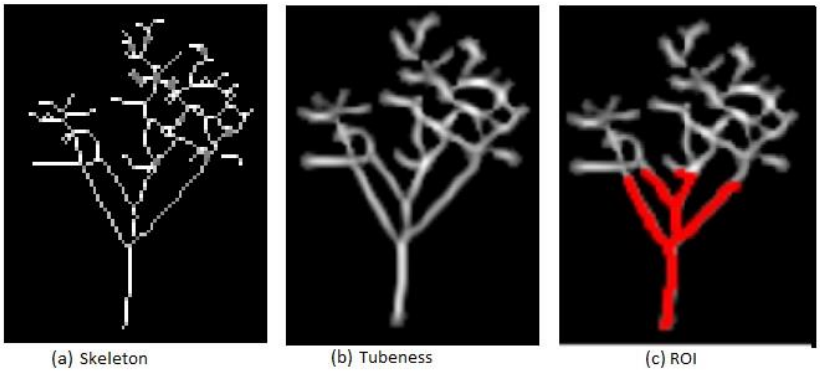
(a) Skeleton (b) Tubeness (c) ROI

Figure 5-6. Skeleton, tubeness, and ROI of the canola plant

Another significant finding was that instead of using 3D point cloud, depth and intensity level information can be beneficial for detecting and counting canola branches. Depth data and intensity information were examined and offered promising approaches. The workflow of this approach is described in Chapter 3. First, either a distance (depth) image or an amplitude image (intensity level) was acquired from the Argos3D camera. Next, this image was applied to some filters (size filter and Gaussian low pass filter) to remove the background and noise and then to smooth the image as shown in Figure 5-7. These depth and intensity-level images provided higher quality than 3D-point cloud images.

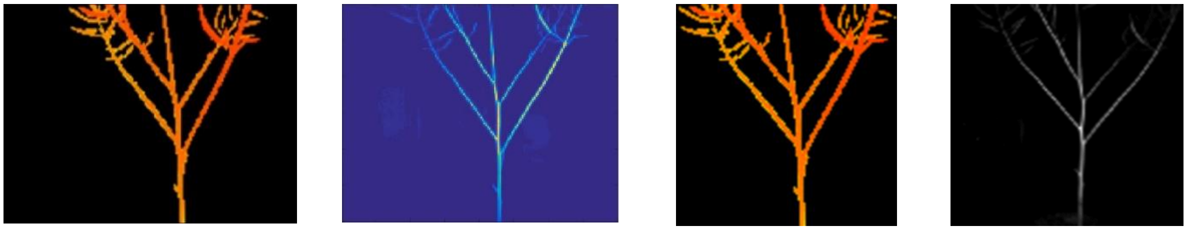

a) Original depth image b) Original intensity level c) Filtered depth image d) Filtered Intensity level

Figure 5-7. Depth and intensity level images before and after filtered

In this approach, environmental surroundings needed to be known to reduce the noise and backgrounds appearing in the acquired images. To gain the best quality of distance information, the common procedure is to remove any background that reflects infrared radiation (e.g., metal materials). To determine the intensity level, a solid background with at least 50 centimeters from the object was the best choice in our experiments. The noise and background was perfectly removed by an empirical threshold of intensity level (threshold T = 600).

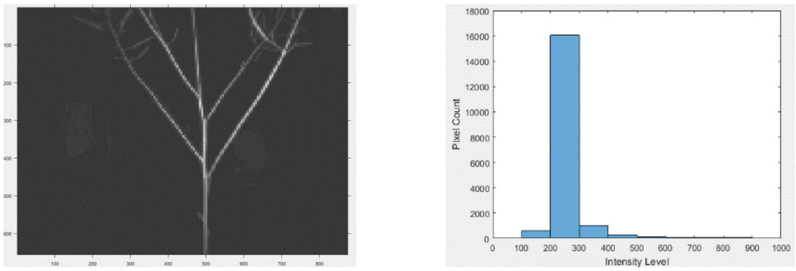

(a) Original grayscale image b) Histogram of the original image

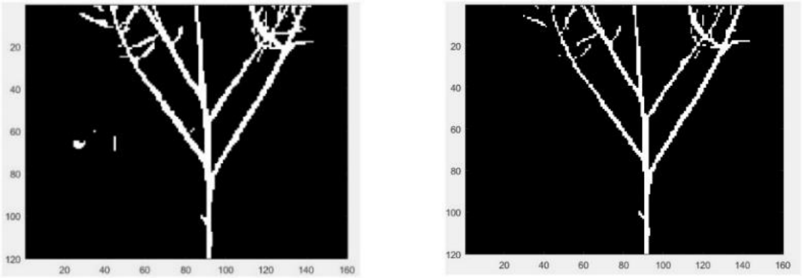

c) Filtered image with T = 400 d) Filtered image with T = 600

Figure 5-8. An example of the filtering background noise by empirical thresholds.

When the threshold was less than 600, for example, T = 400, the output contained unwanted objects in the background; however, these unwanted objects were removed in the output when the threshold was increased to 600, as shown in Figure 5-8(c) and Figure 5-8(d), respectively. The original grayscale, the histogram of the original image, and the filtered image with different thresholds are illustrated in Figure 5-8. In addition to removing the background and noise, the Gaussian smoother filter greatly contributes to the outcomes of this branch-detection algorithm. In the experiments, the standard deviation (σ = 1.7) was applied. When this standard deviation increased, the output image became smoother, but the detection of branches was affected by the large standard deviation. Figure 5-9, for example, demonstrates the output after applying a Gaussian smoother filter with a different value of standard deviation.

(a) σ = 1.7 (b) σ = 5 (c) σ = 7

Figure 5-9. The results after applying a Gaussian smoother filter with a different value of σ=1.7, 5, and 7

From these filtered images after removing the background and noise, a ROI was retrieved and then applied to a fast matching algorithm to find the skeleton. Finally, the number of canola branches was calculated, as shown in Figure 5-10.

(a) ROI (b) The skeleton and results

Figure 5-10. The area of interest (ROI) (a) and the skeleton of the canola plant (b)

Overall, these results suggest that the Argos3D P100 camera can be used to detect and count the number of branches in many ways, depending on how the data are acquired.

To evaluate the performance of the proposed algorithm for detecting and counting canola branches, thirty individual canola plants were captured and processed. To provide a referenced number of canola branches, a method of manually counting the number of canola branches was used as a ground truth. In addition, a relative error rate was used to express the accuracy of these experiment results, given by:

$$Relative\ error = \frac{|Manual\ counting\ result - Automatic\ counting\ result|}{Manual\ counting\ result} * 100\% \qquad (5.1)$$

The comparisons of the automatic and manual counting the canola branches are presented in Table 5-1.

Table 5-1. Results of automatic and manual counting the canola branches from the Argos3D P100

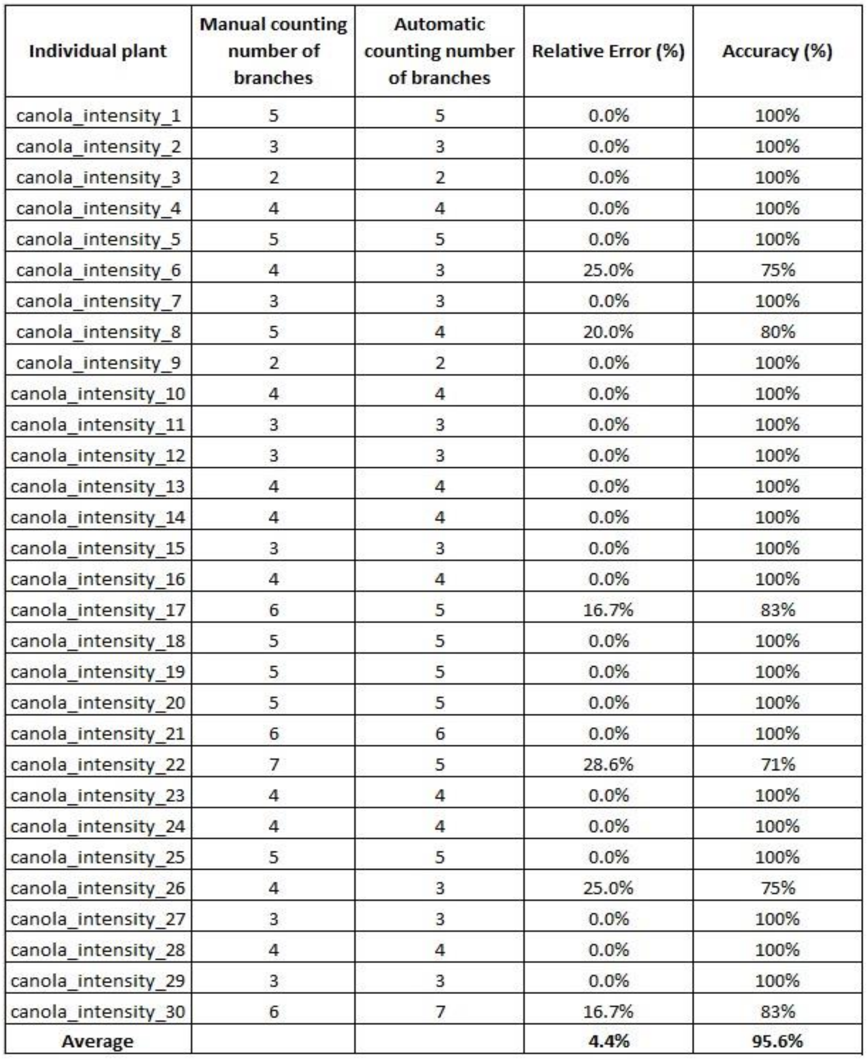

Individual plant	Manual counting number of branches	Automatic counting number of branches	Relative Error (%)	Accuracy (%)
canola_intensity_1	5	5	0.0%	100%
canola_intensity_2	3	3	0.0%	100%
canola_intensity_3	2	2	0.0%	100%
canola_intensity_4	4	4	0.0%	100%
canola_intensity_5	5	5	0.0%	100%
canola_intensity_6	4	3	25.0%	75%
canola_intensity_7	3	3	0.0%	100%
canola_intensity_8	5	4	20.0%	80%
canola_intensity_9	2	2	0.0%	100%
canola_intensity_10	4	4	0.0%	100%
canola_intensity_11	3	3	0.0%	100%
canola_intensity_12	3	3	0.0%	100%
canola_intensity_13	4	4	0.0%	100%
canola_intensity_14	4	4	0.0%	100%
canola_intensity_15	3	3	0.0%	100%
canola_intensity_16	4	4	0.0%	100%
canola_intensity_17	6	5	16.7%	83%
canola_intensity_18	5	5	0.0%	100%
canola_intensity_19	5	5	0.0%	100%
canola_intensity_20	5	5	0.0%	100%
canola_intensity_21	6	6	0.0%	100%
canola_intensity_22	7	5	28.6%	71%
canola_intensity_23	4	4	0.0%	100%
canola_intensity_24	4	4	0.0%	100%
canola_intensity_25	5	5	0.0%	100%
canola_intensity_26	4	3	25.0%	75%
canola_intensity_27	3	3	0.0%	100%
canola_intensity_28	4	4	0.0%	100%
canola_intensity_29	3	3	0.0%	100%
canola_intensity_30	6	7	16.7%	83%
Average			**4.4%**	**95.6%**

The estimated results are very close to the manual results, 95.6% accuracy on average. As the results illustrate in Table 5-1, the average error rate is small, about 4.4%, in which, 6/30 results were inaccurate. These inaccurate results may be caused by some uncontrolled factors, such as adjacent, overlapping branches and background noise. The main difficulty of detecting and counting branches was to detecting branches in merging regions that are partially overlapped or stuck to one another. Although the branches could be easily identified by human sight, these overlapping branches were difficult to detect by image processing techniques. This issue occurred because the level of pixels in the region of the overlapping branches did not change in intensity. For example, the canola plant number 22nd had seven branches; however, only five were detected instead of seven branches because one branch was overlapped another and another branch was adjacent to a second branch.

Similarly, one of the branches was stuck to another; therefore, the number of branches was counted as three-fourth (3/4) and four-fifths (4/5) branches for plant number 6th and plant number 8th, respectively. These obstacles should be resolved to improve the accuracy rate of the algorithm for detecting and counting branches.

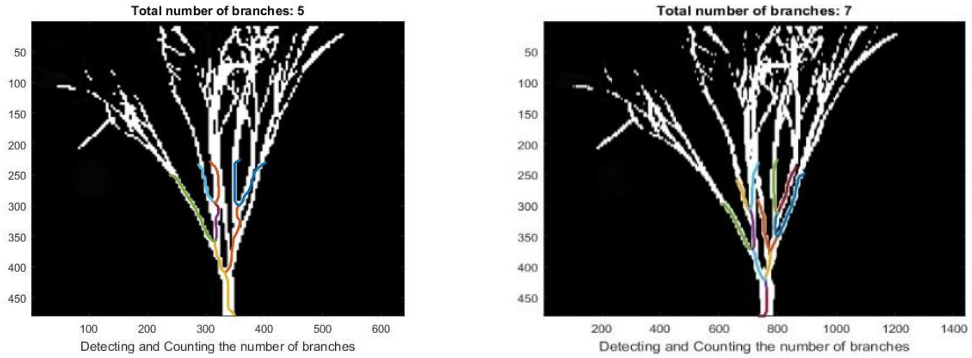

a) The result before applying horizontal resizing of the image

b) The result after applying horizontal resizing of the image

Figure 5-11. An example of the solution for sticking branches

Fortunately, there are some worthwhile solutions to these problems. First, each canola plant should be captured by multiple views, in which, the overlapping branches can be identified. Second, in the case of adjacent branches, the horizontal size of the image needs to be increased, so the adjacent branches can be separated, and easily recognized, as shown in the results depicted in Figure 5-11. Third, any other surrounding objects should be moved out of the camera's field of view. Finally, the image with and without the plant should be retrieved and the background removed by subtracting these images with and without the plant. Overall, the data from this study suggest that the algorithm for detecting and counting canola branches offers a high accuracy measurement and can be achieved through grayscale information or 3D point cloud obtained from the Argos3D P100 camera.

5.2.2 Using a Kinect V2 Camera

In contrast to the Argos3D P100, which can acquire depth information without light, the Kinect V2 requires precise illumination to capture a point cloud of the canola plant. However, in this research, the 3D images had better resolution quality than the Argos3D P100, as shown in Figure 5-12. From the 3D point cloud, a 3D size filter was applied to remove the noise and background, as seen in Figure 5-13.

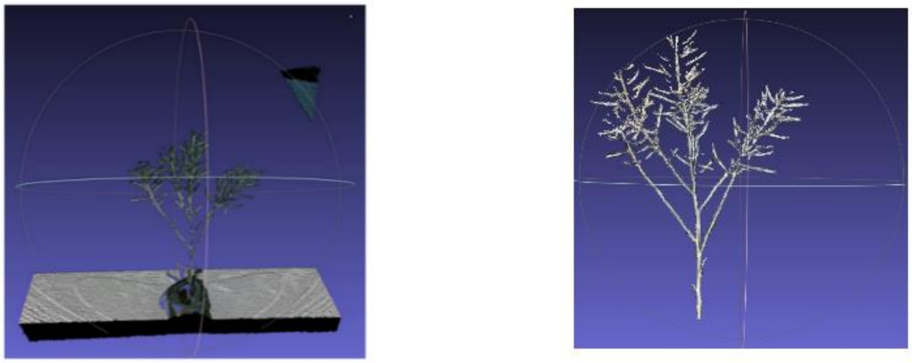

a) A 3D point cloud

b) The Filtered 3D point cloud

Figure 5-12. A 3D point cloud acquired from the Kinect V2 camera

After the noise and background were removed, the 2D image was retrieved from the cleaned 3D point cloud. After that, grayscale and binary images of the 2D image were converted before obtaining the ROI of the canola plant, as shown in Figure 5-14. Because the input image had jagged edges, a dilation algorithm was used to enlarge and smooth the ROI.


(a) 2D image (b) Binary image (c) ROI

Figure 5-13. Extracting 2D image (a), binary image (b), and ROI of the canola plant (c)

Based on the ROI information, the skeleton of the ROI was examined. The results of the detection and counting of the branches are given in Figure 5-14.


(a) The skeleton (b) Results

Figure 5-14. The skeleton (a) and results of counting canola branches (b)

Similar to the algorithm for detecting and counting canola branches shown in Section 5.2.1, this algorithm can use depth or infrared images acquired from the Kinect V2 camera to detect and count canola branches. Figure 5-15 illustrates the outputs of this detection algorithm.

(a) RGB image (b) Depth image (c) Infrared image

(d) Binary (e) ROI (f) The results

Figure 5-15. The results of the branches detection algorithm

Similar to the evaluation of the detection algorithm performance in the Argos3D's data set, thirty individual canola plants were captured by the Kinect V2 camera and processed. To provide referenced numbers of canola branches, the canola branches were counted manually. A relative error rate was used to show the accuracy of these experiment results, as given in Equations (5.2) and (5.3). The comparisons of the automatic and manual counting of canola branches are presented in Table 5-2.

Table 5-2. Results of automatic and manual counting of canola branches from the Kinect V2

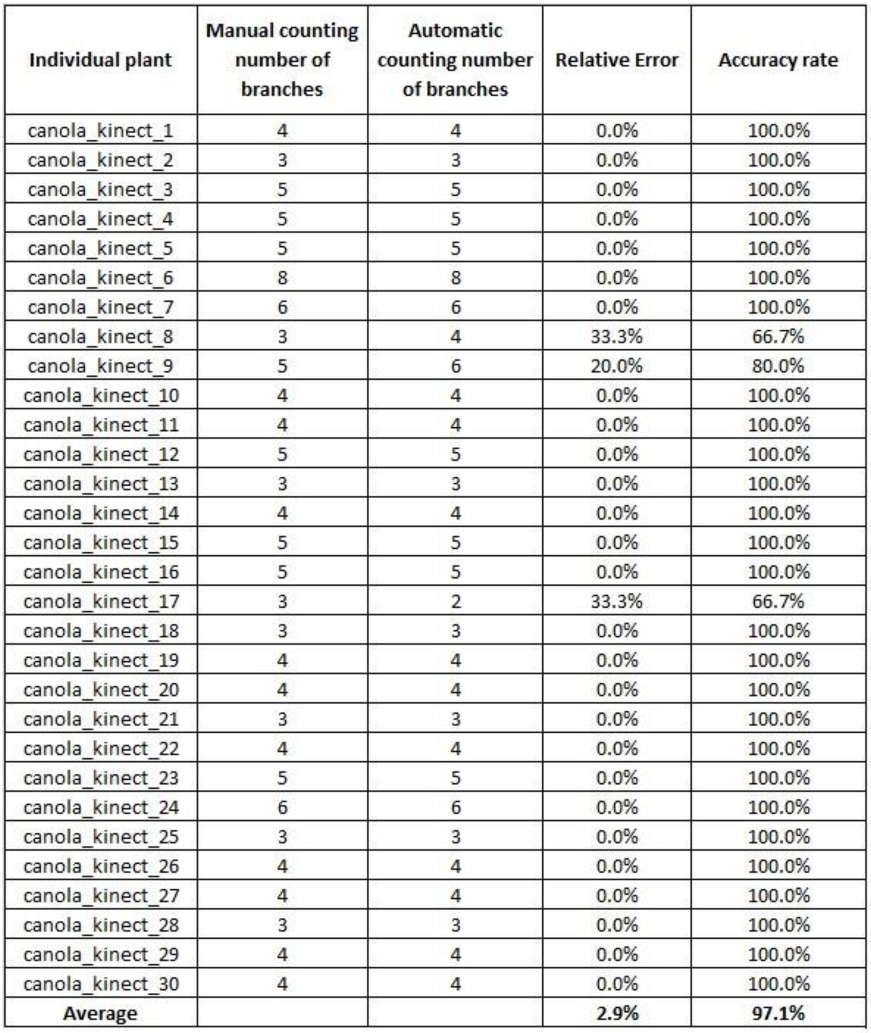

Individual plant	Manual counting number of branches	Automatic counting number of branches	Relative Error	Accuracy rate
canola_kinect_1	4	4	0.0%	100.0%
canola_kinect_2	3	3	0.0%	100.0%
canola_kinect_3	5	5	0.0%	100.0%
canola_kinect_4	5	5	0.0%	100.0%
canola_kinect_5	5	5	0.0%	100.0%
canola_kinect_6	8	8	0.0%	100.0%
canola_kinect_7	6	6	0.0%	100.0%
canola_kinect_8	3	4	33.3%	66.7%
canola_kinect_9	5	6	20.0%	80.0%
canola_kinect_10	4	4	0.0%	100.0%
canola_kinect_11	4	4	0.0%	100.0%
canola_kinect_12	5	5	0.0%	100.0%
canola_kinect_13	3	3	0.0%	100.0%
canola_kinect_14	4	4	0.0%	100.0%
canola_kinect_15	5	5	0.0%	100.0%
canola_kinect_16	5	5	0.0%	100.0%
canola_kinect_17	3	2	33.3%	66.7%
canola_kinect_18	3	3	0.0%	100.0%
canola_kinect_19	4	4	0.0%	100.0%
canola_kinect_20	4	4	0.0%	100.0%
canola_kinect_21	3	3	0.0%	100.0%
canola_kinect_22	4	4	0.0%	100.0%
canola_kinect_23	5	5	0.0%	100.0%
canola_kinect_24	6	6	0.0%	100.0%
canola_kinect_25	3	3	0.0%	100.0%
canola_kinect_26	4	4	0.0%	100.0%
canola_kinect_27	4	4	0.0%	100.0%
canola_kinect_28	3	3	0.0%	100.0%
canola_kinect_29	4	4	0.0%	100.0%
canola_kinect_30	4	4	0.0%	100.0%
Average			**2.9%**	**97.1%**

The estimated results are very close to the manual count results, an average of 97.1% accuracy is obtained. Based on the outputs shown in Table 5-2, the average error rate is smaller than the average error rate using the Argos3D's dataset, about 2.9%, in which, three of thirty cases (10%) are inaccurate. This average error rate is lower than the average error rate based on the Argos3D dataset because the input images acquired from the Kinect V2 have a higher resolution. The average error rate from the Kinect's data set had some inaccurate results, caused by reasons described in Section 5.2.1. Adjacent branches, as seen in plants number 8, 9, and 17, were one cause. To deal with inaccurate results, the solutions investigated in Section 5.2.1 can be used. The evidence from this research suggests that the Kinect V2 can be used to detect and count canola branches through 3D point cloud or infrared images.

From the results mentioned above, it can be seen that, due to its characteristics and system set-up, the Argos3D P100 camera is more suitable for phenotyping mobile device than is Kinect V2. The Argos3D P100 consumes less power and uses the small computer Raspberry Pi with a 2.0 USB port to operate. The Kinect V2 requires a higher power requirement and a desktop or laptop computer with a 3.0 USB port. In addition, the dimensions and weights of the Argos3D P100 are much smaller than those of the Kinect V2. Therefore, the Argos3D P100 was chosen instead of the Kinect V2 for the depth camera of the proposed platform.

5.2.3 Limitations

The counting branches method is limited by the quality of the source images, plant structure and applicable only on single plants in indoor conditions. The results show that higher accuracy was achieved if the canola branches were counted by using clear images and fewer branches overlapping. However, the proposed method has certain limitations in counting more complex plants or dealing with background noise. If a canola plant has many branches that occlude each other, the algorithm will have great difficulty detecting them. In addition, because of the use of infrared lights, the Argos3D-P100 images suffered from strong ambient light and a metal-background. To avoid these problems, the images should be taken in low ambient light and with a non-metal background or surroundings. This method is also limited to laboratory phenotyping because it can only deal with a single plant. Canola plants in the field are lodged together and the branches counting method requires further developing.

5.3 Detection and Counting Canola Seedpods

5.3.1 Using a High-Resolution Digital Camera

To count canola seedpods in the lab setting, images of thirty individual canola plants were taken by the Sony A58 with different view angles. As seen in the workflow introduced in Chapter 3, each color image was converted into a grayscale image and then tube-like structures (vessels) were distinguished by applying the Frangi 2D Vesselness filter, as shown in Figure 5-16. By using the result after applying the Frangi filter, the skeleton of the plant was extracted. Finally, the skeleton was refined before the endpoints in the skeleton of the canola were detected. With these endpoints, the seedpods were detected, and then the number of seedpods was estimated. This process is shown in Figure 5-17.

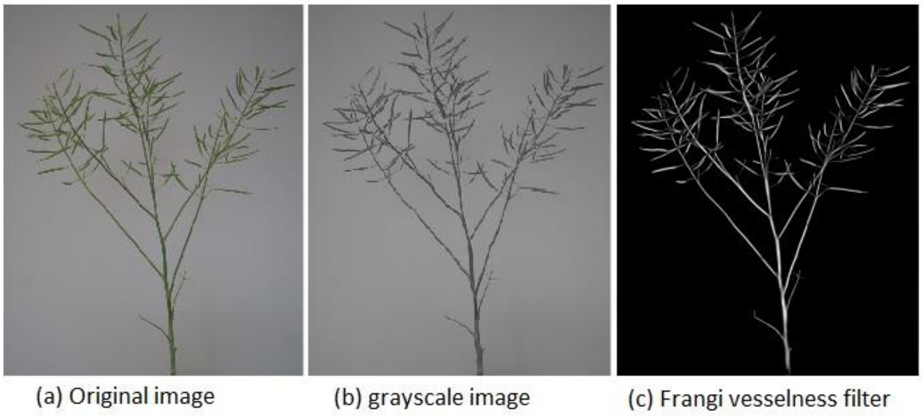
(a) Original image (b) grayscale image (c) Frangi vesselness filter

Figure 5-16. The original image (a), the grayscale image (b), and the filtered image

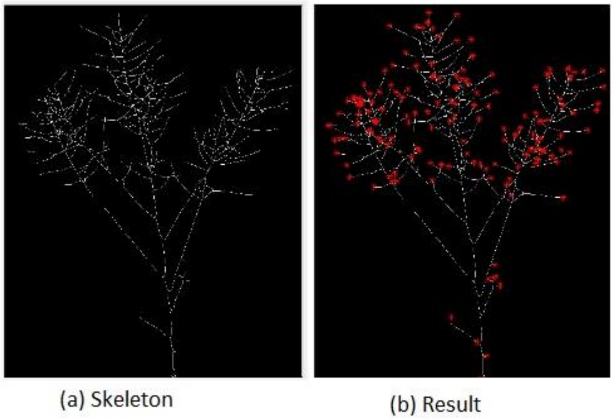
(a) Skeleton (b) Result

Figure 5-17. The skeleton and the results of counting canola seedpods

Similar to the algorithm for detecting and counting canola branches, a methodology of quantitative performance evaluation for counting canola seedpods was examined. Thirty individual canola plants with three different angle view images were captured and automatically processed. To provide referenced numbers of canola seedpods, manual counting the canola seedpods was applied. To express the accuracy of these experiment results, a relative error rate was used:

$$Relative\ error = \frac{|M - Avg|}{M} * 100\% \tag{5.2}$$

where *M* is the manual counting result, *Avg* is the average of the automatic counting result. In this formula, the average of automatic counting results was calculated by:

$$Avg = \frac{\sum_{1}^{3} Automatic\ counting\ result}{3} \tag{5.3}$$

The comparisons of the automatic and manual counting of canola seedpods are presented in Table 5-3. The manual results and estimated results are very close, with an average of 91.4%

accuracy. Because the algorithm detected and counted all canola ‘spikes’ and seedpods, the number of canola ‘spikes’ contributes to the relative errors in counting. Spikes are the sharp points located at the end of the stems and branches, but they not are the seedpods. Since the percentage of canola spikes is quite high, about 9.1 %, the average error rate reaches 8.6 %. The results of counting canola seedpods and the percentage of canola spikes and seedpods are shown in Table 5-3 and Table 5-4, respectively.

Table 5-3. Results of the automatic and manual counting of canola seedpods

Individual plant	Manual counting number of seedpods	Automatic counting number of seedpods			Average of automatic counting number of seedpods	Relative Error	Accuracy rate
		AngleView 1	AngleView 2	AngleView 3			
canola_plant_1	117	120	139	137	132	12.8%	87%
canola_plant_2	120	136	124	137	133	10.3%	90%
canola_plant_3	110	116	124	116	119	7.9%	92%
canola_plant_4	83	93	89	90	91	9.2%	91%
canola_plant_5	67	66	73	64	68	5.0%	95%
canola_plant_6	63	56	67	70	65	9.5%	90%
canola_plant_7	113	109	108	112	110	2.9%	97%
canola_plant_8	140	156	158	138	151	8.6%	91%
canola_plant_9	145	155	149	160	155	6.7%	93%
canola_plant_10	101	116	116	113	115	13.9%	86%
canola_plant_11	90	101	101	102	102	12.6%	87%
canola_plant_12	100	110	113	109	111	10.7%	89%
canola_plant_13	66	71	72	77	74	11.1%	89%
canola_plant_14	58	65	62	67	65	11.5%	89%
canola_plant_15	47	55	56	55	56	17.7%	82%
canola_plant_16	135	148	147	142	146	7.9%	92%
canola_plant_17	70	78	77	79	78	11.4%	89%
canola_plant_18	132	141	136	134	137	3.8%	96%
canola_plant_19	95	97	97	101	99	3.5%	96%
canola_plant_20	61	67	60	69	66	8.2%	92%
canola_plant_21	125	133	137	140	137	9.3%	91%
canola_plant_22	65	68	70	68	69	5.6%	94%
canola_plant_23	72	71	86	71	76	7.4%	93%
canola_plant_24	126	132	133	139	135	6.9%	93%
canola_plant_25	104	109	116	123	116	11.5%	88%
canola_plant_26	99	105	106	108	107	7.4%	93%
canola_plant_27	140	152	130	149	144	7.4%	93%
canola_plant_28	135	143	141	145	143	5.9%	94%
canola_plant_29	141	151	151	149	151	6.6%	93%
canola_plant_30	122	130	131	120	127	5.2%	95%
Average						**8.6%**	**91.4%**

Table 5-4. Percentage of canola spikes

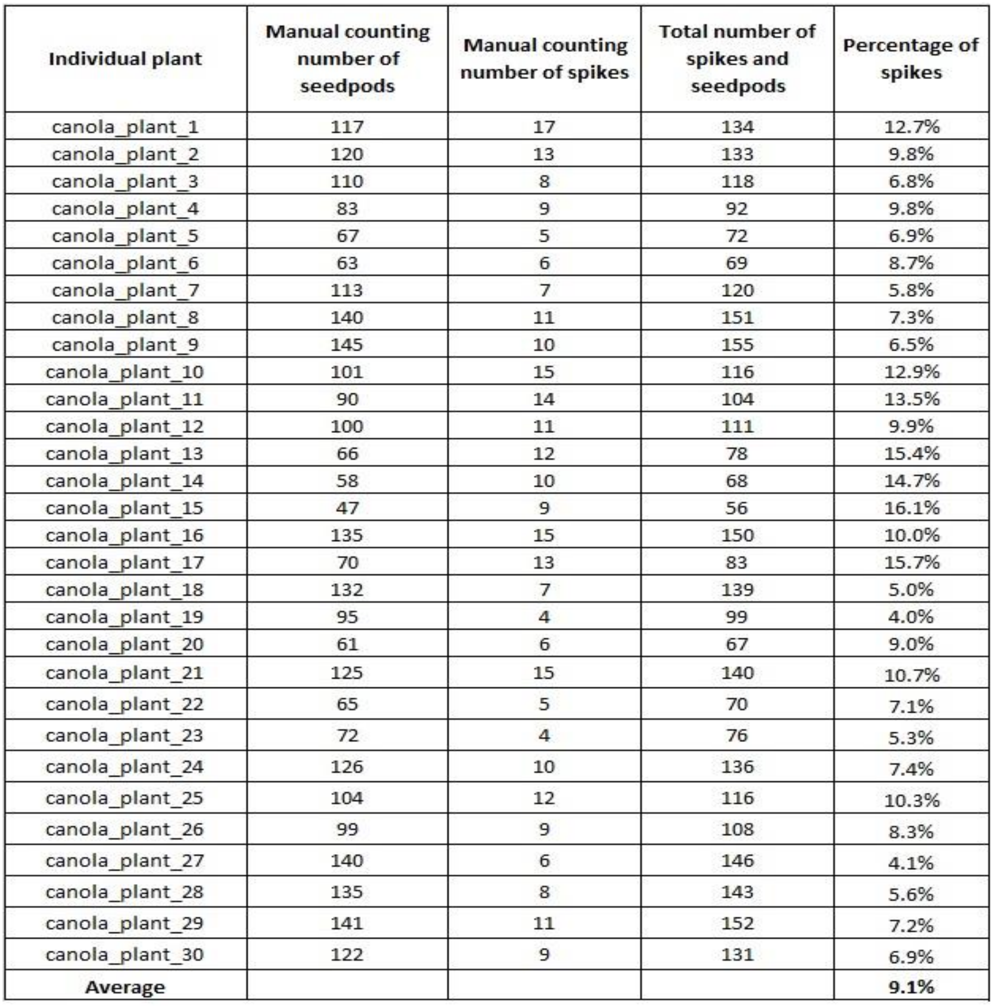

Individual plant	Manual counting number of seedpods	Manual counting number of spikes	Total number of spikes and seedpods	Percentage of spikes
canola_plant_1	117	17	134	12.7%
canola_plant_2	120	13	133	9.8%
canola_plant_3	110	8	118	6.8%
canola_plant_4	83	9	92	9.8%
canola_plant_5	67	5	72	6.9%
canola_plant_6	63	6	69	8.7%
canola_plant_7	113	7	120	5.8%
canola_plant_8	140	11	151	7.3%
canola_plant_9	145	10	155	6.5%
canola_plant_10	101	15	116	12.9%
canola_plant_11	90	14	104	13.5%
canola_plant_12	100	11	111	9.9%
canola_plant_13	66	12	78	15.4%
canola_plant_14	58	10	68	14.7%
canola_plant_15	47	9	56	16.1%
canola_plant_16	135	15	150	10.0%
canola_plant_17	70	13	83	15.7%
canola_plant_18	132	7	139	5.0%
canola_plant_19	95	4	99	4.0%
canola_plant_20	61	6	67	9.0%
canola_plant_21	125	15	140	10.7%
canola_plant_22	65	5	70	7.1%
canola_plant_23	72	4	76	5.3%
canola_plant_24	126	10	136	7.4%
canola_plant_25	104	12	116	10.3%
canola_plant_26	99	9	108	8.3%
canola_plant_27	140	6	146	4.1%
canola_plant_28	135	8	143	5.6%
canola_plant_29	141	11	152	7.2%
canola_plant_30	122	9	131	6.9%
Average				**9.1%**

The accuracy of the proposed algorithm is presented in Table 5-5. It can be seen that the accuracy of the proposed counting algorithm reached about 92%. To deal with this drawback, an improvement to the algorithm was proposed. To reduce these error rates in counting canola seedpods, the number of canola spikes must be eliminated. It is possible to hypothesize that the result of each measurement for counting canola seedpods was estimated by:

$$R = \begin{cases} A - Sp, & if\ A > M \\ A + Sp, & otherwise \end{cases} \tag{5.4}$$

where *R* is the result of estimating a number of seedpods after eliminating spikes, *A* is the average result of the automatic counting of canola seedpods, *M* is the result of manual counting number of canola seedpods, and *Sp* is the estimated number of spikes based on the relationship between *A* and the percentage of canola spikes. *Sp* was calculated by:

$$Sp = A * n \tag{5.5}$$

where n is the percentage of canola spikes.

Table 5-5. The accuracy of the automatic counting of canola seedpods

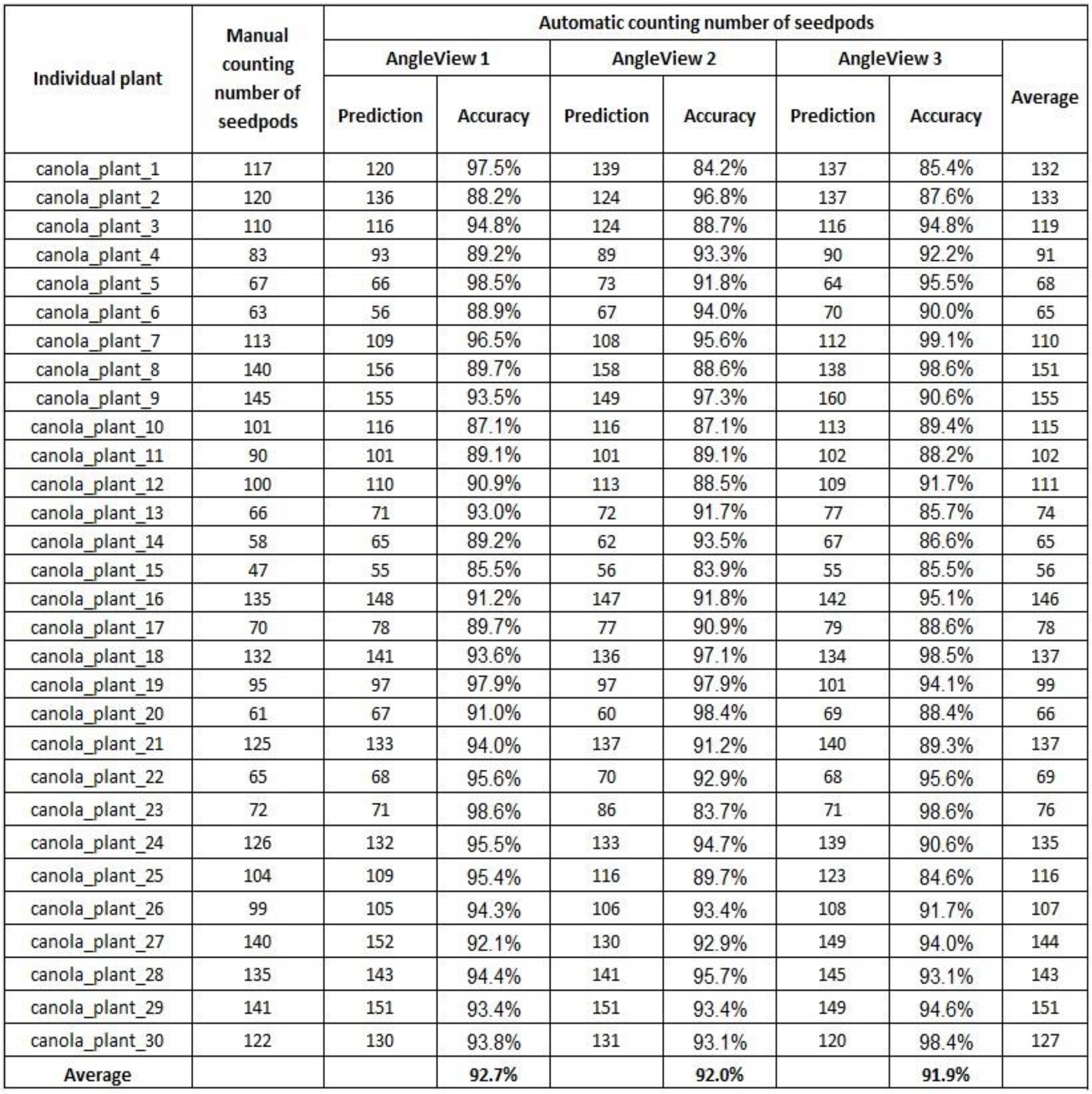

Individual plant	Manual counting number of seedpods	Automatic counting number of seedpods						
		AngleView 1		AngleView 2		AngleView 3		Average
		Prediction	Accuracy	Prediction	Accuracy	Prediction	Accuracy	
canola_plant_1	117	120	97.5%	139	84.2%	137	85.4%	132
canola_plant_2	120	136	88.2%	124	96.8%	137	87.6%	133
canola_plant_3	110	116	94.8%	124	88.7%	116	94.8%	119
canola_plant_4	83	93	89.2%	89	93.3%	90	92.2%	91
canola_plant_5	67	66	98.5%	73	91.8%	64	95.5%	68
canola_plant_6	63	56	88.9%	67	94.0%	70	90.0%	65
canola_plant_7	113	109	96.5%	108	95.6%	112	99.1%	110
canola_plant_8	140	156	89.7%	158	88.6%	138	98.6%	151
canola_plant_9	145	155	93.5%	149	97.3%	160	90.6%	155
canola_plant_10	101	116	87.1%	116	87.1%	113	89.4%	115
canola_plant_11	90	101	89.1%	101	89.1%	102	88.2%	102
canola_plant_12	100	110	90.9%	113	88.5%	109	91.7%	111
canola_plant_13	66	71	93.0%	72	91.7%	77	85.7%	74
canola_plant_14	58	65	89.2%	62	93.5%	67	86.6%	65
canola_plant_15	47	55	85.5%	56	83.9%	55	85.5%	56
canola_plant_16	135	148	91.2%	147	91.8%	142	95.1%	146
canola_plant_17	70	78	89.7%	77	90.9%	79	88.6%	78
canola_plant_18	132	141	93.6%	136	97.1%	134	98.5%	137
canola_plant_19	95	97	97.9%	97	97.9%	101	94.1%	99
canola_plant_20	61	67	91.0%	60	98.4%	69	88.4%	66
canola_plant_21	125	133	94.0%	137	91.2%	140	89.3%	137
canola_plant_22	65	68	95.6%	70	92.9%	68	95.6%	69
canola_plant_23	72	71	98.6%	86	83.7%	71	98.6%	76
canola_plant_24	126	132	95.5%	133	94.7%	139	90.6%	135
canola_plant_25	104	109	95.4%	116	89.7%	123	84.6%	116
canola_plant_26	99	105	94.3%	106	93.4%	108	91.7%	107
canola_plant_27	140	152	92.1%	130	92.9%	149	94.0%	144
canola_plant_28	135	143	94.4%	141	95.7%	145	93.1%	143
canola_plant_29	141	151	93.4%	151	93.4%	149	94.6%	151
canola_plant_30	122	130	93.8%	131	93.1%	120	98.4%	127
Average			**92.7%**		**92.0%**		**91.9%**	

As a result, the error rates of the proposed algorithm for counting seedpods are significantly decreased after eliminating the number of spikes. The error rate is lowered to 3.2% on average after applying Equations (5.4) and (5.5), as presented in Table 5-6. The outputs of this algorithm are shown in Figure 5-18. The results of these experiments support the idea that the proposed algorithms have the potential to highly and accurately detect and count canola seedpods.

Table 5-6. The refined results of automatic counting the canola seedpods

Individual plant	Manual counting number of seedpods	Average of automatic counting number of seedpods	Average number of spikes	Refined results	Average Error rate
canola_plant_1	117	132	12	120	2.6%
canola_plant_2	120	133	12	121	0.8%
canola_plant_3	110	119	11	108	1.8%
canola_plant_4	83	91	8	83	0.0%
canola_plant_5	67	68	6	62	7.5%
canola_plant_6	63	65	6	59	6.3%
canola_plant_7	113	110	10	120	6.2%
canola_plant_8	140	151	14	137	2.1%
canola_plant_9	145	155	14	141	2.8%
canola_plant_10	101	115	10	105	4.0%
canola_plant_11	90	102	9	93	3.3%
canola_plant_12	100	111	10	101	1.0%
canola_plant_13	66	74	7	67	1.5%
canola_plant_14	58	65	6	59	1.7%
canola_plant_15	47	56	5	51	8.5%
canola_plant_16	135	146	13	133	1.5%
canola_plant_17	70	78	7	71	1.4%
canola_plant_18	132	137	12	125	5.3%
canola_plant_19	95	99	9	90	5.3%
canola_plant_20	61	66	6	60	1.6%
canola_plant_21	125	137	12	125	0.0%
canola_plant_22	65	69	6	63	3.1%
canola_plant_23	72	76	7	69	4.2%
canola_plant_24	126	135	12	123	2.4%
canola_plant_25	104	116	11	105	1.0%
canola_plant_26	99	107	10	97	2.0%
canola_plant_27	140	144	13	131	6.4%
canola_plant_28	135	143	13	130	3.7%
canola_plant_29	141	151	14	137	2.8%
canola_plant_30	122	127	12	115	5.7%
Average					**3.2%**

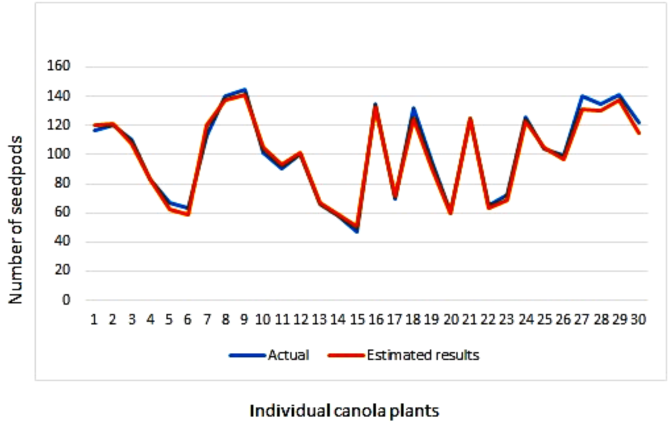

Figure 5-18. Comparing the refined results of the proposed algorithm to the actual results

5.3.2 Limitations

The method for counting seedpods was limited by the quality of the source images (e.g., a clear image, clear seedpods, and a clear background level), the overlapping seedpods, and computational costs. The experiment's results show that the error rate increased for several reasons, such as unclear canola plant images, a complex background, and overlapping seedpods. The clearer the back-ground and seedpods, and the less the seedpods overlap, the fewer the errors. To deal with these problems, a clear image and clear background are required and each canola plant must be captured from different views. A promising solution to the problems might be to capture the plant with different focuses and then to use an image fusion technique, which will be introduced in the next section. The images this technique produces would be fused to obtain clear seedpods.

5.4 Monitoring Canola Growth Stages

This section described a non-contact method of canola plant growth measurement using the proposed mobile platform. The proposed system measures canola plant growth parameters, such as plant height. If plant growth parameters are precisely measured on each plant growth cycle, a detailed model of plant growth can be developed. As well, the system can accurately predict and control the plants for high yield. This section describes how a calibration of the Argos3D camera was first performed before the canola plant heights' were measured. The depth camera must be calibrated to examine the canola plants'-growth stages using distance information. The distance information depends on several Argos3D's parameters, such as a data frame rate and integration time.

5.4.1 Calibration of the Argos3D P100

To calibrate the Argos3D P100, the depth camera was fixed at a distance of 1,631mm, a frame rate of 10fps, and an integration time of two milliseconds (ms). A distance of 300 mm to 1631 mm was explored due to the low resolution (160x120 pixels). The highest accurate measurement recorded was at the distance of 1,000mm, as seen in Table 5-7. Table 5-7 describes the accuracy of distances acquired by the Argos3D P100 at 1,500mm and at an integration time of 1.5ms. In addition, while the frame rate was set at 10fps to reduce the amount of output data without affecting the output quality, the integration time was set at 2ms. This rate and time ensured there was sufficient to measure gray or green objects. The scene of the calibration is shown in Figure 5-19.

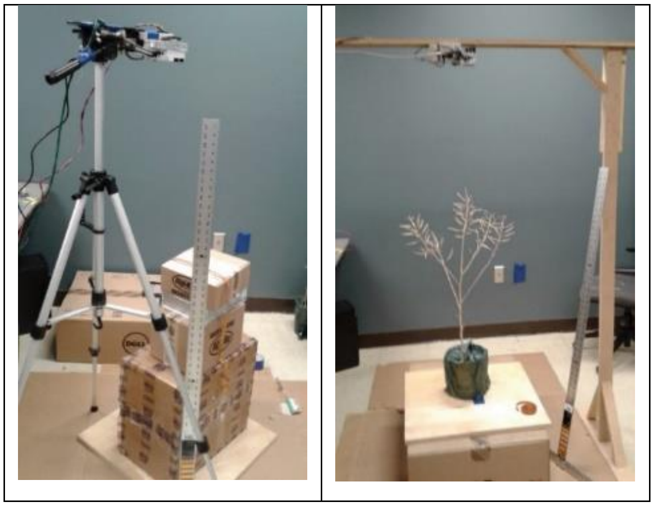

Figure 5-19. Calibrations of the Argos3D with a camera tripod (a) and frame (b).

The process of the depth camera calibration was performed in several steps. First, the offset distance was set at -2,300 (mm). Then, this empirical offset was used for the global offset of the depth camera. Finally, the referenced objects (solid wood and carton boxes) with different distances were used to measure and then to compare the automatic measurements to the actual distances. Furthermore, to increase the accuracy of the automatic measurement process, three automatic measurement results were used to calculate the average of the distance per referenced object. Then the relative error rate was calculated by Equations (5.2) and (5.3).

To increase the accuracy of the height measurement, ten samples with different heights were selected, and the average of each estimated result was calculated from 30 to 50 frames. Table 5-7 shows only the average of estimated results due to its limited space. As a result, the average error rate of the distance measurements is reduced by the calibration process. These results are illustrated in Table 5-7, in which every relative error is reduced more than 5%. The range of low error rates, from 0.07% to 1.65%, occurred at a distance from 1,000mm to 1,400mm, but it gradually increased to 4.05% when the distance from 1,000mm to 418mm was decreased. It can thus be suggested that the best range for measuring plant height is from 1,000mm to 1,400mm, providing the error rate is less than 2%.

Table 5-7. Results of the Argos3D P100's calibration

Distance from Argos3D camera to the object	Frame rate (fps)	Offset distance (mm)	Actual (mm)	Average of estimated results (mm)	Relative Error
Background (solid wood)	10	-2300	1400	1401.02	0.07%
Object 1 (solid wood))	10	-2300	1307	1311.36	0.33%
Object 2 (carton box)	10	-2300	1197	1210.18	1.10%
Object 3 (carton box)	10	-2300	1074	1089.72	1.46%
Object 5 (carton box)	10	-2300	960	975.88	1.65%
Object 6 (carton box)	10	-2300	776	794.82	2.43%
Object 7 (carton box)	10	-2300	677	694.48	2.58%
Object 8 (carton box)	10	-2300	531	545.96	2.82%
Object 9 (carton box)	10	-2300	515	531.82	3.27%
Object 10 (carton box)	10	-2300	418	434.92	4.05%

Table 5-8. Accuracy of distances at 1500mm and an integration time of 1.5ms

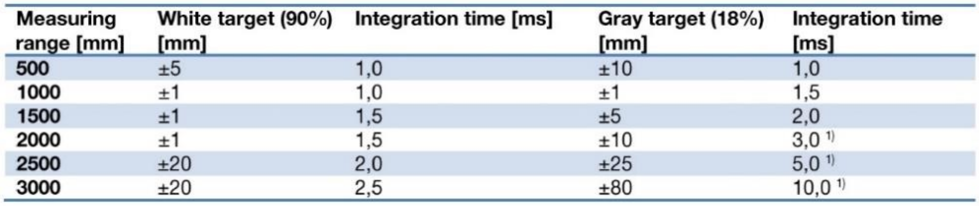

Measuring range [mm]	White target (90%) [mm]	Integration time [ms]	Gray target (18%) [mm]	Integration time [ms]
500	±5	1,0	±10	1,0
1000	±1	1,0	±1	1,5
1500	±1	1,5	±5	2,0
2000	±1	1,5	±10	3,0 1)
2500	±20	2,0	±25	5,0 1)
3000	±20	2,5	±80	10,0 1)

5.4.2 Measuring Height of Individual Canola Plants

Due to the limited canola samples in the winter season, only thirteen canola plants were used to measure plant height. Each canola plant had a different height, ranging from 130 mm to 1319mm (including pod). To expand the height range of these canola plants, some different boxes were added underneath the pods of the canola plants. These plants were directly placed underneath the camera that fixed on the frame at a distance of 1,631mm (see Figure 5-19). Depth data of each plant were extracted from the stream acquired from the Argos3D camera, then converted into MAT.files (Matlab format files) before distance information from the depth camera to the plant was obtained. From the MAT.files, an average of 30 measurements was retrieved. These experiments were conducted in the laboratory, and their results are shown in Figure 5-20. The results of the measurements plant height are presented in Table 5-9. The results reveal that the relative error is quite low, less than 5%, with the high distance between the depth camera and the plant, between 850mm and 1,300mm. However, the relative errors gradually increase up to 12% when the distance between the depth camera and the plant extend greater than 1300mm. This investigation has identified that plant height is easily measured with high accuracy up to nearly

98% by using depth images with a distance from 1,000mm to 1,100mm. Overall, this plant height measurement technique offers an acceptable result with an average error of 8.9%.

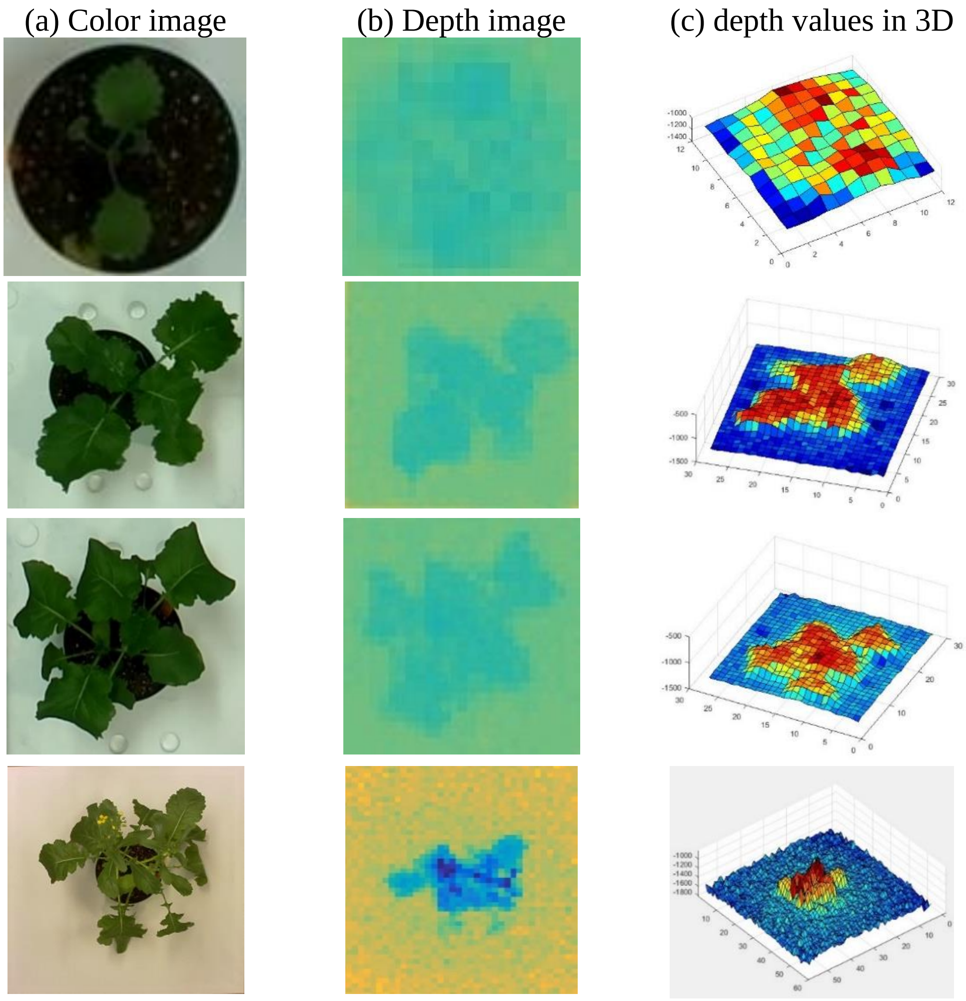
(a) Color image
(b) Depth image
(c) depth values in 3D

Figure 5-20. Some results of the plant height measurements

Table 5-9. Results of the canola plant height measurements

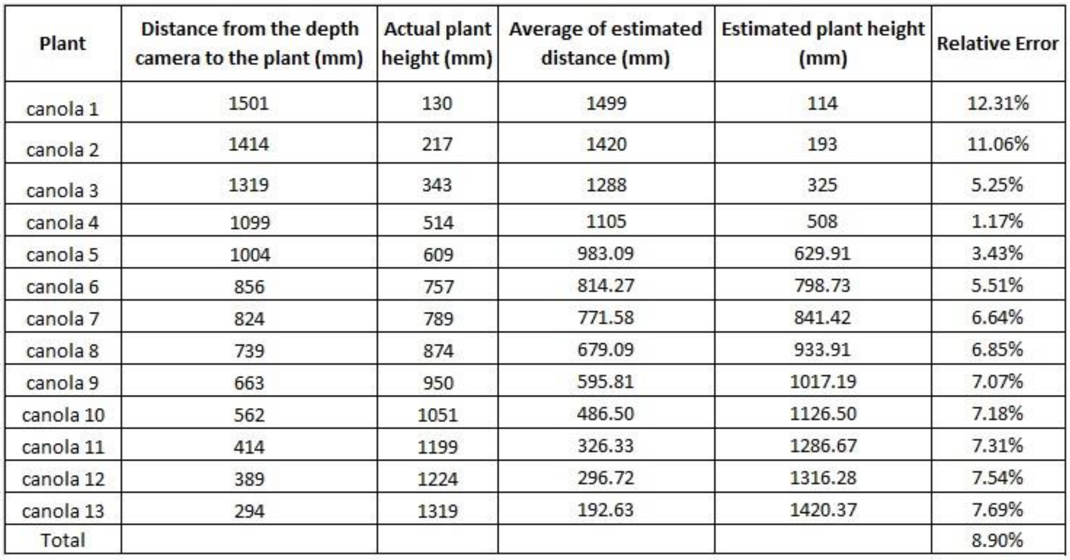

Plant	Distance from the depth camera to the plant (mm)	Actual plant height (mm)	Average of estimated distance (mm)	Estimated plant height (mm)	Relative Error
canola 1	1501	130	1499	114	12.31%
canola 2	1414	217	1420	193	11.06%
canola 3	1319	343	1288	325	5.25%
canola 4	1099	514	1105	508	1.17%
canola 5	1004	609	983.09	629.91	3.43%
canola 6	856	757	814.27	798.73	5.51%
canola 7	824	789	771.58	841.42	6.64%
canola 8	739	874	679.09	933.91	6.85%
canola 9	663	950	595.81	1017.19	7.07%
canola 10	562	1051	486.50	1126.50	7.18%
canola 11	414	1199	326.33	1286.67	7.31%
canola 12	389	1224	296.72	1316.28	7.54%
canola 13	294	1319	192.63	1420.37	7.69%
Total					8.90%

5.4.3 Limitations

The plant-height measurement approach is limited by the distance between the plant and the depth camera. When the plant is placed too close (less than 300 mm) or too far (greater than 1,300 mm), the error rate increased because the depth camera is limited by the range of activity, from 100 mm to 3,000 mm. The solution to this problem is that to place the plant under the depth camera - between 850 mm to 1,300 mm, to achieve a more accurate measurement.

5.5 Multi-Focus Image Fusion

To capture images of the canola plants, canola plants were directly placed underneath the Pi camera that fixed on the frame at a distance of 1,000 mm (see Figure 5-19). Each canola plant was recorded at 10fps for 3 seconds. The time between each changing the focal length is 10 seconds. Only frame number 20 of each video stream acquired from Pi camera was extracted. The reason is that the plant and the camera are needed to stable before capturing the images. Then, only the regions contain the plant in the selected images were cropped and used for multi-focus image fusion methods that will be introduced in this section.

To evaluate and verify the performance of the proposed approach, comprehensive experiments were conducted. The proposed method was compared with five other good multi-focus image fusion methods, such as the multi-scale weighted gradient based method (MWGF) [103], the DCT based Laplacian pyramid fusion technique (DCTLP) [104], the image fusion with guided filtering (GFF) [105], the gradient domain-based fusion combined with a pixel-based fusion (GDPB) [106], and the image matting (IM) based fusion algorithm [107]. The MWGF method is based on the image structure saliency and two scales to solve the fusion problems raised by anisotropic blur and miss-registration. The image structure saliency is used because it reflects the saliency of local edge and corner structures. The large-scale measure is used to reduce the impacts of anisotropic blur and miss-registration on the focused region detection, while the small-scale measure is used to determine the boundaries of the focused regions. The MWGF algorithm is available from https://github.com/lsauto/MWGF-Fusion. The DCTLP presents an image fusion method using discrete Cosine transform (DCT) based Laplacian pyramid (LP) in frequency domain. The authors in [104] imply that the higher level of pyramidal decomposition, the better quality of the fused image. The DCTLP algorithm is available at https://www.mathworks.com/ -matlabcentral/file-exchange/40302-dct-laplacian-pyramid-based-image-fusion. The GFF method is based on fusing two-scale layers through using a guided filter based weighted average method. This method measures pixel saliency and spatial consistency at two scales to construct weight maps for the fusion process. The GFF enables a fast and effective image fusion method for multi-focus, multi-spectral, multi-exposure, and multimodal images. The GFF algorithm is available at http://xudongkang.weebly.com/uploads/1/6/4/6/16465750/gff_1.0.7z. In gradient domain, authors in [106] present a multi-exposure and multi-focus image fusion (GDPB). This method fuses luminance and chrominance channels separately. The luminance channel is fused by using a wavelet-based gradient integration algorithm coupled with a Poisson Solver at each resolution to attenuate the artifacts. The chrominance channels are fused based on a weighted sum of the chrominance channels of the input images. This algorithm is available at https://www.mathworks.com/matlabcentral/fileexchange/48782-multi-exposure-and-multi-focus-image-fusion-in-gradient-domain?focused=6354746&tab=function. The image mating fusion (IM) method is based on of three steps: obtaining the focus information of each source image by morphological filtering, applying an image matting technique to achieve accurate focused regions of each source image, and combining these fused regions to construct the fused image. The IM algorithm is available at http://xudongkang.weebly.com/uploads/1/6/4/6/16465750/ifm.rar. These methods were downloaded and run on the same computer to compare to the proposed method.

All these methods used the same input images as the ones applied in the proposed technique. Ten multi-focuses image sequences were used in the experiments. Four of them are canola images captured by setting well-focused and manual changing focal length of the Pi camera; the others are selected from the general datasets used for many image fusion techniques. These general datasets are available at [108,109]. In the first four-canola database sets, three of them are artificial multi-focus images obtained by using LunaPic tool (https://www.lunapic.com), one of them is multi-focus images acquired directly from the Pi camera after cropping the region of interest. The proposed algorithm was developed to fit many types of multi-focus images captured by any digital camera or Pi camera.

The empirical parameters of the gradient domain fast guided filter and VS metrics were adjusted to obtain the best outputs. The parameters of the gradient domain fast guided filter (see Equation 3-46) consisted of a window size filter ($\zeta 1$), a small positive constant (Ɛ), subsampling of the fast guided filter (s), and a dynamic range of input images (L). The parameters of VS maps (see Equation 3-40), including alpha, beta, and gamma, were used to control visual saliency, gradient similarity, and color distortion measures, respectively. These empirical parameters of the gradient domain fast guided filters were experimentally set as s = 4, L = 9, and two pairs of $\zeta 1(1) = 4, Ɛ(1) = 1.0e - 6$ and $\zeta 1(2) = 4, Ɛ(2) = 1.0e - 6$ for optimizing base and detail weight maps. Other empirical parameters of VS maps were set as alpha = 1, beta = 0.89, and gamma = 0.31.

Surprisingly, when changing these parameters of the VS maps, such as, alpha = 0.31, beta = 1, and gamma = 0.31, the fused results had a similar quality to the first parameters' setting. It can be thus concluded that to obtain focused regions, both visual saliency and gradient magnitude similarity can be used as the main saliencies. In addition, the chrominance colors (M and N) also contributed to the quality of the fused results. For example, when increasing the parameters of M and N, the blurred regions appeared in the fused results. Figure 5-21 shown the outputs of the proposed algorithm, including visual saliency, gradient magnitude similarity, and chrominance colors. The red and green oval denotes the defocused region of the input image (Fig.5-21a).

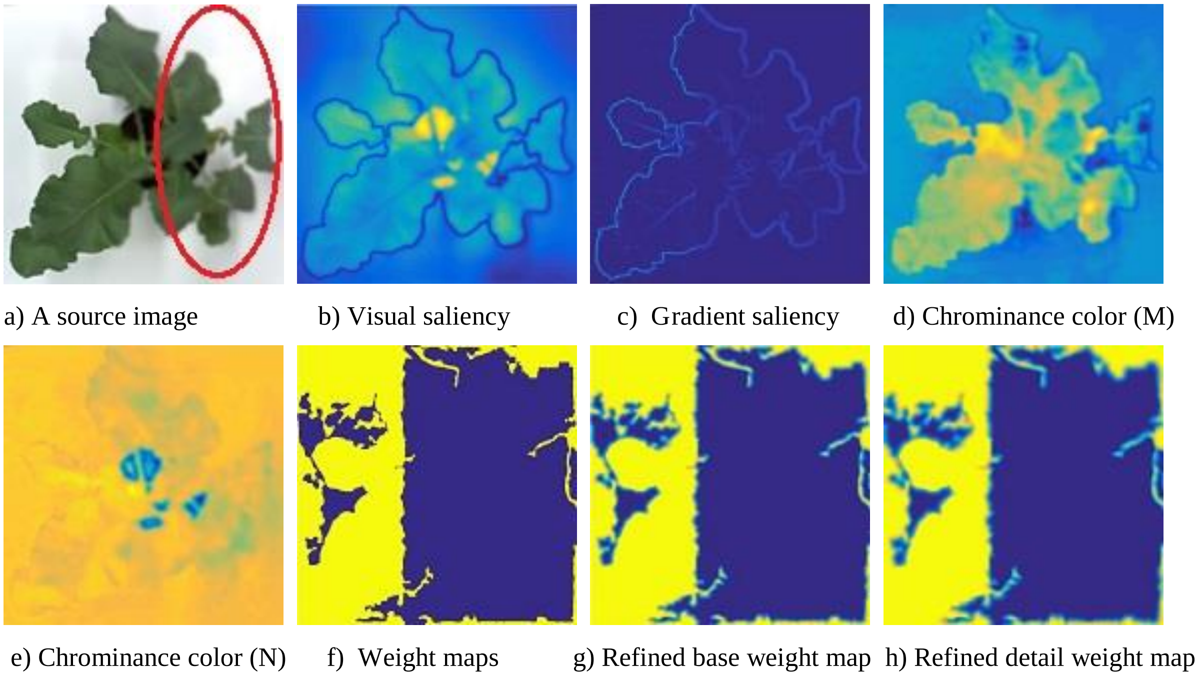
a) A source image
b) Visual saliency
c) Gradient saliency
d) Chrominance color (M)
e) Chrominance color (N)
f) Weight maps
g) Refined base weight map
h) Refined detail weight map

Figure 5-21. An example of a source image and its saliencies and weight maps

5.5.1 Comparisons with other Multi-Fusion Methods

In this section, a comprehensive assessment, including subjective and objective assessments, is used to evaluate the quality of fused images obtained from the proposed and other methods. Subjective assessments are methods to evaluate the quality of an image through many factors, including viewing distance, display device, lighting condition, vision ability, etc. However, subjective assessments are expensive and time consuming. Therefore, objective assessments – mathematical models - are designed to predict the quality of an image accurately and automatically.

For subjective or perceptual assessment, the comparisons of these fused images are shown from Figure 5-22 to Figure 5-26. The figures show the fused results of the “Canola 1,” “Canola 2,” “Canola 4,” “Books,” and “Rose flower” image sets. In these five examples, (a) and (b) are two source multi-focus images, and (c), (d), (e), (f), (g), and (h) are the fused images obtained with the MWGF, DCTLP, GFF, GDPB, IM, and the proposed methods, respectively. In almost all the cases, the MWGF method offers quite good fused images; however, sometimes it fails in dealing with the focused regions. For example, the blurred regions remain in the fused image as marked by the red circle in Figure 5-22(c). The DCTLP method offers fused images as good as the MWGF but causes blurring of the fused images in all five examples. The IM method also provides quite good results; however, ghost artifacts remain in the fused images, as shown in Figure 5-22(g), Figure 5-24(g), Figure 5-25(g), and Figure 5-26(g). Although the fused results of the GFF method reveals good visual effects at first glance, small blurred regions remained at the edge regions (the boundary between focused and defocused regions) of the fused results. This blurring of edge regions can be seen in the "rose flower" or "book" fused images in Figure 5-25(e) and Figure 5-26(e). The fused images of the GDPB method had unnatural colors and too much brightness. The fused results of the GDPB are also suffered from the ghost artifacts on the edge regions and the boundary between focused and defocused regions. It can be clearly seen that the proposed algorithm can obtain clearer fused images and better visual quality and contrast than other algorithms due to its combination of the gradient domain fast-guided filter and VS maps. The proposed algorithm offers fused images with fewer block artifacts and blurred edges.

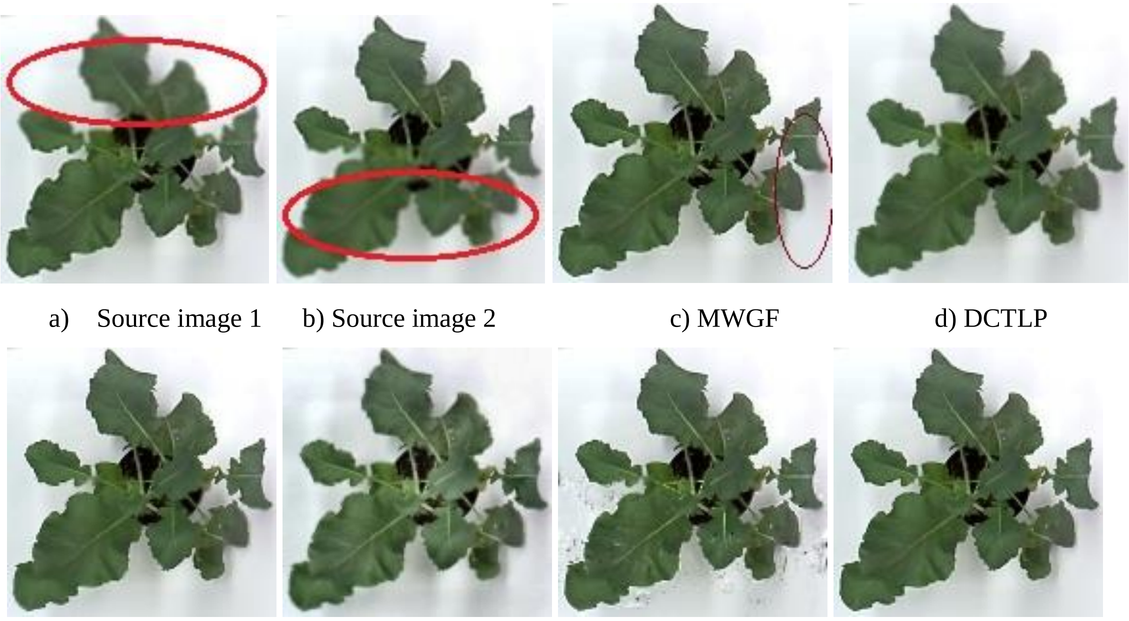
a) Source image 1 b) Source image 2 c) MWGF d) DCTLP

e) GFF f) GDPB g) IM h) the proposed method

Figure 5-22. Source images of "Canola 1" (a, b) and its fused images performed by [103], [104], [105], [106], [107] and the proposed algorithm.

a) Source image 1 b) Source image 2 c) MWGF d) DCTLP

e) GFF f) GDPB g) IM h) the proposed method

Figure 5-23. Source images of "Canola 2" (a, b) and its fused images performed by [103], [104], [105], [106], [107] and the proposed algorithm.

a) Source image 1 b) Source image 2 c) MWGF d) DCTLP

e) GFF f) GDPB g) IM h) the proposed method

Figure 5-24. Source images of "Canola 4" (a, b) and its fused images performed by [103], [104], [105], [106], [107] and the proposed algorithm.

a) Source image 1 b) Source image 2 c) MWGF d) DCTLP

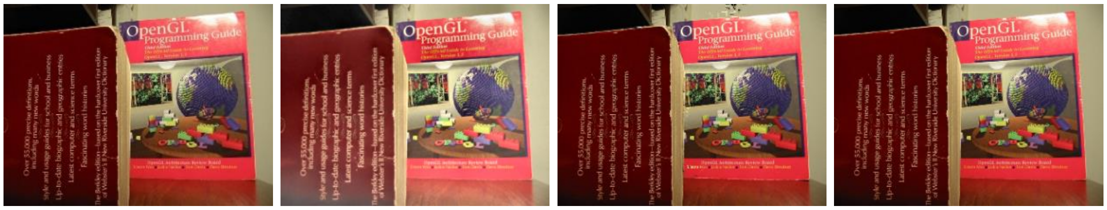

e) GFF f) GDPB g) IM h) the proposed method

Figure 5-25. Source images of “books” (a, b) and its fused images performed by [103], [104], [105], [106], [107] and the proposed algorithm.

a) Source image 1 b) Source image 2 c)MWGF d) DCTLP

e) GFF f) GDPB g) IM h) the proposed method

Figure 5-26. Source images of “a rose” (a, b) and its fused images performed by [103], [104], [105], [106], [107] and the proposed algorithm.

Besides on the subjective assessment, an objective assessment without the reference image was also conducted in this thesis. Three objective metrics, including mutual information (MI) [110], structural similarity (QY) [111], and an edge information-based metric Q(AB/F) [112] were used to evaluate the fusion performance of different multi-focus fusion methods.

The mutual information (MI) measures the amount of information transferred from both source images into the resulting fused image. It is calculated by

$$MI = 2\left(\frac{I(X,F)}{H(F)+H(X)} + \frac{I(Y,F)}{H(F)+H(Y)}\right) \tag{5.6}$$

where $I(X,F)$ is the mutual information of the input image X and fused image F. $I(Y,F)$ is the mutual information of the input image Y and fused image F. $H(X)$, $H(Y)$, and $H(F)$ denote the entropies of the input image X,Y, and used image F, respectively.

The structural similarity (QY) measures the corresponding regions in a reference original image *x* and the test image *y*. It is defined as

$$Q(x,y,f|w) = \begin{cases} \lambda(w)SSIM(x,f|w) + \left(1-\lambda(w)\right)SSIM(y,f|w), & for\ SSIM(x,y|w) \geq 0.75 \\ \max\{\mathrm{SSIM(x,f|w)}, \mathrm{SSIM(y,f|w)}\} & ,\mathrm{for}\ SSIM(x,y|w) < 0.75 \end{cases} \tag{5.7}$$

where $\lambda(w) = \frac{s(x|w)}{s(X|W)+s(y|w)}$ is the local weight, and $s(x|w)$ and $s(y|w)$ are the variances of w_x and w_y, respectively.

The edge information based metric $Q^{AB/F}$ measures the amount of edge information that is transferred from input images to the fused image. For the fusion of source images A and B resulting in a fused image F, gradient strength $g(n,m)$ and orientation $\alpha(n,m)$ are extracted at each pixel (n,m) from an input image, as given by

$$g_A(n,m) = \sqrt{s_A^x(n,m)^2 + s_A^y(n,m)^2} \tag{5.8}$$

$$\alpha_A = tan^{-1}\left(\frac{s_A^y(n,m)}{s_A^x(n,m)}\right) \tag{5.9}$$

where $s_A^x(n,m)$ and $s_A^y(n,m)$ are the output of the horizontal and vertical Sobel templates centred on pixel $p_A(n,m)$ and convolved with the corresponding pixels of input image A.

The relative strength and orientation values of $G^{AF}(n,m)$ and $A^{AF}(n,m)$ of the input image A with respect to the fused image F are calculated by

$$G^{AF}(n,m) = \begin{cases} \frac{g_{F(n,m)}}{g_{A(n,m)}}\ if\ g_{A(n,m)} > g_{F(n,m)} \\ \frac{g_{A(n,m)}}{g_{F(n,m)}}, \qquad otherwise \end{cases} \tag{5.10}$$

$$A^{AF}(n,m) = 1 - \frac{|\alpha_A(n,m) - \alpha_F(n,m)|}{\pi/2} \tag{5.11}$$

From these values, the edge strength and orientation values are derived, as given by

$$Q_g^{AF}(n,m) = \frac{\Gamma_g}{1+e^{K_g(G^{AF}(n,m)-\sigma_g)}} \tag{5.12}$$

$$Q_{\alpha}^{AF}(n,m) = \frac{\Gamma_{\alpha}}{1+e^{K_{\alpha}(A^{AF}(n,m)-\sigma_{\alpha})}} \tag{5.13}$$

$Q_g^{AF}(n,m)$ and $Q_{\alpha}^{AF}(n,m)$ model information loss between the input image A and the fused image F. The constants Γ_g, K_g, σ_g and Γ_{α}, $K_{\alpha}, \sigma_{\alpha}$ determine the exact shape of the sigmoid functions used to form the edge strength and orientation preservation values (Eq. 5.12 and Eq.5.13). Edge information preservation values are formed by

$$Q^{AF}(n,m) = Q_g^{AF}(n,m)Q_{\alpha}^{AF}(n,m) \tag{5.14}$$

with $0 \leq Q^{AF}(n,m) \leq 1$. The higher value of $Q^{AF}(n,m)$, the less loss of information of the fused image.

The fusion performance $Q^{AB/F}$ is evaluated as a sum of local information preservations estimates between each of the input images and fused image, is defined as

$$Q^{AB/F} = \frac{\sum_{n=1}^{N} \sum_{m=1}^{M} Q^{AF}(n,m)w^{A}(n,m)+Q^{BF}(n,m)w^{B}(n,m))}{\sum_{j=1}^{N} \sum_{j=1}^{M}(w^{A}(i,j)+w^{B}(i,j))} \tag{5.15}$$

where $Q^{AF}(n,m)$ and $Q^{BF}(n,m)$ are edge information preservation values, weighted by $w^{A}(n,m)$ and $w^{B}(n,m)$, respectively.

Table 5-10 illustrates the quantitative assessment values of five different multi-focus fusion methods and the proposed method. The larger values indicated by the metrics, the better the image quality. The values shown in bold represent the highest performance. From Table 5-10, it can be seen that the proposed method produces the highest quality scores for all three-objective metrics, except for QY with “Canola 2” datasets and QAB/F with “Book” datasets. These large quality scores suggest that the proposed method performed well and is both stable and reliable. Overall, it can be concluded that, when compared with previous multi-focus fusion methods, the proposed method performs competitively, both in visual perception and objective metrics.

Table 5-10. Comparisons of the proposed method with other methods

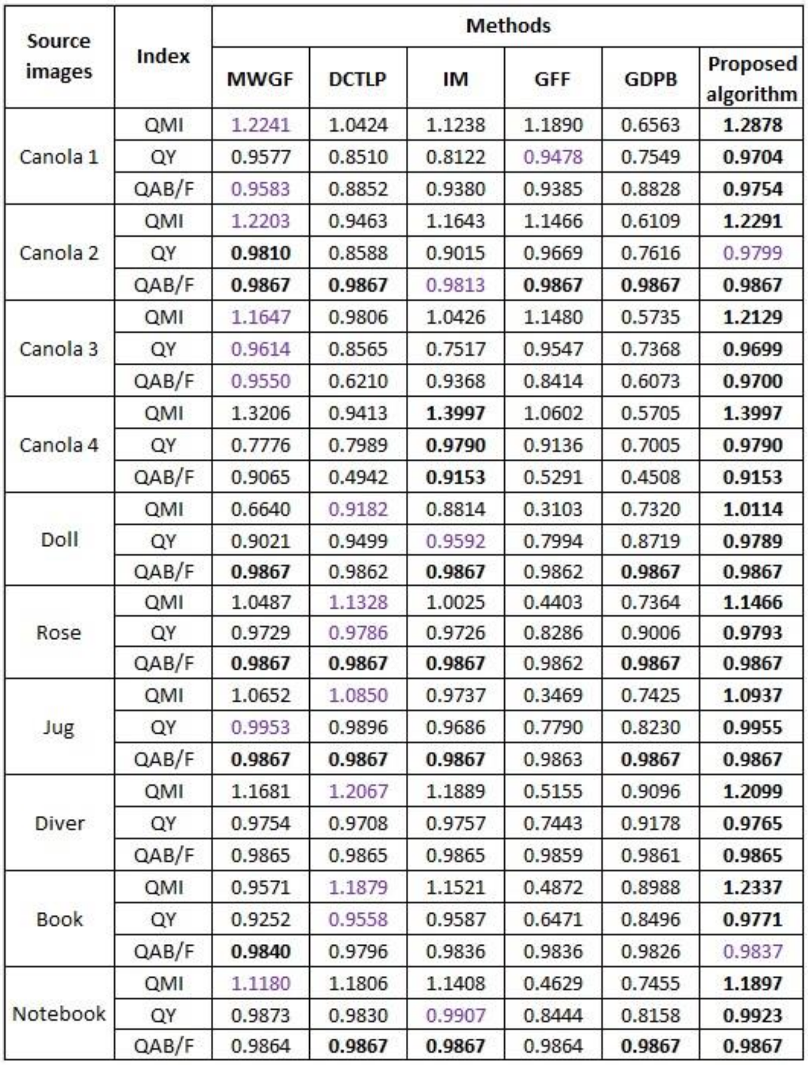

Source images	Index	Methods					
		MWGF	DCTLP	IM	GFF	GDPB	Proposed algorithm
Canola 1	QMI	1.2241	1.0424	1.1238	1.1890	0.6563	**1.2878**
	QY	0.9577	0.8510	0.8122	0.9478	0.7549	**0.9704**
	QAB/F	0.9583	0.8852	0.9380	0.9385	0.8828	**0.9754**
Canola 2	QMI	1.2203	0.9463	1.1643	1.1466	0.6109	**1.2291**
	QY	**0.9810**	0.8588	0.9015	0.9669	0.7616	0.9799
	QAB/F	**0.9867**	**0.9867**	0.9813	**0.9867**	**0.9867**	**0.9867**
Canola 3	QMI	1.1647	0.9806	1.0426	1.1480	0.5735	**1.2129**
	QY	0.9614	0.8565	0.7517	0.9547	0.7368	**0.9699**
	QAB/F	0.9550	0.6210	0.9368	0.8414	0.6073	**0.9700**
Canola 4	QMI	1.3206	0.9413	**1.3997**	1.0602	0.5705	**1.3997**
	QY	0.7776	0.7989	**0.9790**	0.9136	0.7005	**0.9790**
	QAB/F	0.9065	0.4942	**0.9153**	0.5291	0.4508	**0.9153**
Doll	QMI	0.6640	0.9182	0.8814	0.3103	0.7320	**1.0114**
	QY	0.9021	0.9499	0.9592	0.7994	0.8719	**0.9789**
	QAB/F	**0.9867**	0.9862	**0.9867**	0.9862	**0.9867**	**0.9867**
Rose	QMI	1.0487	1.1328	1.0025	0.4403	0.7364	**1.1466**
	QY	0.9729	0.9786	0.9726	0.8286	0.9006	**0.9793**
	QAB/F	**0.9867**	**0.9867**	**0.9867**	0.9862	**0.9867**	**0.9867**
Jug	QMI	1.0652	1.0850	0.9737	0.3469	0.7425	**1.0937**
	QY	0.9953	0.9896	0.9686	0.7790	0.8230	**0.9955**
	QAB/F	**0.9867**	**0.9867**	**0.9867**	0.9863	**0.9867**	**0.9867**
Diver	QMI	1.1681	1.2067	1.1889	0.5155	0.9096	**1.2099**
	QY	0.9754	0.9708	0.9757	0.7443	0.9178	**0.9765**
	QAB/F	0.9865	0.9865	0.9865	0.9859	0.9861	**0.9865**
Book	QMI	0.9571	1.1879	1.1521	0.4872	0.8988	**1.2337**
	QY	0.9252	0.9558	0.9587	0.6471	0.8496	**0.9771**
	QAB/F	**0.9840**	0.9796	0.9836	0.9836	0.9826	0.9837
Notebook	QMI	1.1180	1.1806	1.1408	0.4629	0.7455	**1.1897**
	QY	0.9873	0.9830	0.9907	0.8444	0.8158	**0.9923**
	QAB/F	0.9864	**0.9867**	**0.9867**	0.9864	**0.9867**	**0.9867**

5.5.2 Comparisons in Computation Efficiency

Computational cost is also a key metric for fusion performance assessment. In the experiments, all the testing fusion methods were implemented in MATLAB R2016b on a computer with a 2.9 GHz CPU and 8.0 GB RAM. Two types of source images, one from our laboratory and the other from the general datasets, were used for many image fusion techniques. To compare the computation efficiency of the proposed method with other fusion methods, these source images with these sizes were used: 1024 x 768, 800x800, 768 x768, 768 x 512, 772 x 824, 720 x 644, and 520 x 520. Table 5-12 illustrates the average running time of different multi-focus image fusion methods. The smaller values of the computational time indicate the better fusion performance. The values shown in bold, purple, and green colors in Table 5-11represent the best, the second-best and the third-best performance. As has been pointed out, in some cases, the proposed method requires less running time than that of the MWGF, IM, GFF, and GDPB methods but only slightly more than that of the DCTLP. The reason is that the proposed method adopts the gradient domain fast-guided filter.

Table 5-11. Computational time of different multi-focus fusion methods

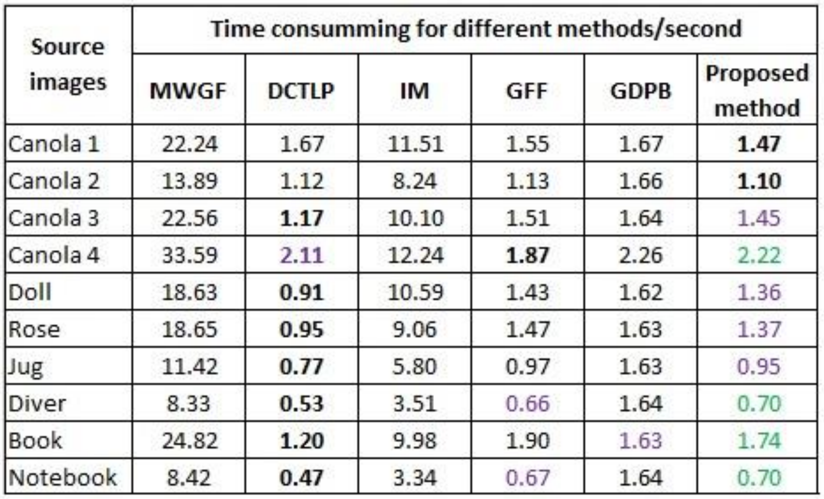

Source images	**Time consumming for different methods/second**					
	MWGF	**DCTLP**	**IM**	**GFF**	**GDPB**	**Proposed method**
Canola 1	22.24	1.67	11.51	1.55	1.67	**1.47**
Canola 2	13.89	1.12	8.24	1.13	1.66	**1.10**
Canola 3	22.56	**1.17**	10.10	1.51	1.64	1.45
Canola 4	33.59	2.11	12.24	**1.87**	2.26	2.22
Doll	18.63	**0.91**	10.59	1.43	1.62	1.36
Rose	18.65	**0.95**	9.06	1.47	1.63	1.37
Jug	11.42	**0.77**	5.80	0.97	1.63	0.95
Diver	8.33	**0.53**	3.51	0.66	1.64	0.70
Book	24.82	**1.20**	9.98	1.90	1.63	1.74
Notebook	8.42	**0.47**	3.34	0.67	1.64	0.70

5.5.3 Limitations

The fused results of the proposed method remain as small-blurred regions in the boundaries between the focused and defocused regions. More morphological techniques are required to deal with this problem.

CHAPTER 6 – CONCLUSIONS AND FUTURE WORK

6.1 Conclusions

This thesis shows that the goals of this research are achieved. The thesis presents contributions to the canola plant phenotyping and image processing areas, including counting canola branches and seedpods in indoor environment, estimating plant height, and fusing multi-focus images. Tools developed in the thesis consisted of a low-cost depth plant phenotyping mobile device, a plant traits measuring tool, and an image fusion tool. The low-cost depth mobile platform was built from a low-cost depth camera (an Argos3D P100), a low-cost Pi camera, and a low-cost mini-computer (a Raspberry Pi 3). This mobile platform can help plant researchers to capture canola plant images in terms of 2D and 3D across environments. Once the mobile platform was built, captured images are used to measure plant traits, such as the number of canola branches, canola seedpods, and plant height. This study also developed image fusion tools to support plant researchers in improving the description and quality of 2D images for further research, such as fusing multi-focus images to obtain clear focused results and using a low-cost camera instead of an expensive camera.

The method to count canola branches uses the Argos3D P100 depth camera instead of the Kinect V2 camera to acquire 2D or 3D images with lower background noise. This depth camera performs very fast, up to 160fps even in low ambient illumination. The algorithm of the counting canola branches was quite simple. First, the 2D or 3D image is converted to grayscale before a Gaussian low-pass filter was applied to smooth the input image. Then, the ROI containing the branches and stem are obtained, before a fast-marching algorithm was applied to identify the skeleton of the ROI. Finally, the end-points of the skeleton or the number of branches and stems are retrieved. However, the results remain inaccurate when the canola branches are overlapping. To deal with the obstacle of overlapped branches that cause error, a horizontal resizing technique was developed. The accuracy of the counting canola branches then improved and achieved up to 95.6%. Based on the experimental results, it can be stated that using a low-cost depth camera (Argos3D P100) is reliable, accurate, and fast in detection and counting canola branches under indoor environments.

To count the canola seedpods in color images, a digital camera was used. Then, the Frangi vesselness filter was deployed to remove the background and noise from these images. Next, the skeleton of the canola was extracted and an algorithm for finding end-points was deployed. The number of seedpods was quite similar to the number of end-points of the skeleton. Finally, a refined technique that eliminated spikes was developed to offer better accurate results. The accuracy of the algorithm for counting canola seedpods reached 96.8%. It can thus be clearly seen that the counting of canola seedpods is an outstanding method to obtain accuracy, stability, and reliability.

Besides counting canola branches and seedpods, the height of plants was measured using a helpful measurement tool. By using a low-cost depth camera, Argos3D P100, the plant height of each canola plant is easily measured with high speed and accuracy. First, the grayscale information of the canola plant is obtained. Then, the distance information between the depth camera and the plant was directly extracted from the grayscale information. Finally, the plant height is estimated based on this information and the distance between the depth camera and ground truth. From the experiment's results, it is evident that the plant height measurement method offers a high-speed measurement with high accuracy, up to 91 % on an average.

To improve the description and quality image, especially images acquired from the digital camera or the Pi camera for counting seedpods or further study, an image fusion method is required. A novel multi-focus image fusion method was proposed with the combination of the VS maps and gradient domain fast-guided filter. In the proposed algorithm, the VS maps are first deployed to obtain visual saliency, gradient magnitude similarity saliency, and chrominance saliency (or color distortions). Then, the initial weight map is constructed with a mix of three metrics. Next, the final-decision weight maps are obtained by optimizing the initial weight map with a gradient domain fast-guided filter at two components. Finally, the fused results are retrieved by the combination of two-component weight maps and two-component source images that present large-scale and small-scale variations in intensity. The proposed method was compared with five proper representative fusion methods, both in subjective and objective evaluations. Based on the experiment's results, the proposed fusion method presents a competitive performance with or even outperforms some state-of-the-art methods. The proposed method's success was largely based on the VS maps' measure and gradient domain fast-guided filter. The proposed method can use any digital images captured by either a high-end or low-end camera, especially the low cost Pi camera. This fusion method can be used to improve the results of counting canola seedpods from the images captured by low-cost cameras.

6.2 Future Work

To further enhance the performance of the proposed method, future research directions will focus on generating more accurate canola counts and extend the image-fusion method to other fields. Although the counting of canola branches reveals quite good results, some limitations such as the strong ambient light, overlapping branches and outdoor environment were obstacles. To deal with these drawbacks, some ideas can be implemented, such as using another higher depth camera and enhancing depth images by fusing depth and color images. Some options for higher depth cameras are Argos3D P3xx cameras. Argos3D P330 is the current highest version equipped with a high-resolution depth sensor (352x287 pixels) combined with a 2D CMOS sensor. This depth camera is less sensitive to strong ambient light and offers a Gigabit Ethernet interface so that data streams can be transferred faster to the host. One interesting approach that might solve the problem of overlapping branches is to use a technique of enhanced depth images. This technique suggests that the current 3D point cloud resolution acquired from the Argos3D P100 can be enhanced by fusing depth and color images. From the enhanced depth images, canola branches can be more easily identified and are more accurate than the current method. In addition, counting canola branches cannot be used for outdoor scenario due to the complex structure of the canola plants in the field. For outdoor environment, other applications of this depth camera can be pursued, such as detecting canola plants, segmenting individual leave, and measuring leaf area index.

One limitation of the proposed method for counting canola seedpods is the deployment in the outdoor environment. Due to overlapping or twisted canola branches and seedpods in the field, counting seedpods may not be possible. The solution to deal with this can be started from the flowering stage, in which canola flowers can be counted. Further study to count the number of flowers can be pursued to address this challenge.

Other limitations of the proposed multi-focus image fusion, such as small-blurred regions in the boundaries between the focused and defocused regions and the computational cost, are worthwhile to investigate. Morphological techniques and optimizing multi-focus fusion algorithm are also recommended for further study. Finally, 3D modelling from enhancing depth images and fusion techniques should be investigated for their application in plant phenotyping and other fields, such as remote sensing and medicine.

References

[1.] Food and Agriculture Organization of the United Nations, 2017. *The future of food and agriculture – Trends and challenges*. Retrieved on February 28, 2018 from http://www.fao.org/3/a-i6583e.pdf

[2.] Luc Casséus (2009). *Canola: a Canadian success story*. Canadian Agriculture at a Glance. Component of Statistics Canada Catalogue no. 96-325-X. Retrieved on February 28, 2018 from https://www.statcan.gc.ca/pub/96-325-x/2007000/article/10778-eng.pdf

[3.] Census of Agriculture, 2016. Retrieved on February 28, 2018 from https://www.statcan.gc.ca/daily-quotidien/170510/dq170510a-eng.pdf

[4.] Canadian Canola Growers Association, 2016. Retrieved on February 28, 2018 from http://www.ccga.ca/policy/Documents/Canola%20Information%20Booklet%20-%20Web.pdf .

[5.] Phillips, R. L. (2010). Mobilizing science to break yield barriers. *Crop Science, 50* (Supplement_1), S-99.

[6.] Li, L., Zhang, Q., & Huang, D. (2014). A review of imaging techniques for plant phenotyping. *Sensors*, *14*(11), 20078-20111.

[7.] Fiorani, F., & Schurr, U. (2013). Future scenarios for plant phenotyping. *Annual review of plant biology*, *64*, 267-291.

[8.] Furbank, R. T., & Tester, M. (2011). Phenomics – technologies to relieve the phenotyping bottleneck. *Trends in Plant Science, 16*(12), 635-644. doi:10.1016/j.tplants.2011.09.005

[9.] Dornbusch, T., Lorrain, S., Kuznetsov, D., Fortier, A., Liechti, R., Xenarios, I., & Fankhauser, C. (2012). Measuring the diurnal pattern of leaf hyponasty and growth in Arabidopsis–a novel phenotyping approach using laser scanning. *Functional Plant Biology*, *39*(11), 860-869.

[10.] Chen, D., Neumann, K., Friedel, S., Kilian, B., Chen, M., Altmann, T., & Klukas, C. (2014). Dissecting the Phenotypic Components of Crop Plant Growth and Drought Responses Based on High-Throughput Image Analysis. *The Plant Cell Online, 26*(12), 4636-4655. doi:10.1105/tpc.114.129601

[11.] Kjaer, K. H., & Ottosen, C. O. (2015). 3D laser triangulation for plant phenotyping in challenging environments. *Sensors*, *15*(6), 13533-13547.

[12.] Eitel, J. U., Magney, T. S., Vierling, L. A., Brown, T. T., & Huggins, D. R. (2014). LiDAR based biomass and crop nitrogen estimates for rapid, non-destructive assessment of wheat nitrogen status. *Field Crops Research*, *159,* 21-32.

[13.] Tanger, P., Klassen, S., Mojica, J. P., Lovell, J. T., Moyers, B. T., Baraoidan, M., ... & Leung, H. (2017). Field-based high throughput phenotyping rapidly identifies genomic regions controlling yield components in rice. *Scientific Reports*, *7*, 42839.

[14.] Moshou, D., Bravo, C., Oberti, R., West, J., Bodria, L., McCartney, A., & Ramon, H. (2005). Plant disease detection based on data fusion of hyper-spectral and multi-spectral fluorescence imaging using Kohonen maps. *Real-Time Imaging, 11*(2), 75-83. doi:10.1016/j.rti.2005.03.003

[15.] Tsaftaris, S. A., & Noutsos, C. (2009). Plant Phenotyping with Low Cost Digital Cameras and Image Analytics. *Information Technologies in Environmental Engineering*, 238-251. doi:10.1007/978-3-540-88351-7_18

[16.] Gai, J., Tang, L., & Steward, B.L. (2015). Plant Recognition through the Fusion of 2D and 3D Images for Robotic Weeding. *2015 ASABE International Meeting*. doi:10.13031/aim.20152181371

[17.] Thoren, D., & Schmidhalter, U. (2009). Nitrogen status and biomass determination of oilseed rape by laser-induced chlorophyll fluorescence. *European Journal of Agronomy, 30*(3), 238-242. doi:10.1016/j.eja.2008.12.001

[18.] Xiong, X., Yu, L., Yang, W., Liu, M., Jiang, N., Wu, D., … Liu, Q. (2017). A high-throughput stereo-imaging system for quantifying rape leaf traits during the seedling stage. *Plant Methods, 13*(1). doi:10.1186/s13007-017-0157-7

[19.] Baranowski, P., Jedryczka, M., Mazurek, W., Babula-Skowronska, D., Siedliska, A., & Kaczmarek, J. (2015). Hyperspectral and Thermal Imaging of Oilseed Rape (Brassica napus) Response to Fungal Species of the Genus Alternaria. *PLOS ONE, 10*(3), e0122913. doi:10.1371/journal.pone.0122913

[20.] Singh, A., Ganapathysubramanian, B., Singh, A. K., & Sarkar, S. (2016). Machine Learning for High-Throughput Stress Phenotyping in Plants. *Trends in Plant Science, 21*(2), 110-124. doi:10.1016/j.tplants.2015.10.015

[21.] Dambreville, A., Griolet, M., Rolland, G., Dauzat, M., Bédiée, A., Balsera, C., . . . Granier, C. (2017). Phenotyping oilseed rape growth-related traits and their responses to water deficit: the disturbing pot size effect. *Functional Plant Biology, 44* (1), 35-45. doi: 10.1071/ft16036

[22.] Busemeyer, L., Mentrup, D., Möller, K., Wunder, E., Alheit, K., Hahn, V., ... & Rahe, F. (2013). Breedvision—A multi-sensor platform for non-destructive field-based phenotyping in plant breeding. *Sensors, 13*(3), 2830-2847.

[23.] Van der Heijden, G., Song, Y., Horgan, G., Polder, G., Dieleman, A., Bink, M., … Glasbey, C. (2012). SPICY: towards automated phenotyping of large pepper plants in the greenhouse. *Functional Plant Biology, 39*(11), 870. doi:10.1071/fp12019

[24.] Reis, R.J. (2013). Evaluation of Phenotyping Methods for Maize. M.Sc. Thesis, University of Illinois at Urbana-Champaign, Urbana, Illinois.

[25.] Yahata, S., Onishi, T., Yamaguchi, K., Ozawa, S., Kitazono, J., Ohkawa, T., . . . Tsuji, H. (2017). A hybrid machine learning approach to automatic plant phenotyping for smart agriculture. *2017 International Joint Conference on Neural Networks (IJCNN)*. doi:10.1109/ijcnn.2017.7966067

[26.] Gürel, C., Zadeh, M. H. G., & Erden, A. (2016). Rose Stem Branch Point Detection And Cutting Point Location for Rose Harvesting Robot. *The 17th International Conference on Machine Design and Production, UMTIK 2016*.

[27.] Großkinsky D. K., Svensgaard J., Christensen S., Roitsch T. (2015). Plant phenomics and the need for physiological phenotyping across scales to narrow the genotype-to-phenotype knowledge gap. *J. Exp. Bot.* 66, 5429–5440. 10.1093/jxb/erv345.

[28.] The Transportation Energy Resources from Renewable Agriculture Phenotyping Reference Platform (TERRA-REF), Arizona. http://terraref.org/, accessed on September 20, 2017

[29.] Australian plant phenomics facility. Available online: http://www.plantphenomics.org.au/, accessed on September 20, 2017

[30.] Rothamsted Research, UK. https://www.rothamsted.ac.uk/field-scanalyzer, accessed on September 20, 2017

[31.] Rahaman, M. M., Chen, D., Gillani, Z., Klukas, C., & Chen, M. (2015). Advanced phenotyping and phenotype data analysis for the study of plant growth and development. *Frontiers in Plant Science*, 6, 619. doi: 10.3389/fpls.2015.00619

[32.] Udayakumar N (2014). Visible Light Imaging. In: Manickavasagan A., Jayasuriya H. (eds) *Imaging with Electromagnetic Spectrum*. Springer, Berlin, Heidelberg. doi: 10.1007/978-3-642-54888-8_5

[33.] Siddiqui, Z. S., Cho, J., Park, S., Kwon, T., Lee, G., Jeong, M., … Park, S. (2014). Phenotyping of rice in salt stress environment using high-throughput infrared imaging. *Acta Botanica Croatica, 73*(1). doi:10.2478/botcro-2013-0027

[34.] Virlet, N., Lebourgeois, V., Martinez, S., Costes, E., Labbe, S., & Regnard, J. (2014). Stress indicators based on airborne thermal imagery for field phenotyping a heterogeneous tree population for response to water constraints. *Journal of Experimental Botany, 65*(18), 5429-5442. doi:10.1093/jxb/eru309

[35.] Jones Hamlyn G., Serraj Rachid, Loveys Brian R., Xiong Lizhong, Wheaton Ashley, Price Adam H (2009). Thermal infrared imaging of crop canopies for the remote diagnosis and quantification of plant responses to water stress in the field. *Functional Plant Biology 36*, 978-989. doi:10.1071/FP09123

[36.] Martynenko, A., Shotton, K., Astatkie, T., Petrash, G., Fowler, C., Neily, W., & Critchley, A. T. (2016). Thermal imaging of soybean response to drought stress: the effect of Ascophyllum nodosum seaweed extract. *SpringerPlus, 5*(1). doi:10.1186/s40064-016-3019-2

[37.] Grant, O. M., Davies, M. J., James, C. M., Johnson, A. W., Leinonen, I., & Simpson, D. W. (2012). Thermal imaging and carbon isotope composition indicate variation amongst strawberry (Fragaria×ananassa) cultivars in stomatal conductance and water use efficiency. *Environmental and Experimental Botany, 76*, 7-15. doi:10.1016/j.envexpbot.2011.09.013

[38.] Costa, J. M., Grant, O. M., & Chaves, M. M. (2013). Thermography to explore plant–environment interactions. *Journal of Experimental Botany, 64*(13), 3937-3949. doi:10.1093/jxb/ert029

[39.] Munns R., James R. A., Sirault X. R., Furbank R. T., Jones H. G. (2010). New phenotyping methods for screening wheat and barley for beneficial responses to water deficit. *J. Exp. Bot.* 61 3499–3507. 10.1093/jxb/erq199

[40.] Jansen, M., Gilmer, F., Biskup, B., Nagel, K. A., Rascher, U., Fischbach, A., … Walter, A. (2009). Simultaneous phenotyping of leaf growth and chlorophyll fluorescence via GROWSCREEN FLUORO allows detection of stress tolerance in Arabidopsis thaliana and other rosette plants. *Functional Plant Biology, 36*(11), 902. doi:10.1071/fp09095

[41.] Scholes, J. D., and S. A. Rolfe. 2009. Chlorophyll fluorescence imaging as tool for understanding the impact of fungal diseases on plant performance: a phenomics perspective. *Functional Plant Biology*, 36(10-11):880-892

[42.] Mutka, A. M., & Bart, R. S. (2014). Image-based phenotyping of plant disease symptoms. *Frontiers in Plant Science, 5*, 734. http://doi.org/10.3389/fpls.2014.00734

[43.] Sindhuja Sankaran, Ashish Mishra, Reza Ehsani, & Cristina Davis (2010). Review: A review of advanced techniques for detecting plant diseases. *Comput. Electron. Agric.* 72, 1 , 1-13. doi: 10.1016/j.compag.2010.02.007

[44.] Humplík, J. F., Lazár, D., Husičková, A., & Spíchal, L. (2015). Automated phenotyping of plant shoots using imaging methods for analysis of plant stress responses – a review. *Plant Methods, 11*(1). doi:10.1186/s13007-015-0072-8

[45.] Cabrera-Bosquet, L., Molero, G., Stellacci, A., Bort, J., Nogués, S., & Araus, J. (2011). NDVI as a potential tool for predicting biomass, plant nitrogen content and growth in wheat genotypes subjected to different water and nitrogen conditions. *Cereal Research Communications, 39*(1), 147-159. doi:10.1556/crc.39.2011.1.15

[46.] Petrozza, A., Santaniello, A., Summerer, S., Di Tommaso, G., Di Tommaso, D., Paparelli, E., … Cellini, F. (2014). Physiological responses to Megafol® treatments in tomato plants under drought stress: A phenomic and molecular approach. *Scientia Horticulturae, 174*, 185-192. doi:10.1016/j.scienta.2014.05.023

[47.] González-Flor, C., Serrano, L., Gorchs, G., & Pons, J. M. (2014). Assessment of Grape Yield and Composition Using Reflectance-Based Indices in Rainfed Vineyards. *Agronomy Journal*, 106(4), 1309. doi:10.2134/agronj13.0422

[48.] Schweiger, A. K., Schütz, M., Risch, A. C., Kneubühler, M., Haller, R., & Schaepman, M. E. (2016). How to predict plant functional types using imaging spectroscopy: linking vegetation community traits, plant functional types and spectral response. *Methods in Ecology and Evolution, 8*(1), 86-95. doi:10.1111/2041-210x.12642

[49.] Nguyen, T. T., Slaughter, D. C., Maloof, J. N., & Sinha, N. (2016). Plant phenotyping using multi-view stereo vision with structured lights. *Autonomous Air and Ground Sensing Systems for Agricultural Optimization and Phenotyping*. doi:10.1117/12.2229513

[50.] P. Sodhi, S. Vijayarangan, and D. Wettergreen (2017). In-field Segmentation and dentification of Plant Structures using 3D Imaging. *IEEE/RSJ International Conference on Intelligent Robots and Systems.*

[51.] Paulus, S., Dupuis, J., Riedel, S., & Kuhlmann, H. (2014a). Automated Analysis of Barley Organs Using 3D Laser Scanning: An Approach for High Throughput Phenotyping. *Sensors* (Basel, Switzerland), 14(7), 12670–12686. http://doi.org/10.3390/s140712670

[52.] Guo, Q., Wu, F., Pang, S., Zhao, X., Chen, L., Liu, J., … Chu, C. (2017). Crop 3D - a LiDAR based platform for 3D high-throughput crop phenotyping. *Science China Life Sciences*. doi:10.1007/s11427-017-9056-0

[53.] Friedli, M., Kirchgessner, N., Grieder, C., Liebisch, F., Mannale, M., & Walter, A. (2016). Terrestrial 3D laser scanning to track the increase in canopy height of both monocot and dicot crop species under field conditions. *Plant Methods, 12*.

[54.] Nie, S., Wang, C., Dong, P., Xi, X., Luo, S., & Zhou, H. (2016). Estimating Leaf Area Index of Maize Using Airborne Discrete-Return LiDAR Data. *IEEE Journal of Selected Topics in Applied Earth Observations and Remote Sensing, 9*(7), 3259-3266. doi:10.1109/jstars.2016.2554619

[55.] Li, A., Dhakal, S., Glenn, N., Spaete, L., Shinneman, D., Pilliod, D., … McIlroy, S. (2017). Lidar Aboveground Vegetation Biomass Estimates in Shrublands: Prediction, Uncertainties and Application to Coarser Scales. *Remote Sensing, 9*(9), 903. doi:10.3390/rs9090903

[56.] Seidel, D., Beyer, F., Hertel, D., Fleck, S., & Leuschner, C. (2011). 3D-laser scanning: A non-destructive method for studying above- ground biomass and growth of juvenile trees. *Agricultural and Forest Meteorology, 151*(10), 1305-1311. doi:10.1016/j.agrformet.2011.05.013

[57.] Paulus, S., Eichert, T., Goldbach, H., & Kuhlmann, H. (2014c). Limits of Active Laser Triangulation as an Instrument for High Precision Plant Imaging. *Sensors*, 14(2), 2489-2509. doi:10.3390/s140202489

[58.] Nguyen, T. T., Slaughter, D. C., Townsley, B., Carriedo, L., Maloof, J. N., & Sinha, N. (2016b). Comparison of structure-from-motion and stereo vision techniques for full in-field 3D reconstruction and phenotyping of plants: An investigation in sunflower. *Proceedings of the ASABE Annual International Meeting*. Orlando, Florida, USA.

[59.] Vázquez-Arellano, M., Griepentrog, H., Reiser, D., & Paraforos, D. (2016). 3-D Imaging Systems for Agricultural Applications—A Review. *Sensors, 16*(5), 618. doi:10.3390/s16050618

[60.] Klose R, Penlington J, Ruckelshausen A. (2009).Usability study of 3D time-of-flight cameras for automatic plant phenotyping. *Bornimer Agrartech. Ber. 69*:93–105

[61.] Alenya, G., Dellen, B., & Torras, C. (2011). 3D modelling of leaves from color and ToF data for robotized plant measuring. *2011 IEEE International Conference on Robotics and Automation*. doi:10.1109/icra.2011.5980092

[62.] Nakarmi, A., & Tang, L. (2012). Automatic inter-plant spacing sensing at early growth stages using a 3D vision sensor. *Computers and Electronics in Agriculture, 82*, 23-31. doi:10.1016/j.compag.2011.12.011

[63.] Fernández, R., Salinas, C., Montes, H., & Sarria, J. (2014). Multisensory System for Fruit Harvesting Robots. Experimental Testing in Natural Scenarios and with Different Kinds of Crops. *Sensors, 14*(12), 23885-23904. doi:10.3390/s141223885

[64.] Paulus, S., Behmann, J., Mahlein, A., Plümer, L., & Kuhlmann, H. (2014b). Low-Cost 3D Systems: Suitable Tools for Plant Phenotyping. *Sensors, 14*(2), 3001-3018. doi:10.3390/s140203001

[65.] Li, D., Xu, L., Tan, C., Goodman, E., Fu, D., & Xin, L. (2015). Digitization and Visualization of Greenhouse Tomato Plants in Indoor Environments. *Sensors, 15*(2), 4019-4051. doi:10.3390/s150204019

[66.] Yamamoto, S., Hayashi, S., Tsubota, S. (2015). Growth Measurement of a Community of Strawberries Using Three-Dimensional Sensor. *Environment Control in Biology, 53*(2), 49-53. doi:10.2525/ecb.53.49

[67.] Tisné, S., Serrand, Y., Bach, L., Gilbault, E., Ben Ameur, R., Balasse, H., … Loudet, O. (2013). Phenoscope: an automated large-scale phenotyping platform offering high spatial homogeneity. *The Plant Journal, 74*(3), 534-544. doi:10.1111/tpj.12131

[68.] Flood, P. J., Kruijer, W., Schnabel, S. K., Van der Schoor, R., Jalink, H., Snel, J. F., … Aarts, M. G. (2016). Phenomics for photosynthesis, growth and reflectance in Arabidopsis thaliana reveals circadian and long-term fluctuations in heritability. *Plant Methods, 12*(1). doi:10.1186/s13007-016-0113-y

[69.] Honsdorf, N., March, T. J., Berger, B., Tester, M., & Pillen, K. (2014). High-Throughput Phenotyping to Detect Drought Tolerance QTL in Wild Barley Introgression Lines. *PLoS ONE, 9*(5), e97047. doi:10.1371/journal.pone.0097047

[70.] White, J. W., Andrade-Sanchez, P., Gore, M. A., Bronson, K. F., Coffelt, T. A., Conley, M. M., … Wang, G. (2012). Field-based phenomics for plant genetics research. *Field Crops Research, 133*, 101-112. doi:10.1016/j.fcr.2012.04.003

[71.] Araus, J. L., & Cairns, J. E. (2014). Field high-throughput phenotyping: the new crop breeding frontier. *Trends in Plant Science, 19*(1), 52-61. doi:10.1016/j.tplants.2013.09.008

[72.] Pauli, D., Andrade-Sanchez, P., Carmo-Silva, A. E., Gazave, E., French, A. N., Heun, J., … Gore, M. A. (2016). Field-Based High-Throughput Plant Phenotyping Reveals the Temporal Patterns of Quantitative Trait Loci Associated with Stress-Responsive Traits in Cotton. *G3: Genes, Genomes, Genetics*, *6*(4), 865-879. doi:10.1534/g3.115.023515

[73.] Mueller-Sim, T., Jenkins, M., Abel, J., & Kantor, G. (2017). The Robotanist: A ground-based agricultural robot for high-throughput crop phenotyping. *2017 IEEE International Conference on Robotics and Automation (ICRA)*. doi:10.1109/icra.2017.7989418

[74.] Salas Fernandez, M. G., Bao, Y., Tang, L., & Schnable, P. S. (2017). A High-Throughput, Field-Based Phenotyping Technology for Tall Biomass Crops. *Plant Physiology, 174*(4), 2008-2022. doi:10.1104/pp.17.00707

[75.] Vadez, V., Kholová, J., Hummel, G., Zhokhavets, U., Gupta, S. K., & Hash, C. T. (2015). LeasyScan: a novel concept combining 3D imaging and lysimetry for high-throughput phenotyping of traits controlling plant water budget. *Journal of Experimental Botany, 66*(18), 5581–5593. http://doi.org/10.1093/jxb/erv251

[76.] Sadeghi-Tehran, Pouria; Sabermanesh, Kasra; Virlet, Nicolas; Hawkesford, Malcolm J. (2017). Automated Method to Determine Two Critical Growth Stages of Wheat: Heading and Flowering. *Frontiers in Plant Science*. doi: 10.3389/fpls.2017.00252.

[77.] Virlet, N., Sabermanesh, K., Sadeghi-Tehran, P., & Hawkesford, M. J. (2017). Field Scanalyzer: An automated robotic field phenotyping platform for detailed crop monitoring. *Functional Plant Biology, 44*(1), 143. doi:10.1071/fp16163

[78.] Watanabe K., Guo W., Arai K., Takanashi H., Kajiya-Kanegae H., Kobayashi M., . . . Iwata H. (2017). High-throughput phenotyping of sorghum plant height using an unmanned aerial vehicle and its application to genomic prediction modeling. *Front. Plant Sci. 8*:421. 10.3389/fpls.2017.00421

[79.] Patrick, A., Pelham, S., Culbreath, A., Holbrook, C. C., Godoy, I. J., & Li, C. (2017). High throughput phenotyping of tomato spot wilt disease in peanuts using unmanned aerial systems and multispectral imaging. *IEEE Instrumentation & Measurement Magazine, 20*(3), 4-12. doi:10.1109/mim.2017.7951684

[80.] Fan, L., Jiajia, X., & Chu, Z. (2015). Method of Prediction on Vegetables Maturity Based on Kalman Filtering Fusion and Improved Neural Network. *2015 8th International Conference on Intelligent Networks and Intelligent Systems (ICINIS)*. doi:10.1109/icinis.2015.37

[81.] Padol, P. B., & Sawant, S. D. (2016). Fusion classification technique used to detect downy and Powdery Mildew grape leaf diseases. *2016 International Conference on Global Trends in Signal Processing, Information Computing and Communication (ICGTSPICC)*. doi:10.1109/icgtspicc.2016.7955315

[82.] Samajpati, B. J., & Degadwala, S. D. (2016). Hybrid approach for apple fruit diseases detection and classification using random forest classifier. *2016 International Conference on Communication and Signal Processing (ICCSP)*. doi:10.1109/iccsp.2016.7754302

[83.] West, T., Prasad, S., Bruce, L. M., Reynolds, D., & Irby, T. (2009). Rapid detection of agricultural food crop contamination via hyperspectral remote sensing. *2009 IEEE International Geoscience and Remote Sensing Symposium*. doi:10.1109/igarss.2009.5417520

[84.] Dimov, D., Kuhn, J., & Conrad, C. (2016). Assessment of cropping system diversity in the fergana valley through image fusion of landsat 8 and sentinel-1. *ISPRS Annals of Photogrammetry, Remote Sensing and Spatial Information Sciences, III*-7, 173-180. doi:10.5194/isprs-annals-iii-7-173-2016

[85.] Frangi, A. F., Niessen, W. J., Vincken, K. L., & Viergever, M. A. (1998). Multiscale vessel enhancement filtering. *Medical Image Computing and Computer-Assisted Intervention — MICCAI'98*, 130-137. doi:10.1007/bfb0056195

[86.] Wan, T., Zhu, C., & Qin, Z. (2013). Multifocus image fusion based on robust principal component analysis. *Pattern Recognition Letters, 34*(9), 1001-1008. doi:10.1016/j.patrec.2013.03.003

[87.] Li, X., & Wang, M. (2014). Research of multi-focus image fusion algorithm based on Gabor filter bank. *2014 12th International Conference on Signal Processing (ICSP)*. doi:10.1109/icosp.2014.7015092

[88.] Liu, Y., Liu, S., & Wang, Z. (2015). Multi-focus image fusion with dense SIFT. *Information Fusion, 23*, 139-155. doi:10.1016/j.inffus.2014.05.004

[89.] Phamila, Y. A., & Amutha, R. (2014). Discrete Cosine Transform based fusion of multi-focus images for visual sensor networks. *Signal Processing, 95*, 161-170. doi:10.1016/j.sigpro.2013.09.001

[90.] Wan, W., & Lee, H. J. (2016). Multi-Focus Image Fusion Based on Focused Regions Detection. *2016 International Conference on Computational Science and Computational Intelligence (CSCI)*. doi:10.1109/csci.2016.0158

[91.] Zhou, Q., Liu, X., Zhang, L., Zhao, W., & Chen, Y. (2016). Saliency-based image quality assessment metric. *2016 3rd International Conference on Systems and Informatics (ICSAI)*. doi:10.1109/icsai.2016.7811082

[92.] Kou, F., Chen, W., Wen, C., & Li, Z. (2015). Gradient Domain Guided Image Filtering. *IEEE Transactions on Image Processing, 24*(11), 4528-4539. doi:10.1109/tip.2015.2468183

[93.] Fast image dehazing using guided filter. (2015). *2015 IEEE 16th International Conference on Communication Technology (ICCT)*. doi:10.1109/icct.2015.7399820

[94.] Mohammed Amean, Z., Low, T., McCarthy, & C., Hancock, N. (2013). Automatic plant branch segmentation and classification using vesselness measure. *Proceedings of the Australasian Conference on Robotics and Automation (ACRA 2013).*

[95.] C. L. McCarthy, N. H. Hancock, & S. R. Raine (2009). Automated Internode Length Measurement of Cotton Plants under Field Conditions. *Transactions of the ASABE, 52*(6), 2093-2103. doi:10.13031/2013.29198

[96.] Jin, J., & Zakhor, A. (2017). Point Cloud Based Approach to Stem Width Extraction of Sorghum. *Electronic Imaging, 2017*(17), 148-155. doi:10.2352/issn.2470-1173.2017.17.coimg-438

[97.] Latecki, L. J., Li, Q., Bai, X., & Liu, W. (2007). Skeletonization using SSM of the Distance Transform. *2007 IEEE International Conference on Image Processing*. doi:10.1109/icip.2007.4379837

[98.] Saha, P. K., Borgefors, G., & Sanniti di Baja, G. (2016). A survey on skeletonization algorithms and their applications. *Pattern Recognition Letters, 76*, 3-12. doi:10.1016/j.patrec.2015.04.006

[99.] Lantuejoul, C. (1980). Skeletonization in Quantitative Metallography. *Issues in Digital Image Processing*, 107-135. doi:10.1007/978-94-009-9133-0_5

[100.] Hassouna, M. S., & Farag, A. A. (2007). MultiStencils Fast Marching Methods: A Highly Accurate Solution to the Eikonal Equation on Cartesian Domains. *IEEE Transactions on Pattern Analysis and Machine Intelligence, 29*(9), 1563-1574. doi:10.1109/tpami.2007.1154

[101.] Zhang, L., Gu, Z., & Li, H. (2013). SDSP: A novel saliency detection method by combining simple priors. *2013 IEEE International Conference on Image Processing*. doi:10.1109/icip.2013.6738036

[102.] Xue, W., Zhang, L., Mou, X., & Bovik, A. C. (2014). Gradient Magnitude Similarity Deviation: A Highly Efficient Perceptual Image Quality Index. *IEEE Transactions on Image Processing, 23*(2), 684-695. doi:10.1109/tip.2013.2293423

[103.] Zhou, Z., Li, S., & Wang, B. (2014). Multi-scale weighted gradient-based fusion for multi-focus images. *Information Fusion*, 20, 60-72. doi:10.1016/j.inffus.2013.11.005

[104.] V. Naidu, B. Elias. (2013). A novel image fusion technique using dct based laplacian pyramid. *International Journal of Inventive Engineering and Sciences (IJIES).*

[105.] Shutao Li, Xudong Kang, & Jianwen Hu. (2013). Image Fusion with Guided Filtering. *IEEE Transactions on Image Processing, 22*(7), 2864-2875. doi:10.1109/tip.2013.2244222

[106.] Paul, S., Sevcenco, I. S., & Agathoklis, P. (2016). Multi-Exposure and Multi-Focus Image Fusion in Gradient Domain. *Journal of Circuits, Systems and Computers, 25*(10), 1650123. doi:10.1142/s0218126616501231

[107.] Li, S., Kang, X., Hu, J., & Yang, B. (2013). Image matting for fusion of multi-focus images in dynamic scenes. *Information Fusion, 14*(2), 147-162. doi:10.1016/j.inffus.2011.07.001

[108.] Jamal Saeedi (2015, March). *Multi focus image dataset*. Retrieved from https://www.researchgate.net/profile/Jamal_Saeedi/publication/273000238_multi-focus_image_dataset/data/54f489b80cf2ba6150635697/multi-focus-image-dataset.rar

[109.] M. Nejati, S. Samavi, and S. Shiraniv (2015, September). *Lytro multi focus dataset*. Retrieved from http://mansournejati.ece.iut.ac.ir/content/lytro-multi-focus-dataset

[110.] Hossny, M., Nahavandi, S., & Creighton, D. (2008). Comments on ‘Information measure for performance of image fusion’. *Electronics Letters*, *44*(18), 1066. doi:10.1049/el:20081754

[111.] Yang, C., Zhang, J., Wang, X., & Liu, X. (2008). A novel similarity based quality metric for image fusion. *Information Fusion, 9*(2), 156-160. doi:10.1016/j.inffus.2006.09.001

[112.] Xydeas, C., & Petrović, V. (2000). Objective image fusion performance measure. *Electronics Letters, 36*(4), 308. doi:10.1049/el:20000267